The Pennsylvania State University

The Graduate School

Department of Electrical Engineering

PHOTOACTIVE NANOSTRUCTURED MATERIALS AND DEVICES: Pt PHOTOANODES, Cu PHOTOCATALYSTS AND SnS ABSORBERS

A Dissertation in

Electrical Engineering

by

Hyeonseok Lee

Submitted in Partial Fulfillment
of the Requirements
for the Degree of

Doctor of Philosophy

May 2014

The dissertation of Hyeonseok Lee was reviewed and approved* by the following:

Mark W. Horn
Professor Engineering Science and Mechanics
Dissertation Advisor
Co-chair of Committee

Jerzy Ruzyllo
Distinguished Professor Electrical Engineering
Co-chair of Committee

Joan M. Redwing
Professor Electrical Engineering

Srinivas Tadigadapa
Professor Electrical Engineering

Jeffrey R. S. Brownson
Assistant Professor Energy & Mineral Engineering

Kultegin Aydin
Professor
Head of the Department of Electrical Engineering

*Signatures are on file in the Graduate School

ABSTRACT

Growing demand of energy and global warming concern regarding CO_2 gases urge researchers to seek an alternative source of energy. Among all candidates, solar energy is very promising owing to its clean and renewable nature. In order to convert the solar energy into useful form such as electricity or hydrocarbon fuel, photoactive materials and devices are commonly used. However, their conversion efficiency is always problematic.

In this dissertation, utilization of the solar energy with three different devices incorporating sculptured thin films (STFs) was demonstrated: (1) electricity generation by dye-sensitized solar cells adopting sculptured Pt nanowire counter electrodes, (2) TiO_2 photocatalytic film with columnar Cu cocatalyts, and (3) sculptured SnS thin film solar cells.

First, Pt STFs were fabricated for dye-sensitized solar cells with 5° obliquely incident vapor flux by electron beam evaporator. Pt STFs exhibit more desirable features for more functional counter electrodes than that in conventional Pt planar counter electrodes. Higher root mean square surface roughness of 44.4 nm and lower charge transfer resistance of 0.121 Ω·㎠ were measured for Pt STF than the root mean square surface roughness of 19.1 nm and charge transfer resistance of 0.578 Ω·㎠ for Pt planar films .These improvement in morphology and electrochemical properties led enhanced photocurrent density and conversion efficiency (9.766 mA/cm^2, 5.1 %).

Second, Cu cocatalysts were sculptured directly on porous TiO_2 catalyst films. Varied lengths of Cu columns were grown and methane production rate from carbon dioxide and water was evaluated under AM 1.5 illumination. The methane production rate showed a maximum of 124.3 $ppm \cdot cm^{-2} \cdot h^{-1}$ with 160 nm Cu column films. This maximum corresponds to the point where the absorption peak at ~600 nm that is attributed to plasmonic effect by Cu STFs.

Third, SnS thin films were deposited by radio frequency magnetron sputter. Deposited SnS thin films were characterized in structural, optical, and electrical manner. Surface morphology and growth pattern of the films were varied, depending on variation of deposition parameters such as power, pressure, throw distance and substrate heating. This variation was related to the energy of deposition modes that is possibly explained by mean free path and mean speed of the vapor flux. Also, the deposition rate is related to diffused vapor flux. The optical properties of the SnS thin films were investigated by spectroscopic ellipsometry. Obtained absorption coefficient was $>10^4$ cm^{-1} even in the range of >1000 nm wavelength. The calculated direct bandgap and indirect bandgap of SnS thin films were ranged from 1.33 to 1.55 eV and from 1.07 to 1.39 eV, respectively. In the investigation of electrical properties by using transport length method, it is found that the SnS films with lower root mean square roughness exhibited lower resistivity while more structured SnS film showed higher resistivity. In addition, the photoresponse was observed under AM 1.5 illumination. SnS thin film solar cells were fabricated in the two different types of thin film solar cells and electrochemical solar cells. The SnS electrochemical solar cells showed photovoltaic behavior and improved voltage, fill factor and efficiency (V_{oc}= 0.38, FF=0.26 and η=0.0025 %) were measured with the incorporation of the sculptured SnS thin films.

TABLE OF CONTENTS

LIST OF FIGURES

LIST OF TABLES

ACKNOWLEDGEMENTS

I would like to thank the people that helped me to successfully finish all my Ph. D. work. Without the people, I could have not accomplished what I have done so far.

First of all, I would like to express my sincere gratitude to my advisors, Dr. Mark W. Horn and Dr. Jerzy Ruzyllo that have encouraged me to keep pursuing Ph. D course with invaluable guidance and support. I also thank to my committee members, Dr. Joan M. Redwing, Dr. Srinivas Tadigadapa and Dr. Jeffrey R. S. Brownson for valuable comments and suggestions.

I would like to thank the previous and current lab members, Sean M. Pursel, Micheal A, Motyka, Yao Jin and Hitesh Basantani that gave proper help in the experiments when I needed. In addition, I would like to thank Dr. Suil In and Rona Banai who made possible to keep doing the exiting research with sincere collaboration and useful discussion. I would like to thank The Korean graduate student society in the department of electrical engineering. It has been very helpful for my family to be easily adapted to the life in State College. I would like to thank Dr. Kenneth Jenkins and Ms. Sherry Dawn Jackson for proper help when I was in a difficulty.

Lastly, my family deserves a special mention. My wife, Jinhee Lee gave me a cheerful word whenever I am discouraged and support in every aspect of my life during Ph. D. course. She was and is my infinite source of courage and love with my lovely daughter, Ashlyn Jooeun Lee. I also would like to thank my family in Korea for sincere support.

Chapter 1

Introduction

The harvesting of solar power for photovoltaic energy generation and CO_2 conversion into useful fuels are two areas of great interest for future world energy needs. The perceived risk of using up all our fossil fuels and the measured increase in CO_2 emission has urged many countries to develop and utilize renewable sources such as solar, wind, and geothermal energy. Among these valuable sources of energy, solar energy is considerably promising as alternative energy source because it is clean without CO_2 emission and its reservoir is tremendous–e.g. the energy generated from the area of 25,921 km ^{2} with 10 % solar-to-electrical system efficiency for one year is able to support annual energy consumed in USA territory of 9,826,675 km^2 [1].

For solar energy conversion into electricity, solar cells have been regarded as useful tool. To date, various types of solar cells have been suggested and developed: (1) inorganic solar cells incorporating inorganic semiconductor materials such as silicon and gallium arsenide or next generation materials for thin film solar cells such as copper indium gallium sulfide (CIGS) and cadium telluride (CdTe), (2) dye-sensitized solar cells (DSSCs) consisted of light-absorbing dye molecules, oxidized semiconductor materials, redox electrolyte, and catalyzed counter electrodes, and (3) organic solar cells with light-absorbing polymer and conductive polymers. Silicon has taken more than 70-80 % in the solar cell market share for the last few decades since it has its high conversion efficiency and is an abundant material but it has the disadvantage of a high price for a crystalline silicon wafer. In the fabrication of the crystalline silicon solar module, more than 50 % of the cost would be consumed by the silicon wafer [2]. For this reason, a solar cell made with thin films could be considered as an alternative because the thin film solar cells are much

more efficient than the crystalline silicon solar cells in materials usage. Currently, the thin film solar cell industry is mostly focused on CIGS, CdTe or amorphous silicon. Even though these materials exhibit a high absorption coefficient and high conversion efficiency only with thin films, a variety of the thin film solar cell materials cannot be excluded for the future industry. In particular, it is necessary to hedge against the exhaustion of less abundant, more expensive materials since reservoir of the materials on earth crust are always finite. Moreover, in the case of the thin film solar cells based on cadmium, it has toxicity that must be addressed. In these aspects, discovering another promising candidate for thin film solar cells is greatly worthwhile. Tin sulfide is a very attractive material to research in this aspect since it has strengths in its excellent optical property, abundance in the earth's crust and nontoxicity. For practical fabrication of a SnS-based solar cell, fundamental research on SnS materials and its films is needed first.

Simultaneously, the research on various types of solar cells must be accompanied for the growth of photovoltaic industry. This enables the solar cells industry to give capability for low cost fabrication and flexibility on solar power generation sites, not relying only on massive electricity generation farms in a limited place. DSSCs or organic solar cells can provide solar cells with mobility and flexibility in application. Particularly, DSSCs show higher conversion efficiency and flexibility in certain applications owing to development of the efficient photoreactive dye molecules and availability on various substrates. Among three main parts –i.e. photoelectrode, electrolyte and counter electrode,– counter electrodes also should be studied vibrantly for a breakthrough in efficiency.

In addition to solar energy utilization by solar cells, solar energy can contribute to producing useful hydrocarbon fuels such as methane by reducing atmospheric CO_2 gas via a photocatalyst. The CO_2 conversion through the use of a photocatalyst is an attractive possibility since it is the way of not only reducing atmospheric CO_2 level but also producing useful fuels in a time. A popular material for the photocatalysts is TiO_2 based catalyst with a metal cocatalyst.

Previous research has focused mainly on the TiO_2 catalyst but, for enhanced hydrocarbon production rate, optimization or modification of the cocatalyst is also necessary.

Performance of photovoltaic solar energy conversion and CO_2 conversion to hydrocarbon fuels by solar energy can be improved by modifying the morphology or structure of the device by enhancing the surface area such that excellent chemical or electrical reactions can be realized. In this thesis, sculptured thin films (STFs) are utilized to improve the performance of two solar energy conversion devices: as the platinum counter electrode of DSSCs and as a copper cocatalyst for photocatalysis in CO_2 conversion. Lastly, they are preliminarily explored for tin sulfide as a light absorber in a heterojunction solar cell. The STFs are deposited in a columnar structure with oblique vapor flux. Owing to its higher surface area and nominal 1-D structure, STFs are used to improve solar energy conversion and CO_2 conversion by increasing reactive sites through their structural features.

The Chapter 2 of this dissertation describes background knowledge for sculptured thin films (STFs) and their fabrication. Methodology of STFs is explained with examples in Chapter 2. In Chapter 3, the motivation of the research, history, mechanism, and materials for dye-sensitized solar cells are introduced. The results and discussions on how a sculptured platinum nanowire counter electrode works for DSSCs are also provided in Chapter 3. Chapter 4 presents background knowledge of CO_2 conversion through photocatalysts as well as the motivation of the research using Cu STFs. Data is presented on the use of Cu columnar structures and the role of the Cu STFs as cocatalyst. The reasons for the improvement in methane production rate are also discussed. Fundamental description for SnS thin films and its potential use in solar cells is provided in Chapter 5. Prior to adoption of the sculptured SnS thin film for solar cells, experimental findings and understanding features of sputtered SnS thin films are discussed with regard to their morphology, optical properties and electrical properties. Chapter 6 provides conclusions and suggested future work.

.

1.1 Chapter 1 References

[1] J. A. Turner, A realizable renewable energy future, *Science* Vol. 285 30 July (**1999**) 687-689.

[2] M. A. Green, Thin-film solar cells: review of materials, technologies and commercial status, *Journal of Materials Science: Materials in Electronics* Vol. 18 (**2007**) S15-S19.

Chapter 2

Sculptured Thin Films

Sculptured thin films (STFs) are films grown from an obliquely incident vapor flux, χ_v with or without substrate rotation. STFs exhibit columnar or porous structure with various morphologies depending on the movement or angle of the substrate. Various structures, from a simple slanted columnar structure to a complex zigzag or helical structure, are realizable with the STF methodology as shown in Figure 2-1 (a)-(c). The schematic of STF methodology for making a columnar structure by physical vapor deposition is shown in Figure 2-1(d).

In oblique deposition, the directionality of vapor flux is the essential for deposition of STFs. These unique and valuable structures are dominated by a shadowing effect and adatom diffusion. The shadowing effect occurs naturally with an obliquely incident vapor flux. In other words, the vapor flux that arrived at the substrate already shadows an area behind that the higher topography. This shadowing of the vapor flux at the nanoscale enables thin films to be porous, or eventually be a columnar structure. Generally speaking, materials with low adatom mobility—i.e. a high melting point material used in a room temperature deposition—have low surface diffusion. Hence, this kind of material is difficult to fill out the porous space between columns by surface diffusion of adatoms and this helps the vapor flux to construct columns on a substrate. In order to make the self-shadowing effective, the angle of incident vapor flux should generally be less than 15°with respect to the plane of the substrate [1-2].

Various materials are able to be chosen for STF methodology as shown in Table 2-1. Applicable materials to the STF methodology include oxides, fluorides, metals, semiconductors, and even polymers [3].

Group of Materials	Materials
Oxides	aluminum oxide, silicon oxide, tantalum oxide, titanium oxide, zirconium oxide
Fluorides	calcium fluoride, magnesium fluoride
Metals	aluminum, bismuth, chromium, copper, iron, platinum, titanium, tungsten
Semiconductors	carbon, germanium, silicon
Polymer	Parylene, Teflon

Table 2-1. Examples of the materials for sculptured thin film methodology (Ref. [3]).

The STF deposition can be affected by several essential factors. First factor is the angular distribution of the emitted material from the vapor source. Generally, emitted species can be explained as three different distributions: cosine distribution, under-cosine distribution and over-cosine distribution. For instance, electron beam evaporation follows over-cosine distribution of emitted vapor flux while sputtering applied with low energy is an example for under cosine distribution of the emitted vapor flux. For STF deposition, using physical vapor deposition with high energy is favorable since over-cosine distribution is desirable. A second important factor for STF deposition is the relative size and shape of the vapor source and the tilted substrate. In order to make a collimated vapor flux, the ratio of the distance between vapor source and substrate, $d_{S\text{-}S}$ to the diameter of the substrate, d_{subs} should be kept at a high value. Moreover, distribution of χ_v becomes less broad as the $d_{S\text{-}S}/d_{sub}$ increases. Third, the scattering of the vapor flux during transport from the source to the substrate affects the STF deposition. The existence of gas phase species within the chamber increases the chance of collision with vapor flux emitted toward

substrate. When the collision occurs, the broadening of χ_v is inevitable. For this reason, mean free path of emitted species should be considered. In case of the mean free path $\geq d_{S\text{-}S}$, the gas-phase collision is negligible but when the mean free path $\ll d_{S\text{-}S}$, diffusion transport becomes dominant for vapor flux. In the intermediate range, χ_v distribution and the average value of χ_v, $< \chi_v >$ can be varied. Fourth, the vapor collimation is able to be engineered by adopting a collimator. For example, adopting a cascade of tilted substrates can narrow χ_v distribution. Insertion of a physical collimator between source and substrate is also one of the methods to attain direct collimation for STF deposition. A fifth factor to consider is the energy of the condensing vapor species at impingement with the growing film. The emitted vapor flux are thermalized by elastic collision, being related to the deposition pressure and the distance between substrate and source. When ions are accelerated by electromagnetic fields, a more directed and collimated vapor flux could be obtained. Sixth factor is concurrent ion bombardment at the growing film as a moderating

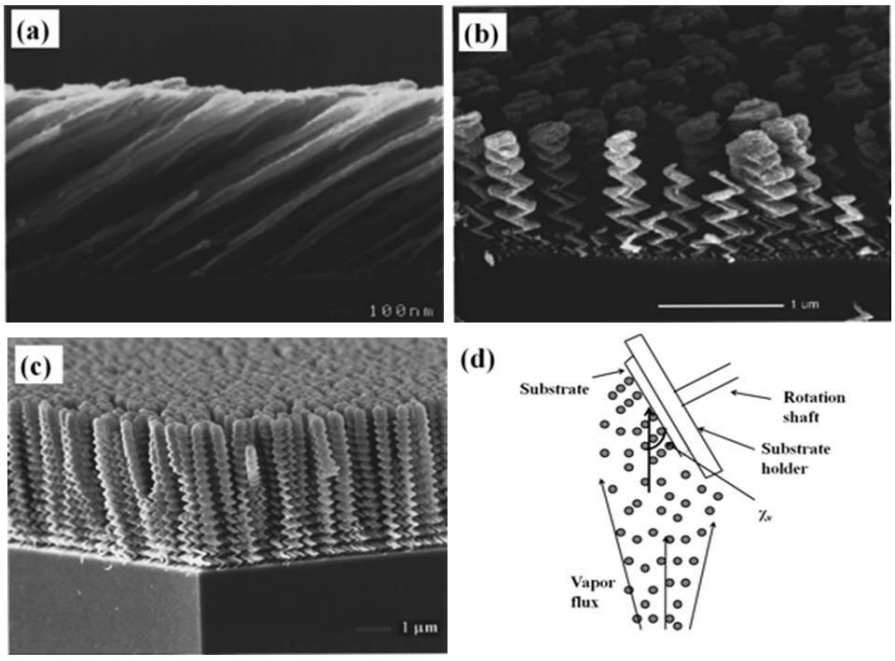

Figure 2-1. Fabrication of sculpture thin films: morphology of (a) slanted STFs, (b) zigzag STFs and (c) helical STFs (Ref. [4]), (d) schematic of STF fabrication method by incident vapor flux with substrate rotation (χ_v: incident vapor flux angle).

mechanism to shadowing-related columnar expansion. The concurrent ion bombardment with the energies ranged from around 10 eV to 100 eV aids for stable columnar structure growth normal to the substrate [3].

2.1 Controlled Sculptured Thin Film Deposition

As mentioned above, one of the essential parameters is the incident vapor flux angle, χ_v. Usually, a small χ_v is preferred for more columnar and porous films. Figure 2-2 shows SiO sculpture thin films with various incident vapor flux angles [4]. As the incident vapor flux angle decreases, the separation between columnar structures becomes larger and, thereby, the film becomes a more porous film. In case of SiO STFs, it is reported that SiO STFs at 25° vapor flux

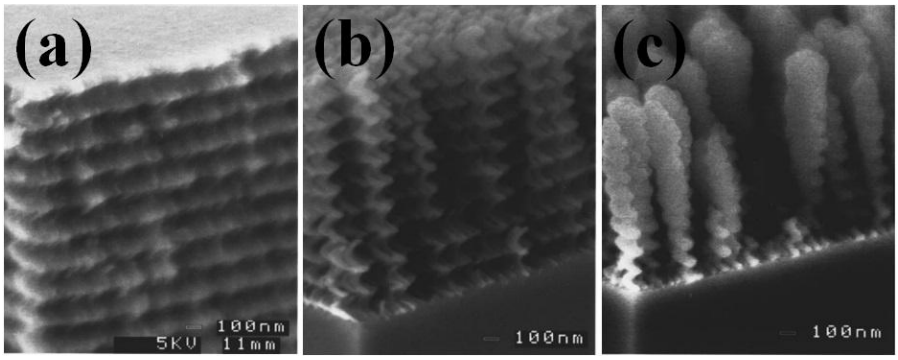

Figure 2-2. Sculptured SiO thin films with varied incident flux angle of (a) 25°, (b) 15° and (c) 2° (Ref. [4]).

angle show ~90 % of the film density and the film density decreased to 20 % as the incident vapor flux angle decreased [4]. Other materials exhibited the same tendency with a decrease in the incident vapor flux angle but relative density was higher in the materials with higher adatom mobility such as Cu and Mn in comparison with the density of the materials with lower adatom mobility such as Al , Cr and CaF_2 [4]. This is related to the degree of self shadowing that occurred by obliquely incident vapor flux angle.

When the STFs are deposited with the rotation that has constant velocity, the STFs can be grown in helicoidal columns. As shown in Figure 2-2, the pitch within helicoidal structure is constant with constant rotation velocity, but the pitch can be reduced as the rotation velocity become faster while the pitch can be widened with a slower rotation velocity [3].

The columnar structure that is grown in STFs should be constant in size and shape through entire structure to obtain constant optical properties. However, some techniques for STF deposition show the expansion of the columnar structure for thicker film depositions. Figure 2-3 (a) and (b) shows the MgF_2 STFs grown in superhelical structure and in slanted structure, respectively. The expansion of the columns is clearly seen as the deposition proceeds. In higher incident flux angle, the STFs experience more column width expansion at higher thickness (See Figure 2-3 (b) and (c)) [5]. Thus, in order to keep uniform column widths, low incident flux angles were used for this thesis.

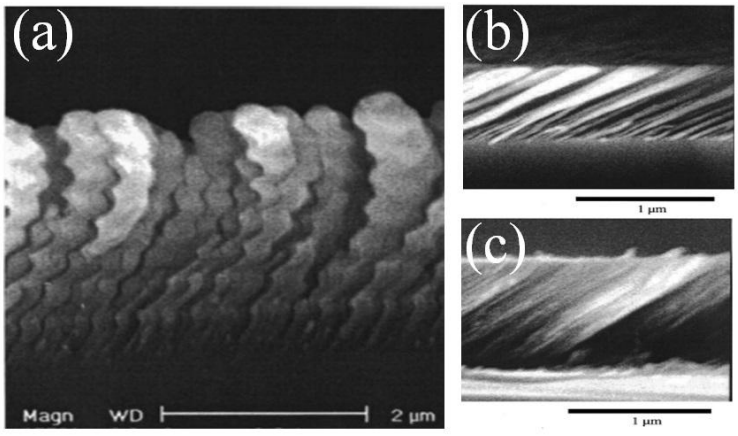

Figure 2-3. Sculptured MgF_3 thin films with varied incident flux angle of (a) 8° in superhelical structure, (b) 3° and (c) 22.5° in slanted structure (Ref. [5]).

2.2 Various Applications with Sculptured Thin Films

STFs have demonstrated their strengths for various applications owing to excellent optical properties with higher surface area and aspect ratio. One area that the STFs are frequently adopted is the solar cell application. TiO_2 STFs have been used as the photoanode in hybrid solar cells with poly(3-hexylthiophene) (P3HT) by electron beam evaporation [6]. The study was implemented about the effect by controlled porosity of STFs for the conversion efficiency of the hybrid solar cells [6]. TiO_2 STFs have also applied to dye-sensitized solar cells (DSSCs) as photoanode [7]. Varied incident vapor flux angles allowed the TiO_2 to have columnar and porous structure and the TiO_2 STFs prepared at 40° of the incident vapor flux attributed to 4.1 % of the conversion efficiency [7]. In another research for DSSCs incorporating TiO_2 STFs, DSSCs were fabricated with 8.5 μm thick TiO_2 STFs sculptured at 10° of incident vapor flux angle. With a TiO_2 scattering layer, the DSSCs exhibited 6.04 % of conversion efficiency [8]. Copper phthalocyanine (CuPc) was sculptured by Dijiken et al. via thermal evaporation for use in organic solar cells [9]. CuPc thin films were grown both on PEDOT:PSS coated on indium tin oxide (ITO) and on seeded substrate which is prepared by the block copolymer method. The CuPc columnar structure had few hundred nanometer length and 15-30 nm of diameter [10]. Rider et al. studied indium tin oxide STFs to demonstrate three-dimensional high surface area transparent electrodes for organic solar cells [10]. Subsequent layer deposited with PEDOT:PSS on the ITO STFs has cobweb-like morphology and its surface area was ~ten-fold higher than that of a commercial ITO substrate. The ITO STFs were reported to yield cells of 2.2 % of solar-to-electricity conversion efficiency [10].

Sculptured TiO_2 films were used as transparent and conductive electrodes for thin-film silicon solar cells. TiO_2 STFs led 68 % increase in optical haze at 600 nm and the solar cells yielded conversion efficiency of 6.6 % [11]. Y. Zhou and coworkers demonstrated sculptured CuI

nanocrystals for organic solar cells based on a junction of Zinc phthalocyanine and C_{60}. CuI STFs showed improved light absorption with higher surface roughness and this resulted in high conversion efficiency of 4.08 % [12].

Another area of STF applications is for sensors owing to innate high surface area and high aspect ratio. In particular, a lot of research has been carried out for humidity sensors fabricated with STFs with various materials. Humidity sensors were fabricated with TiO_2, SiO and Al_2O_3 and tens of miliseconds response time were reported [13-15]. Microfluidic structures were also fabricated with STFs. Silicon STFs deposited at 6° of the incident vapor flux on patterned substrate and acted as microfluidic channel [16]. Narrow bandpass optical filters have been demonstrated by Hawkeye et al. It is reported that, during TiO_2 STF deposition, a defect layer were inserted into the film in controllable manner, and the resulting films established passband within a stop band [17].

In this thesis, STF methodology has been used to fabricate a platinum electrode for a DSSC, a copper cocatalyst for CO_2 and a SnS thin film used in an electrochemical solar cell. The first two applications were performed using e-beam evaporation whereas the last application was via rf sputtering. As expected, the last application had much less precise morphology than the first two applications because of the larger source and higher pressure utilized in sputtering.

2.3 Chapter 2 Reference

[1] K. Robbie, L. J. Friedrich, S. K. Dew, Fabrication of thin films with highly porous microstructures, *Journal of Vacuum Science and Technology A* Vol. 13 No. 3 May/Jun (**1995**) 1032-1035.

[2] R. Messier, T. Gehrke, C. Frankel, V. C. Venugopal, W. Otaño, A. Lakhtakia, Engineered sculptured nematic thin films, *Journal of Vacuum Science and Technology A* Vol. 15 No. 4 Jul/Aug (**1997**) 2148-2152.

[3] A. Lakhtakia, R. Messier, Sculptured thin films: nanoengineered morphology and optics, *The Society of Photo-Optical Instrumentation Engineers* Bellingham, Washington, USA (**2005**).

[4] K. Robbie, M. J. Brett, Sculptured thin films and glancing angle deposition: growth mechanics and applications, *Journal of Vacuum Science and Technology A* Vol. 15 No. 3 May/Jun (**1997**) 1460-1465.

[5] R. Messier, V. C. Venugopal, P. D. Sunal, Origin and evolution of sculptured thin films, *Journal of Vacuum Science and Technology A* Vol. 18 No. 4 Jul/Aug (**2000**) 1538-1545.

[6] N. J. Gerein, M. D. Fleischauer, M. J. Brett, Effect of TiO_2 film porosity and thermal processing on TiO_2-P3HT hybrid materials and photovoltaic device performance, *Solar Energy Materials & Solar Cells* Vol. 94 (**2010**) 2343-2350.

[7] G. K. Kiema, M. J. Colgan, M. J. Brett, Dye sensitized solar cells incorporating obliquely deposited titanium oxide layers, *Solar Energy Materials & Solar Cells* Vol. 85 (**2005**) 321-331.

[8] S. M. Pursel, Dye sensitized solar cells based on nanowire sculptured thin film titanium dioxide photoanodes, *Ph. D dissertation* Pennsyvania State Univeristy, University Park, USA (**2011**).

[9] J. G. V. Dijken, M. D. Fleischauer, M. J. Brett, Controlled nanostructuring of CuPc thin films via glancing angle deposition for idealized organic photovoltaic architecture, *Journal of Materials Chemistry* Vol. 21 (**2011**)1013-1019.

[10] D. A. Rider, R. T. Tucker, B. J. Worfolk, K. M. Krause, A. Lalany, M. J. Brett, J. M. Buriak, K. D. Harris, Indium tin oxide nanopillar electrodes in polymer/fullerene solar cells, *Nanotechnology* Vol. 22 (**2011**) 085706-085714.

[11] K. Hung, G. Chiou, M. Wong, Y. Wang, I. Chung, Transparent sculptured titania films for enhanced light absorption in thin-film Si solar cells, *Thin Solid Films* Vol. 520 (**2011**) 1385-1389.

[12] Y. Zhou, T. Taima, T. Miyadera, T. Yamanari, M. Kitamura, K. Nakatsu, Y. Yoshida, Glancing angle depositon of copper iodide nanocrystals for efficient organic photovoltaics, *Nano Letters* Vol. 12 (**2012**) 4146-4152.

[13] K. D. Harris, A. Huizinga, M. J. Brett, High-speed porous thin film humidity sensors, Electrochemical and Solid-State Letters Vol. 5 No. 11 (2002) H27-H29.

[14] J. J. Steele, J. P. Gospodyn, J. C. Sit, M. J. Brett, Impact of Morphology on High-speed humidity sensor performance, *IEEE Sensors Journal*, Vol. 6 No. 1 February (**2006**) 24-27.

[15] M. T. Taschuk, J. B. Sorge, J. J. Steele, M. J. Brett, Ion-beam assisted glancing angle deposition for relative humidity sensors, *IEEE Sensors Journal*, Vol. 8 No. 9 February (**2008**) 1521-1522.

[16] G. K. Kiema, M. O. Jenson, M. J. Brett, Glancing angle deposition thin film microstructures for microfluidic application, *Chemistry of Materials* Vol. 17 (**2005**) 4046-4048.

[17] M. M. Hawkeye, M. J. Brett, Narrow bandpass optical filters fabricated with one-dimensionally periodic inhomogeneous thin films, *Journal of Applied Physics* Vol. 100 (**2006**) 044322-1-044322-7.

Chapter 3

Sculptured Platinum Nanowire Counter Electrodes for Dye-sensitized Solar Cells

Dye-sensitized solar cells (DSSCs) have been of great interest since efficient solar cells with more than 7 % conversion efficiency were reported by Grätzel and coworker in 1991 [1]. Due to the nature of materials used and fabrication method, DSSCs are advantageous in fabrication cost in comparison with other inorganic solar cells based on vacuum facilities and energy intensive high temperature processes. Moreover, DSSCs can be used in decorative applications through use of various colors of dyes [1-3].

Chapter 3.1 and 3.2 review the basic of DSSCs including operating mechanisms and materials for each component. Chapter 3.3 gives motivation on the research for sculptured platinum counter electrodes. Chapter 3.4 talks about the experiment for this research, while the results and discussion are provided in Chapter 3.5 and are summarized in Chapter 3.6.

3.1 Concept of Dye-sensitized Solar Cells

DSSCs are fundamentally classified as excitonic solar cells, in the same category as organic solar cells [4]. As indicated by its name, DSSCs produce bound electron-hole pairs– namely, excitons—while conventional inorganic solar cells such as silicon based solar cells generate free electron—hole pairs with incident light. Excitons must be dissociated to generate free carriers and, thereby, allowing current to flow through the solar cells. However, since exitons are hard dissociate by the internal electric field established in solar cells, DSSCs feature a heterojunction structure that can provide excitons with sufficient potential energy for their dissociation [4].

A schematic of typical a DSSC is shown in Figure 3-1. DSSCs have three main components: photo electrode, redox electrolyte, and counter electrode. The photoelectrode plays an essential role in absorbing light energy and transporting electron generated. Dye molecules are excited from the ground state ($S^0 \rightarrow S^*$) when exposed to incident light. At this time, excitons are generated and diffuse away toward the interface of semiconductor/dye molecule. Excitons that arrived at the interface are dissociated by the potential difference and, then, unbounded electrons and holes are subsequently generated. These free electrons can be injected to the conduction band of semiconductor materials—herein, TiO_2 –at the semiconductor/dye molecule interface. The electrons in the conduction band continue to diffuse along the pathway paved by semiconductor materials and flow out to the external circuit. In the mean time, oxidized dye molecules (S^+) return to their ground states and are regenerated by electrons from redox couples in the electrolyte. The counter electrode–herein, Pt electrode–reacts with oxidized species with an electron from external circuit at the electrolyte/counter electrode interface [1-5]. Recapture and recombination can be occurred between conduction band electrons and I_3^- species and between oxidized dye molecules and conduction band electrons, respectively. The operating cycle is summarized by reactions (3.1) to (3.5) listed below [5].

$TiO_2\|S + h\nu \rightarrow TiO_2\|S^*$	excitation	(3.1)
$TiO_2\|S^* \rightarrow TiO_2\|S^+ + e^-_{(cb)}$	injection	(3.2)
$TiO_2\|2S^+ + 3I^- \rightarrow TiO_2\|2S + I_3^-$	regeneration	(3.3)
$I_3^- \rightarrow 2e^-_{(Pt)} \rightarrow 3I^-$	reduction	(3.4)
$I_3^- \rightarrow 2e^-_{(cb)} \rightarrow 3I^-$	recaption (dark reaction)	(3.5)
$TiO_2\|S^+ + e^-_{(cb)} \rightarrow TiO_2\|S$	recombination (dark reaction)	(3.6)

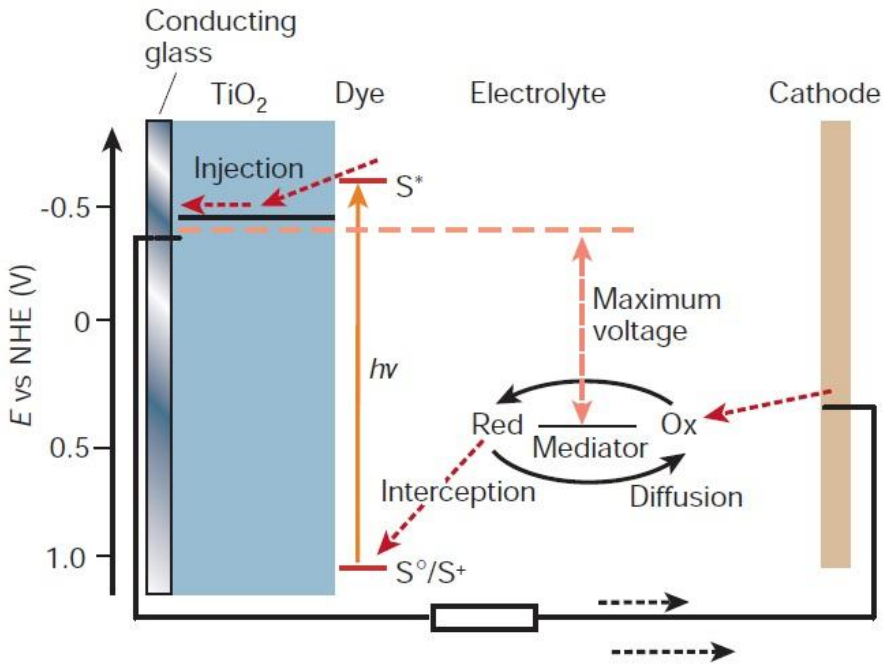

Figure 3-1. Schematic of dye-sensitized solar cells showing reactions and energy potential (Ref. [3]). NHE stands for normal hydrogen electrode.

All these processes to generate current mentioned above in equations (3.1) through (3.6) in DSSCs can be realized by the competition between the processes. In DSSCs, electron injection from the excited dye molecules to the TiO_2 and dye regeneration after electron injection occurrs in femto- and nano-seconds, respectively while electron transport through the interconnection of TiO_2 particles and interfacial recombination at TiO_2/electrolyte interface takes place in millisecond range [2]. Faster reactions in electron injection and dye regeneration enable DSSCs to work efficiently.

In addition, for designing a DSSC, two main points must be considered. First point is how efficiently dye molecules absorb the light energy. This is determined by the light-harvesting

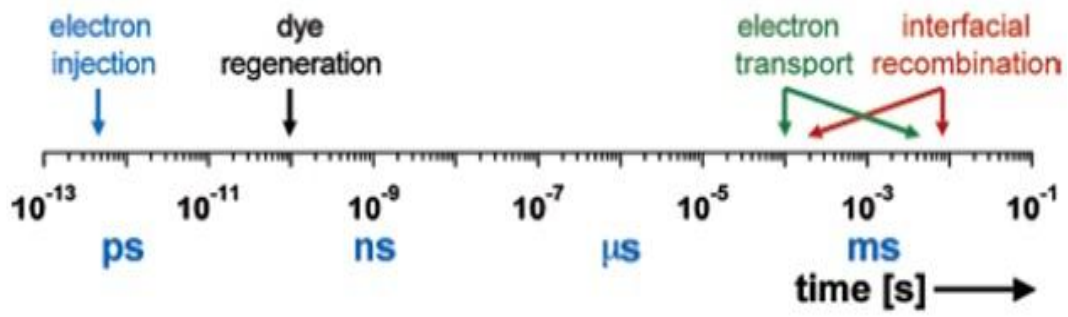

Figure 3-2. Schematic of dye-sensitized solar cells (Ref. [2]).

efficiency (LHE). LHE is described with absorption coefficient, α in terms of light wavelength, λ below,

$$\mathrm{LHE}(\lambda) = 1 - 10^{-\alpha d} \tag{3.7}$$

Where d is the thickness of the semiconductor oxide film [2]. The film thickness should be enough thicker than absorption length 1/α for higher LHE. Second point is how much current can be extracted from a DSSC. The incident photon to current conversion efficiency (IPCE)— it is also referred to external quantum efficiency—explain on this part. IPCE is related to monochromatic photons and, thereby, generated photocurrent as in below,

$$\mathrm{IPCE}(\lambda) = \mathrm{LHE}(\lambda) \cdot \phi_{\mathrm{inj}} \eta_{\mathrm{coll}} \tag{3.8}$$

Where ϕ_{inj} is the quantum yield for electron injection from the excited sensitizer in the conduction band of the semiconductor oxide and η_{coll} is the electron collection efficiency [2]. In order to achieve an efficient DSSC, all photogenerated charge carriers must be transferred to external circuit. For this reason, the pathway of current that flow out of the DSSCs should be designed by considering diffusion length of charge carrier through a semiconductor oxide film. The carrier diffusion length of charge carrier, L is explained as,

$$L = \sqrt{D \cdot \tau} \quad (3.9)$$

where D is the diffusion constant of electron and τ is the charge carrier lifetime. When semiconductor oxide thickness is within the range of charge carrier diffusion length, photogenerated carriers can be efficiently collected to external circuit [2].

3.2 Materials for Dye-sensitized Solar Cells

***Oxide Semiconductor*:** DSSCs adopt oxide semiconductor materials such as TiO_2 [1-3, 5] and ZnO [6, 7] as dye molecule supporting medium. TiO_2 is widely used for its high refractive index, excellent charge transport, and corrosion resistance. Anatase, rutile and brookite are obtainable forms of TiO_2 crystalline structure. The anatase structure with bandgap of 3.2 eV is preferred in DSSCs because its ability to be fabricated at lower temperatures, higher surface area per unit volume and packing density compared to other crystal types [8]. The most common type of TiO_2 film is porous structure composed of interconnected nanoparticles as shown in Figure 3-3 (a) because of larger surface area for dye adsorption on TiO_2 surface. A general way of fabrication

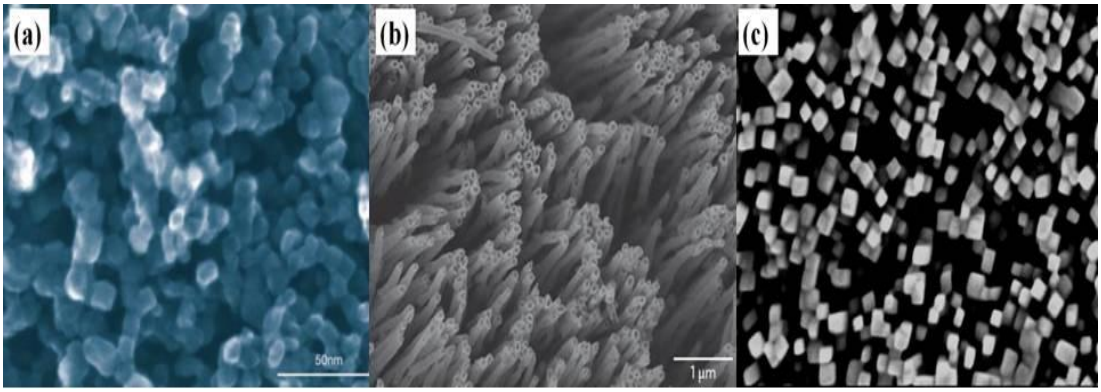

Figure 3-3. Various TiO_2 film morphology: (a) nanoporous film (Ref. [3]), (b) nanotube film (Ref. [9]) (c) nanowire film (Ref. [10]).

for TiO_2 porous film is to implement doctor blading with TiO_2 slurry, controlling the thickness of film by tape attached to substrate. Then, the TiO_2 film are subjected to annealing process at 450 ℃ or 500℃ to burn out organic materials in the slurry and to make interconnection between TiO_2 nanoparticles and the film to be formed in anatase crystal structure. Nanostructures such as nanotubes and nanowires as shown in Figure 3.3 (b) and (c) are also possibilities as photoelectrodes and might have enhanced electron diffusion coefficient and life time.

Dye: The dye molecule and its sensitization are important starting point of light-to-electricity conversion in DSSC system. The common dyes consist of polypyridyl complexes of ruthenium or osmium. The general structure of efficient dyes can be expressed as $ML_2(X)_2$ where L is 2,2'-

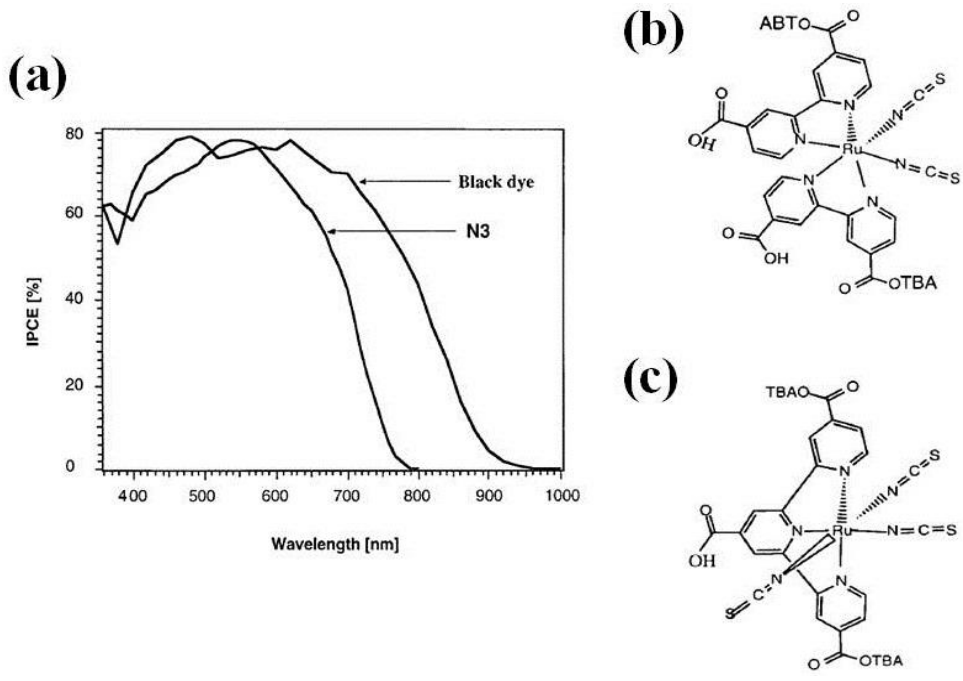

Figure 3-4. (a) Incident photon to charge carrier efficiency of N3 and Black dye (b) molecular structure of N3 dye (c) molecular structure of Black dye (Ref. [11]).

bipyridyl-4,4'-dicarboxilic acid, M is Ru or Os and X is halide, cyanide, thiocyanate or water substituent [11-13].

Figure 3-4 represents incident photon to current efficiency and molecular structure of N3 and Black dye that are well-known for DSSCs market. These molecules have Ru in the center of the structure with carboxylated bipyridyl ligand. N3 dye absorbs light upto 750nm in Figure 3-4 (a). Another Ru polypyridyl complex is illustrated in Figure 3-5 (c). It is called "Black dye" and the dye absorbs light more in the IR range (upto ~920 nm) in comparison with N3 dye [11]. This black dye is close to an ideal dye that has 900 nm as its absorption threshold wavelength and 1.4 eV band gap [11].

Optical transitions under incident light occur via MLCT (metal to ligand charge transfer) that electrons from Ru metal are transferred to the π^* orbital of the carboxylated bipyridyl ligand in forward reaction as represented in Figure 3-5. Backward reaction takes place from Ti_s^{4+} to the Ru atom directly [2].

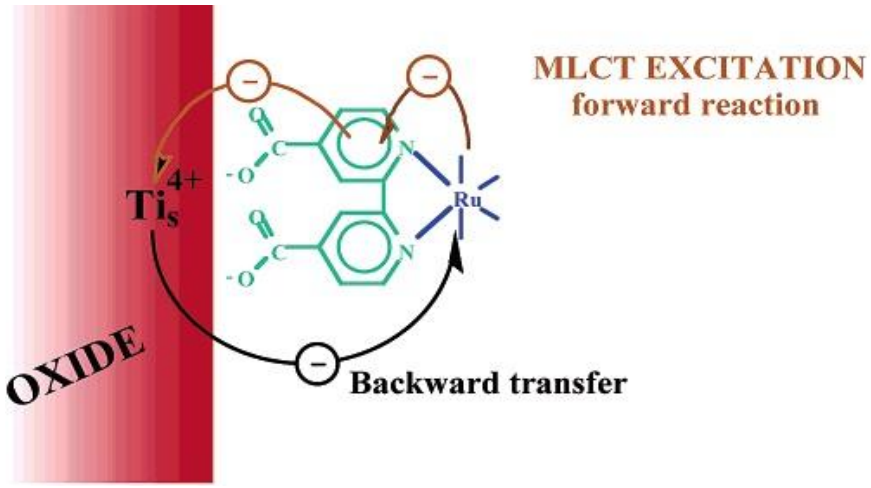

Figure 3-5. Schematic of metal to ligand charge transfer involving the interface at TiO_2/dye molecules in DSSCs [2].

Electrolyte: The electrolyte is the medium necessary for transferring electron from counter electrode to oxidized dye molecules. Since the research of Grätzel et al. in 1991, I^-/I_3^- redox couple -based liquid electrolyte has been popular [1]. Other redox couples such as Br^-/Br_2, SCN^-/SCN_2, $SeCN^-/SeCN_2$, have been suggested but those are less successful due to energy level mismatch and their lower diffusion coefficients in the comparison with that of I^-/I_3^- redox ion. Selection of the solvent for liquid electrolyte is important for dissolution and diffusion of the redox couples [5, 14-15]. Organic solvents like acetonitrile and 3-methoxypropionitrile are generally used for good dissolution and diffusion of redox ions and resulting good performance of DSSCs. Moreover, further improvement can be observed with addition of electric additives such as 4-tert-butylpyridine and cations such as imidazolium derivatives and Li^+ ion in voltage and in photocurrent, respectively [5, 16]. However, use of organic solvents does not guarantee long term performance of DSSCs. Leakage and volatilization canoccurr from DSSCs with corrosion against the sealing material by electrolyte. In order to resolve these problems, other types of electrolytes have been developed. Ionic liquids exhibit excellence in chemical and thermal stability, lower vapor pressure, nonflammability and ionic conductivity. Wang et al. reported remarkable light-to-electricity conversion efficiency of 7.5-8.3 % with 1-etyl-3methylimidazolium selenocyanate (EMISeCN) [17]. However, ionic liquid-based DSSCs still experience leakage and volatilization from its cells. Solid state electrolyte could be the alternatives in this aspect. Studies have been done with inorganic hole transport materials (HTMs) like CuI, CuSCN and organic hole transport materials like spiro-OMeTAD, polyaniline and PEO (poly ethylene oxide) containing iodide/triiodide redox couple. These HTMs have advantages in leakage and volatilization but disadvantages have been investigated. Inorganic HTMs show poor stability and organic HTMs have the weaknesses of poor intrinsic conductivity, incomplete penetration through nanostructured photo electrode and higher recombination [18-22]. In addition to these, DSSCs with gel electrolyte, namely, quasi-solid state electrolyte have been reported with comparable

conversion efficiency to DSSCs with liquid electrolyte owing to improved conductivity and stability [23].

Counter electrode: Electrons from the external circuit are conducted through the counter electrode within DSSC system. The counter electrode enables triiodides in electrolyte with transferred electrons to be reduced to iodides. Platinum has generally been employed because of its superior conductivity and catalytic reaction on triiodides for their reduction. However, since Pt is an expensive materials, other research groups have focused on finding alternatives. Promising candidates suggested are carbon materials such as carbon powder, carbon nanotubes and conducting polymers such as polythiopene and polypyrrole [24-28]. Several examples are shown in Figure 3-6. Unfortunately, the performance of these materials as a counter electrode could not exceed that of a conventional planar platinum electrode in DSSC system.

Pt electrodes have been fabricated by sputtering, thermal decomposition, electro-deposition and electron beam evaporation [13, 29-33]. The attempts to improve Pt electrodes themselves have been carried out in order to increase the reactivity and resulting in a more

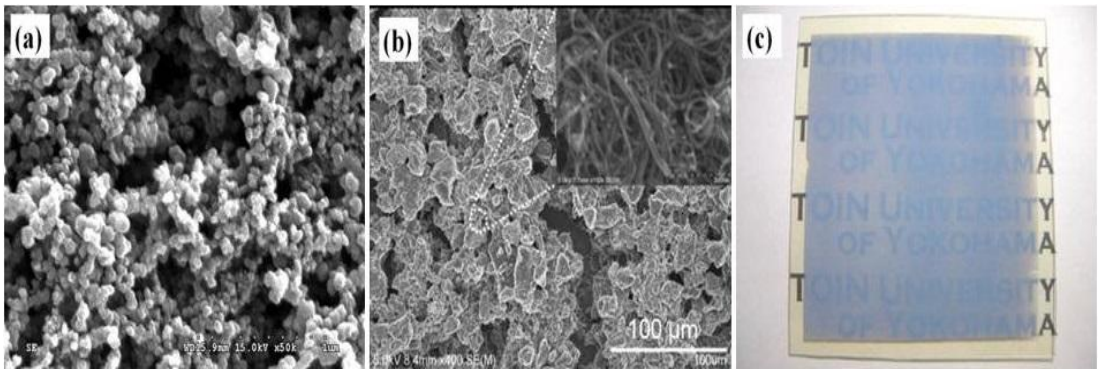

Figure 3-6. Surface morphologies of various counter electrodes: (a) activated cabon (Ref. [17]), (b)multi-wall carbon nanotube (Ref. [18]) and (c) polythiophene composite counter electrodes (Ref. [19]).

efficient counter electrode. Morphological and structural modification have been tried, for example, by using additives into the base solution used for electrodeposition or controlling sputtering conditions. Patterned masks have been used to obtain net-like Pt electrodes as well [29-30, 32-33]. Resulting films have shown improved performance over the standard planar platinum as counter electrode for DSSCs.

3.3 Motivation of Research

As mentioned above, dye-sensitized solar cells (DSSCs) are conventionally composed of three main components: 1) the photoanode electrode incorporating a semiconductor oxide such as TiO_2 or ZnO with adsorbed photo-reactive dye molecules on its surface, 2) electrolyte with redox couples such as I^-/I_3^- , and 3) counter electrode for which a platinized electrode is conventionally used [1, 34]. Since efficient solar cells were first demonstrated by Grätzel in 1991 [1], much research has been performed in pursuit of higher efficient DSSCs. For the first component, novel structures such as nanotubes and nanowires [6, 9] have proved favorable in obtaining higher surface area and longer life time of electrons for photoanode. For the second component, more efficient dye molecules which absorb a wider range of light energy thus generating more electrons by incident photons have been also been developed [13].

For more efficient DSSCs, component 3), the counter electrode must also be investigated and improved. The counter electrode in DSSCs plays a significant role in reducing I_3^- in close proximity to the surface of the electrode and conducting electrons from the external circuit to provide electrons to oxidized dye molecules for regeneration. Since platinum, which is considered as conventional material for counter electrode due to its high conductivity and excellent catalytic activity, is expensive, several research groups have focused on finding alternatives and have

suggested the replacement of platinum. Promising candidates include carbon materials such as carbon powder, [24] carbon nanotubes [35] and conducting polymers such as polythiopene [27] and polypyrrole [28]. However, the performance of these materials as a counter electrode could not outdo that of an ordinary planar platinum electrode in DSSCs [24, 27, 28, 35].

To date, Pt electrodes have been fabricated by sputtering [13, 29, 30, 36], thermal decomposition [31], electrodeposition [32, 33, 37] and electron beam evaporation [41]. However, the fabrications that have carried out by those groups have been only for Pt planar electrodes. Hence, in order to achieve highly chemical reactive and efficient counter electrode, morphological and structural modification have been tried, for example, by using additives into the base solution used for electrodeposition [32, 33] and controlling sputtering conditions [30]. Patterned masks have been used to obtain net-like Pt electrodes as well [29]. Resulting films have shown improved performance over the standard planar platinum as counter electrode for DSSCs [29, 30, 32, 33].

Another method to obtain morphological and structural change of the film is to "sculpt" the film. Sculpture thin films (STFs) are created by obliquely directed physical deposition and, by self-shadowing, STFs show porous and columnar structure [38]. Due to its high surface area and valuable optical properties, STFs have been used in optical or biological applications [38-40]. In the rest of this chapter, a highly structured sculptured platinum thin film was made by oblique angle electron beam evaporation and these sculptured platinum nanowire electrodes were incorporated as counter electrode for DSSCs. The morphology of the electrodes was compared to bare FTO and Pt planar electrodes made by evaporation. In addition, the effects of chloroplatinic acid treatment on the surface of different counter electrodes also were investigated. The performance of DSSCs with these counter electrodes was evaluated under AM 1.5 illumination.

3.4 Experimental Section

3.4.1 Preparation of Pt Counter Electrodes

≈40 nm thick Pt planar counter electrodes (PtPs) were deposited by electron beam evaporator on FTO (fluorinated tin oxide) glasses. Prior to evaporation, the FTO glass was cleaned with sonication in isopropyl alcohol for 10 min and then rinsed with deionized water under sonication again. The base pressure of the chamber for deposition was 2 x 10^{-6} Torr and the deposition rate was 0.4 Å/s. Pt STFs were fabricated by electron beam evaporator with 5° vapor incidence angle (χ_v) and 4.7 Å/s of deposition rate on FTO as shown in Figure 3-7.

The thickness of the Pt STF was ≈230 nm and labeled PtW. For the comparison of

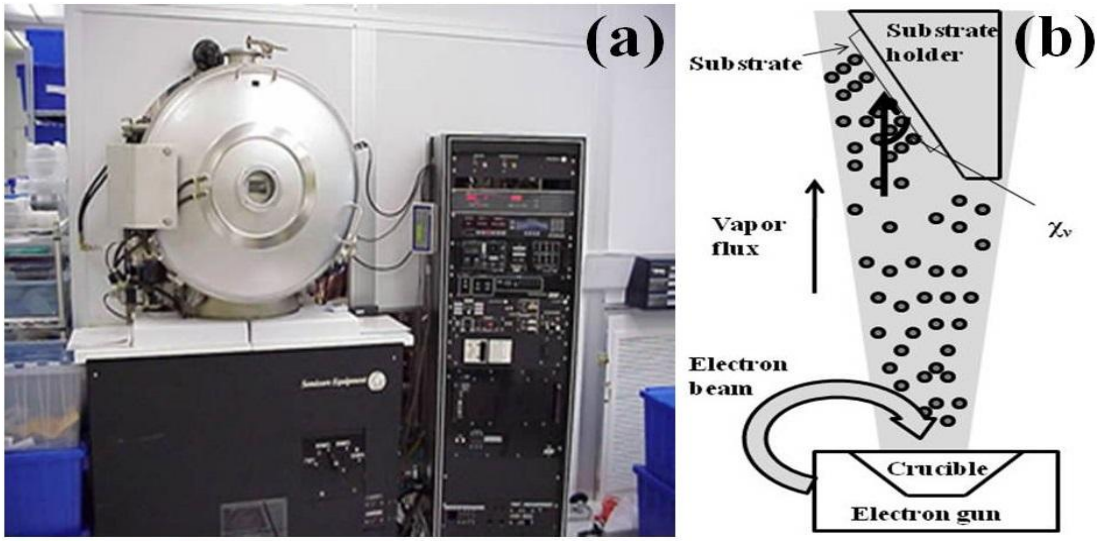

Figure 3-7. Fabrication of sculptured platinum thin films: (a) electron beam evaporator system (b) schematic showing the fabrication of sculptured thin films by electron beam evaporation (χ_v: incident flux angle).

performance, six different counter electrodes were prepared. Along with bare FTO electrode, the planar Pt electrode (PtP), and the STF platinum electrode (PtW), each of these three kinds were acid-treated with 5mM chloroplatinic acid solution (H_2PtCl_6 in isopropyl alcohol) and were subjected to annealing at 385 ℃ for 15 min in ambient air. The bare FTO glass, PtP and PtW samples that received this acid treatment are labeled as FTO-a, PtP-a, and PtW-a, respectively.

3.4.2 Preparation of Photoelectrodes and Cell Assembly

The TiO_2 photoelectrodes were prepared with commercial paste (DSL 18 NR-T, Dyesol) on FTO glass by "doctor blade method." FTO glass was cleaned with the same procedure as that of the counter electrodes. The commercial paste electrodes were annealed at 450 ℃ for 30 min in air to induce the transformation to the anatase phase. Through repetition of the deposition process, about 16-㎛-thick films were obtained. Then, the prepared TiO_2 films were immersed 0.3 mM N-719 (Ruthenium 535-bis TBA, Solaronix) in 1:1 acetonitrile/*tert* butanol solution for 48 h. A rinsing process with acetonitrile was carried out after taking the TiO_2 electrodes out of N-719 solution. The prepared photoelectrodes were assembled with the six different types of counter electrodes prepared above, keeping the space between the two electrodes at ≈40 ㎛ thickness, by using a stretched Parafilm. Commercial liquid electrolyte (EL-HPE, Dyesol) was injected into the gap between the electrodes and after connection to the external circuit, cells with 0.25 cm^2 active area were measured under AM 1.5 illumination.

3.4.3 Measurement of Symmetrical Cells with Various Counter Electrodes

The six different counter electrodes were assembled as symmetrical cells for electrochemical impedance spectroscopy (EIS) in order to evaluate charge transfer resistance and series resistance. The active area was 0.25 cm^2 and a stretched Parafilm (≈40 ㎛) was used as a spacer. The scan range of frequency was 0.01 ~ 3×10^5 Hz and the spectroscopy was obtained at zero dc bias with 10 mV of ac amplitude.

3.5 Results & Discussion

The surface of bare FTO has a rough morphology similar to previous observations; it appears to be deeply faceted with grains on the order of 100 to 200 nm as shown in Figure 3-8 (a) [32, 36]. With chloroplatinic acid treatment, theFTO surface is coated by additional Pt particles (FTO-a), which are reduced by thermal decomposition from chloroplatinic acid solution (Figure 3-8 (b)). The surface morphology of FTO-a is not significantly changed compared to that of FTO because the Pt particles are much smaller than the grains and appear to be scattered on the surface. However, agglomeration between Pt particles with reduced Pt particles onto FTO surface is observed and the crevices between FTO grains appear to be filled with the Pt particles. In AFM measurements, the RMS roughness decreased from 17.9 nm to16.8 nm after the acid wash, supporting this idea of filling in of the crevices. PtP is prepared by electron beam evaporation on FTO and its morphology imitates that of bare FTO. The resulting surface of the PtP shows a slightly rougher morphology than that for bare FTO (19.1 nm). Like FTO-a, PtP was also subjected to H_2PtCl_6 treatment. Reduced Pt particles are present on the surface of Pt planar film and its agglomerated Pt particles are observed, with the particles filling the gaps between

platinum morphology as shown in Figure 3-8 (d). This PtP-a sample shows lower RMS roughness than that of PtP (19.1 → 18.1 nm). A sculptured Pt electrode is shown in Figure 3-8 (e). Sculptured Pt is grown vertically in the shape of nanowires by evaporation at an oblique angle (PtW) with a lot of pores around Pt columns and, due to its structure, the roughness of PtW sample is considerably enhanced in comparison with PtP samples (19.1 → 44.4 nm). Figure 3-8 (f) shows the surface of PtW after chloroplatinic acid treatment, namely, PtW-a. Unlike for the planar Pt or bare FTO samples, in Figure 3-8 (f), any visible difference is not observed in comparison with PtW (Figure 3-8 (e)). However, the reduction in the RMS roughness of PtW-a (44.4 → 39.4 nm) suggests that the presence of thermally decomposed Pt particles some minor filling of crevices with the Pt particles.

Figure 3-9 shows electrochemical impedance spectroscopy of the symmetrical cells adopting the six different electrodes. Among the data, the diameter of the semicircle at high

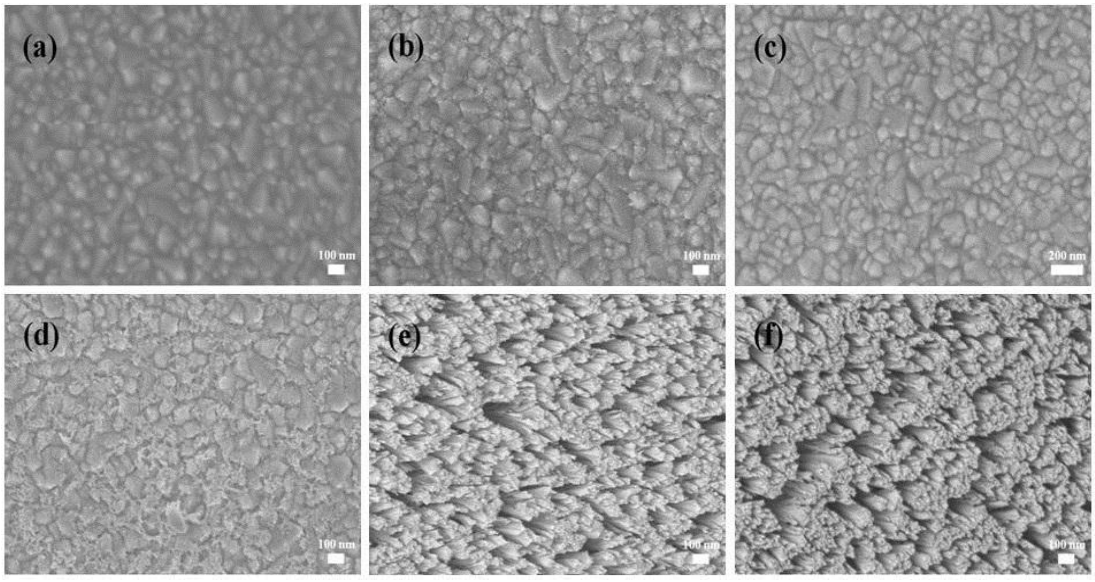

Figure 3-8. Surface morphology of various counter electrodes: a) FTO glass without acid wash, b) FTO glass with acid wash, c) planar Pt on FTO, d) planar Pt on FTO with acid wash, e) sculptured Pt on FTO and f) sculptured Pt on FTO with acid wash.

frequency corresponds to the charge transfer resistance (R_{ct}) in the inset of Figure 3-9 and this is one of the critical factors needed to evaluate the performance of the counter electrodes [10, 13, 20]. With respect to the R_{ct}, the Pt film deposited by normal evaporation or thermal decomposition of the acid on FTO causes more than 100 times improvement in comparison with bare FTO. The R_{ct}s of FTO-a and PtP were 0.786 Ω*㎠ and 0.578 Ω·㎠, respectively. PtP shows more chemical reactivity with H_2PtCl_6 solution treatment (0.509 Ω·㎠). In the case of PtW, five times more charge transfer reactivity is measured (0.121 Ω·㎠), which we suspect originates from a rougher and more porous nanowire structure. Furthermore, nearly fourteen times more charge transfer reactivity (0.04025 Ω·㎠) is observed on the sculptured Pt electrode (PtW-a) with

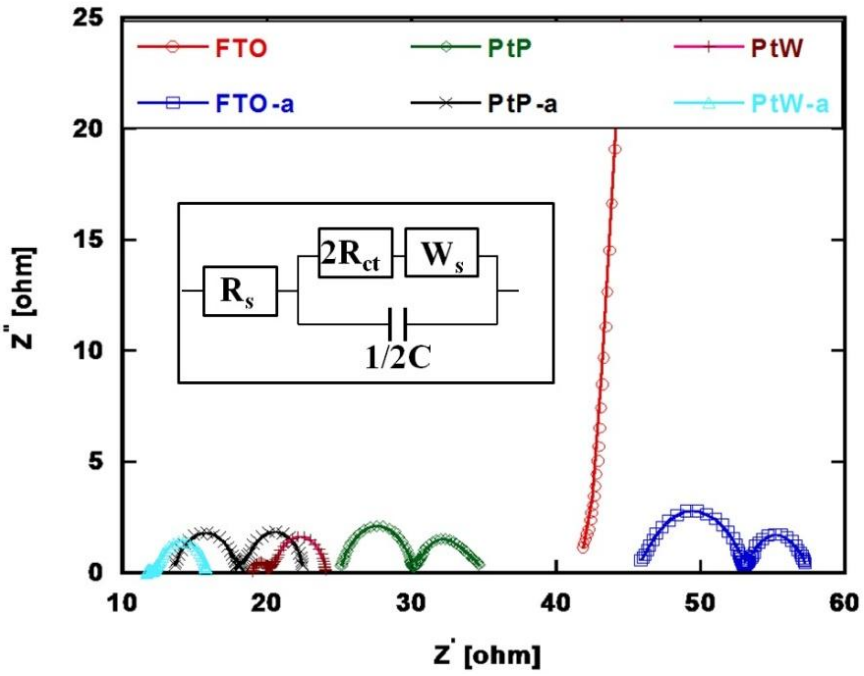

Figure 3-9. Nyquist plots of electrochemical impedance spectroscopy from the symmetrical cells with various electrodes at 0 dc vias: FTO, FTO-a, PtP, PtP-a, PtW and PtW-a (inset R_s: series resistance, R_{ct}: charge transfer resistance, W: Warburg impedance and C:double layer capacitance).

chloroplatinic acid treatment than on the FTO-a electrode. In addition to this, variation of EIS in R_s, which is described by the resistance of the electrodes, is observed in Figure 7-3 unlike other previous experiments [32, 33]. The series resistance of the electrodes is affected by the thickness and structure of the Pt films by evaporation and acid treatment. As thickness of the film increases, the film has a lower R_s and, with acid treatment, the resistance further decreases. However, since DSSCs are one of electrochemical cell and electrodes react with the surface of electrolyte, chemical reactivity of surface of electrode which is defined with R_{ct} is the main contributor to the performance of whole cells regardless of the series resistance of electrodes. Previous experiments done by Fang et al. [36] demonstrate the fact that sheet resistance of counter electrode does not have an influence of the performance of DSSCs.

Figure 3-10 and Table 3-2 show J-V characteristics and parameters of DSSCs incorporating the six different kinds of the counter electrodes. The DSSCs with bare FTO shows very poor performance as shown in Figure 3-10 and Table 3-2. FTO material itself does not act as good catalyst for the liquid electrolyte. However, when adopting either acid solution or evaporation of Pt, the entire performance of DSSCs is abruptly improved. Only a few tens of

Sample Name	**R_s [Ω*㎠]**	**R_{ct} [Ω*㎠]**
PtW-a	2.92	0.04025
PtW	4.75	0.121
PtP-a	3.43	0.509
PtP	6.31	0.578
FTO-a	11.58	0.786
FTO	10.86	3.47e2

Table 3-1. Series resistances and charge transfer resistancesof six different kinds of counter electrodes.

nanometers of platinum demonstrate excellent catalytic activity as a counter electrode as shown by the EIS data and thus the performance of DSSCs are highly enhanced in FTO-a and PtP cell. These results are consistent with large increase in R_{ct} from EIS above and the results of previous experiments by other group [36, 41]. More importantly, the DSSCs show a marked improvement with the adoption of the nanowire Pt structure. In particular, the increase in J_{sc} is remarkable. When Pt nanowire film is used for counter electrode, DSSCs shows better performance than the planar platinum electrode with and acid wash (PtP-a), yielding a current density up to about 9.776 mA/cm^2 and an efficiency up to 5.1 %. The DSSC made with the nanowire Pt counter electrode plus acid wash (PtW-a) demonstrates a 5.63 % efficiency with highest J_{sc} among the measured

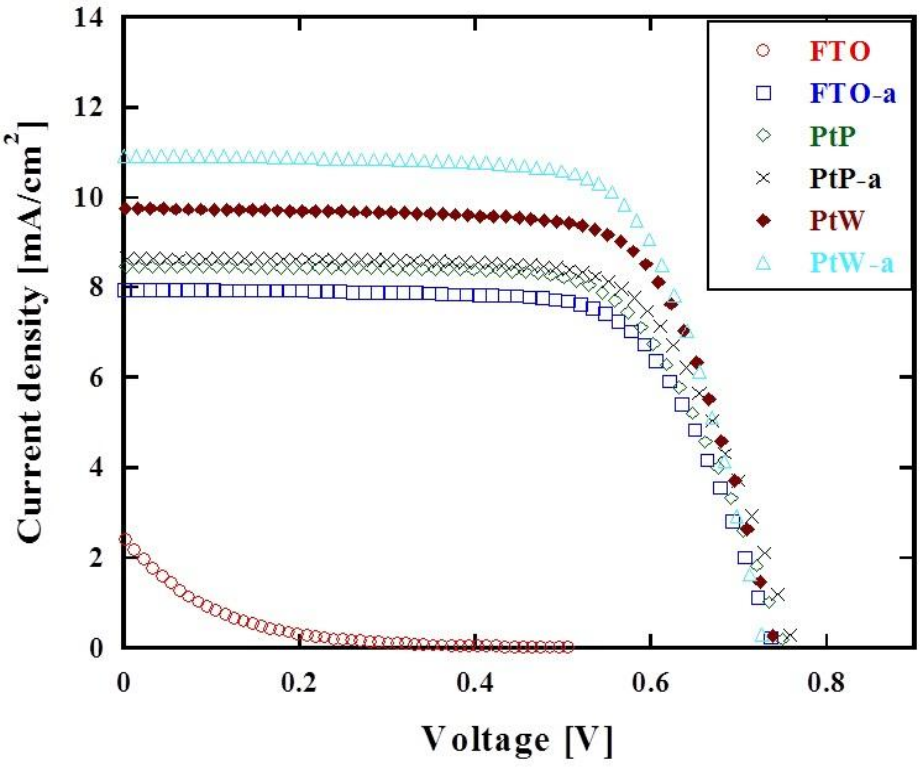

Figure 3-10. J-V characteristics of DSSCs adopting the counter electrodes, FTO, H_2PtCl_6 – treated FTO (FTO-a), Planar Pt (PtP), H_2PtCl_6 –treated PtP(PtP-a), Sculptured Pt (PtW) and H_2PtCl_6 –treated and sculptutred Pt (PtW-a). These cells are tested with 0.25 cm^2 active area under AM 1.5 (100 mW/cm^2).

DSSCs. We believe this is due to the rougher nanowire structure which increases the active surface area for the charge exchange and more area to bond the Pt agglomerates from the acid wash.

Sample Name	J_{sc} [mA/cm^2]	V_{oc} [V]	FF	η [%]
FTO	2.46	0.542	0.658	0.087
FTO-a	7.949	0.739	0.695	4.06
PtP	8.468	0.750	0.678	4.31
PtP-a	8.644	0.762	0.685	4.49
PtW	9.776	0.738	0.707	5.1
PtW-a	10.94	0.729	0.707	5.63

Table 3-2. Characteristic parameters of the DSSCs.

3.6 Summary

A platinum nanowire sculptured thin film which is porous and columnar film was made by electron beam evaporation with a 5 incident flux angle. The platinum nanowire film shows 44.4 nm higher RMS roughness than that of conventional Pt planar film. When evaluating symmetrical electrodes using EIS, the Pt nanowire electrodes show an R_{ct} of 0.121 Ω·㎠ which is five times less in comparison with that of Pt planar electrodes. Moreover, with H_2PtCl_6 solution treatment, a further improvement in R_{ct} down to 0.04025 Ω·㎠ is observed. The performance of DSSCs made with the Pt nanowire film as a counter electrode was 5.1 %, which is an 18.3 %

improvement in efficiency compared to a DSSC made with a Pt planar film and, with the acid treatment, the efficiency using the Pt nanowire counter electrode is enhanced to 5.63 %.

3.7 Chapter 3 References

[1] B. O'Regan, M. Grätzel, A low-cost, high-efficiency solar cell based on dye-sensitized colloidal TiO_2 films, *Nature* Vol. 353 24 Oct (**1991**) 737-740.

[2] M. Grätzel, Solar energy conversion by dye-sensitized photovoltaic cells, *Inorganic Chemistry* Vol. 44 No. 20 (**2005**) 6841-6851.

[3] M. Grätzel, Photoelectrochemical cells, *Nature* Vol. 414 15 Nov (**2001**) 338-344.

[4] B. A. Gregg, Excitonic solar cells, *The Journal of Physical Chemistry B* Vol. 107 (**2003**) 4688-4698.

[5] J. Wu, Z. Lan, S. Hao, P. Li, J. Lin, M. Huang, L. Fang, Y. Huang, Progress on the electrolytes for dye-sensitized solar cells, *Pure and Applied Chemistry* Vol. 80 (**2008**) 2241-2258.

[6] M. Saito, S. Fujihara, Large photocurrent generation in dye-sensitized ZnO solar cells, *Energy & Environmental Science* Vol. 1 (**2008**) 280-283.

[7] M. Law, L. E. Greene, J. C. Johnson, R. Saykally and P. Yang, Nanowire dye-sensitized solar cells, *Nature Materials* Vol. 4 June (**2005**) 455-459.

[8] N. Park, J. van de Lagemaat, A. J. Frank, Comparison of dye-sensitized rutile- and anatase-based TiO_2 solar cells, *Journal of Physcal Chemistry B* Vol. 104 (**2000**) 8989-8994.

[9] O. K. Varghese, M. Paulose, C. A. Grimes, Long vertically aligned titania nanotubes on transparent conducting oxide for highly efficient solar cells, *Nature Nanotechnology* Vol. 4 September (**2009**) 592-597.

[10] X. Feng, K. Shankar, O. K. Varghese, M. Paulose, T. J. Latempa, C. A. Grimes, Nanowire arrays grown directly on transparent conducting oxide coated glass: synthesis details and applications, *Nanoletters* Vol. 8 No. 11 (**2008**) 3781-3786.

[11] M. Grätzel, Perspectives for dye-sensitized nanocrystalline solar cells, *Progress in Photovoltaics: Research and Applications* Vol. 8 (**2000**) 171-185.

[12] T. A. Heimer, C. A. Biognozzi, G. J. Meyer, Molecular level photovoltaics: the electrical properties of metal cyanide complexes anchoered to titanium dioxide, *The Journal of Physical Chemistry* Vol. 97 No. 46 (**1993**) 11987-11994.

[13] M. K. Nazeeruddin, A. Kay, I. Rodicio, R. Humphyr-Baker, E. Müller. P. Liska, N. Vlachopoulos, M. Grätzel, cis-X_2Bis(2,2′-bipyridyl-4,4′-dicarboxylate)ruthenium(Ⅱ) charge-transfer sensitizers (X = Cl^-, Br^-, I^-, CN^-, and SCN^-) on nanocrystalline TiO_2 electrodes, *Journal of the American Chemical Society* Vol. 115 No. 14 (**1993**) 6382-6390.

[14] Z. Wang, K. Sayama, H. Sugihara, Efficient Eosin Y dye-sensitized solar cells containing Br^-/Br_3^- electrolyte, *The Journal of Physical Chemistry B* Vol. 109 (**2005**) 22449-22455.

[15] B. V. Bergeron, A. Marton, G. Oskam, G. J. Meyer, Dye-sensitized SnO_2 electrodes with iodide and pseudohalide redox mediators, *The Journal of Physical Chemistry B* Vol. 109 (**2005**) 937-943.

[16] A. Kay, M. Grätzel, Low cost photovoltaic modules based on dye sensitized nanocrystalline titanium dioxide and carbon powder, *Solar Energy Materials and Solar Cells* Vol. 44 (**1996**) 99-117.

[17] P. Wang, S. M. Zakeeruddin, J. E. Moser, R. Humphry-Baker, M. Grätzel, A Solvent-free, $SeCN^-/(SeCN)_3^-$ based ionic liquid electrolyte for high-efficiency dye-sensitized nanocrystalline solar cells, *Journal of the American Chemical Society* Vol. 126 (**2004**) 7164-7165.

[18] Q. B. Meng, K. Takahashi, X. T. Zhang, I. Sutanto, T. N. Rao, O. Sato, A. Fujishima, Fabrication of an efficient solid –state dye-sensitized solar cells, *Langmuir* Vol. 19 (**2003**) 3572-3574.

[19] E. V. A. Premalal, G. R. R. A. Kumara, R. M. G. Rajapakse, M. Shimomura, K. Murakami, A. Konno, Tuning chemistry of CuSCN to enhance the performance of TiO_2/N719/CuSCN all-solid-state dye-sensitized solar cell, *Chemical Communications* Vol. 46 (**2010**) 3360-3362.

[20] I. K. Ding, N. Tétreault, J. Brillet, B. E. Hardin, E. H. Smith, S. J. Rosenthal, F. Sauvage, M. Grätzel, M. D. Mcgehee, Pore-filling of spiro-OMeTAD in solid-state dye sensitized solar cells: quantification, mechanism, and consequences for device performance, *Advanced Functional Materials* Vol. 19 (**2009**) 1-6.

[21] S. Tan, J. Zhai, M. Wan, Q. Meng, Y. Li, L. Jiang, D. Zhu, Influence of small molecules in conducting polyaniline on the photovoltaic properties of solid-state dye-sensitized solar cells, *The Journal of Physical Chemistry B* Vol. 108 (**2004**) 18693-18697.

[22] T. Stergiopoulos, L. M. Arabatzis, G. Katsaros, P. Falaras, Binary polyethylene oxid/titania solid-state redox electrolyte for highly efficient nanocrystalline TiO_2 photoelectrochemical cells, *Nano Letters* Vol. 2 No. 11 (**2002**) 1259-1261.

[23] J. Wu, S. Hao, Z. Lan, J. Lin, M. Huang, Y. Huang, L. Fang, S. Yin, T. Sato, A Thermoplastic gel electrolyte for stable quasi-solid state dye-sensitized solar cells, *Advanced Functional Materials* Vol. 17 (**2007**) 2645-2652.

[24] K. Imoto, K. Takahashi, T. Yamaguchi, T. Komura, J. Nakamura, K. Murata, High-performance carbon counter electrode for dye-sensitized solar cells, *Solar Energy Materials & Solar Cells* Vol. 79 (**2003**) 459-469.

[25] H. S. Lee, H. Y. Lee, S. Y. Ahn, K. H. Kim, J. Y. Kwon, Improved carbon counter electrodes for dye sensitized solar cells, *Advanced Materials Research* Vol. 31 (**2008**) 176-178.

[26] W. J. Lee, E. Ramasamy, D. Y. Lee, J. S. Song, Efficient dye-sensitized solar cells with catalytic multiwall carbon nanotube counter electrodes, *Applied Materials & Interfaces* Vol. 1 No. 6 (**2009**) 1145-1149.

[27] T. Muto, M. Ikegami, T. Miyasaka, Polythiophene-based mesoporous counter electrodes for plastic dye-sensitized solar cells, *Journal of the Electrochemical Society* Vol. 157 No. 8 (**2010**) B1195-B1200.

[28] S. S. Jeon, C. Kim, J. Ko, S. S. Im, Spherical polypyrrole nanoparticles as a highly efficient counter electrode for dye-sensitized solar cells, *Journal of Materials Chemistry* Vol. 21 (**2011**) 8146-8151.

[29] L. Lin, P. Nien, C. Lee, K. Tsai, M. Yeh, R. Vittal, K. Ho, Low-temperature flexible photoanode and net-like Pt counter electrode for improving the performance of dye-sensitized solar cells, *The Journal of Physical Chemistry C* Vol. 114 (**2010**) 21808-21815.

[30] Y. Lee, C. Chen, L. Chong, C. Chen, Y. Liu, C. Chi, A platinum counter electrode with high electrochemical activity and high transparency for dye-sensitized solar cells, *Electrochemistry Communications*, Vol. 12 (**2010**) 1662-1665.

[31] Q. Wang, S. Ito, M. Grätzel, F. Fabregat-Sntiago, I. Mora-Seró, J. Bisquert, T. Bessho, H. Imai, Characteristics of High Efficiency Dye-Sensitized Solar Cells, *Journal of Physical Chemistry B*, Vol. 110 (**2006**) 25210-25221.

[32] C. Lin, J. Lin, C. Wan, T. Wei, High-performance and low platinum loading electrodeposited-Pt counter electrodes for dye-sensitized solar cells, *Electrochimica Acta*, Vol. 56 (**2011**) 1941-1946.

[33] H. Lin, Feng Hao, C. Lin, J. Li, Highly catalytic active nanostructured Pt electrodes for dye-sensitized solar cells prepared by low temperature electrodeposition, *Functional Materials Letters*, Vol. 4 (**2011**) 7-11.

[34] M. Grätzel, Dye-sensitized solar cells, *Journal of Photochemistry and Photobiology C: Photochemistry Reviews* Vol. 4 (**2003**) 145-153.

[35] X. Mei, S. Cho, B. Fan, J. Ouyang, High-performance dye-sensitized solar cells with gel-coated binder-free carbon nanotube films as counter electrode, *Nanotechnology* Vol. 21 (**2010**) 1-9.

[36] X. Fang, T. Ma, G. Guan, M. Akiyama, E. Abe, Performance characteristics of dye-sensitized solar cells based on counter electrodes with Pt films of different thickness, *Journal of Photochemistry and Photobiology A: Chemistry* Vol. 164 (**2004**) 179-182.

[37] S. Kim, Y. Nah, Y. Noh, J. Jo, D. Kim, Electrodeposited Pt for cost-efficient and flexible dye-sensitized solar cells, *Electrochimica Acta* Vol. 51 (**2006**) 3814-3819.

[38] S. Pursel, M. Horn, Prospects for nanowire sculptured-thin-film devices, *Journal of Vacuum Science & Technology B* Vol. 25 (**2007**) 2611-2615.

[39] H. Tan, O. Ezekoye, J. Schalie, M. Horn, A. Lakhtakia, J. Xu, W. Burgos, Biological Reduction of Nanoengineered Iron(III) Oxide Sculputured Thin Films, *Environmental Science & Technology* Vol. 40 (**2006**) 5490-5495.

[40] S. Pursel, M. Horn, A. Lakhtakia, Tuning of sculptured-thin-film spectral-hole filters by postdeposition etching, *Optical Engineering* Vol. 46 (**2007**) 040507-1-040507-3.

[41] A. Hauch, A. Georg, Diffusion in the electrolyte and charge-transfer reaction at the platinum electrode in dye-sensitized solar cells, *Electrochimica Acta* Vol. 46 (**2001**) 3457-3466.

Chapter 4

Plasmonic Enhancement of CO_2 Conversion to Methane using Sculptured Copper Thin Films Grown Directly on TiO_2

Reduction of atmospheric CO_2 and its conversion into fuels at the same time have been of interest to researchers who are eager to mitigate green house effects while simultaneously acquiring an alternate energy source. Conventional ways of obtaining useful fuels such as hydrogen, methane and ethane from the atmospheric CO_2 have been tried thermochemically, electrochemically or photocatalytically [1-8]. However, the thermochemical and electrochemical methods require heat concentrated by huge system and electricity, which is not sustainablefor CO_2 reduction. Adopting photocatalysts for CO_2 conversion appears to be more simple and attractive.

In this chapter, a brief history of CO_2 conversion into fuels by photocatalysts and an explanation of CO_2 conversion mechanism will be examined Materials for CO_2 conversion will be discussed in Chapter 4.1as well as a basic understanding of plasmonic effect by plasmonic metals and its role in photocatalysis for CO_2 conversion. Motivation on adopting sculptured copper thin films on TiO_2 will be presented in Chapter 4.2 while experimental information will be given in Chapter 4.3. Results of the experiments will be presented and discussed in Chapter 4.4 and Chapter 4.5 will summarize the main results.

4.1 Literature Review on CO_2 Conversion by Photocatalytic Semiconductors

4.1.1 CO_2 Conversion by Photocatalytic Semiconductors and TiO_2 Photocatalysts

After Halmann's initial work for CO_2 conversion based on electrochemical cells fabricated with p-type GaP in 1978 [5] Inoue et al. succeeded CO_2 conversion to hydrocarbon fuel by possible photocatalytic powders such as TiO_2, WO_3, ZnO and CdS as shown in Figure 4-1 [4]. Inoue et al. describe the CO_2 conversion mechanism by semiconductor catalysts as follow,

Generation of Electron-hole pairs

$$\text{catalyst} + h\nu \rightarrow \text{catalyst}^* (e^-_{cond} + h^+_{val}) \quad (4.1)$$

Oxidation

$$H_2O + 2h^+_{val} \rightarrow 1/2O_2 + 2H^+ \quad (4.2)$$

Reduction

$$CO_2\,(aq) + 2H^+ + 2e^-_{cond} \rightarrow HCOOH \quad (4.3)$$

$$HCOOH + 2H^+ + 2e^-_{cond} \rightarrow HCHO + H_2O \quad (4.4)$$

$$HCHO + 2H^+ + 2e^-_{cond} \rightarrow CH_3OH \quad (4.5)$$

$$CH_3OH + 2H^+ + 2e^-_{cond} \rightarrow CH_4 + H_2O \quad (4.6)$$

where catalyst* is the excited catalyst by light energy, $h\nu$, e^-_{cond} is the electron in conduction band and h^+_{val} is the hole in valence band of catalyst [4]. A multistep reduction process is required for CO_2 conversion as represented reaction equation (4.1) to (4.6).

In the experiment with semiconductor photocatalysts depicted in Figure 4.1, all the catalysts except for WO_3 produced HCHO and CH_3OH under filtered illumination which are the chemicals are necessary for obtaining CH_4. Yields of HCHO were ranged from 1×10^{-3} to 2×10^{-3} M and yields of CH_3OH were ranged from 2.3×10^{-4} to 53.5×10^{-4} M. In particular, TiO_2 catalysts showed no yields under the illumination with light wavelength longer than 500 nm [4].

Among these photocatalysts mentioned above, TiO_2 has been considered one of the most appropriate candidates for CO_2 conversion because of stability against corrosive reactants and

excellent oxidation properties. The CO_2 conversion into hydrocarbon fuels only by TiO_2 photocatalysts can be realized, but the hydrocarbon production rate of the fuels from CO_2 and water are small and the conversion can be activated within a limited wavelength range of light as reported above.

Several attempts for enhancement in CO_2 conversion by TiO_2 photocatalysts have been carried out. One of attempts implemented by research group was that nitrogen doping of TiO_2 materials [6, 9]. The resulting TiO_2 catalysts exhibited elongated range of absorption wavelength. Undoped TiO_2 materials usually show high absorption only within ultraviolet region (<400 nm) due to a bandgap of 3.2 eV for anatase TiO_2 but, after nitrogen doping, TiO_2 showed a larger absorption peak even within visible range, especially, in the range of 400 nm < λ < 500 nm. This

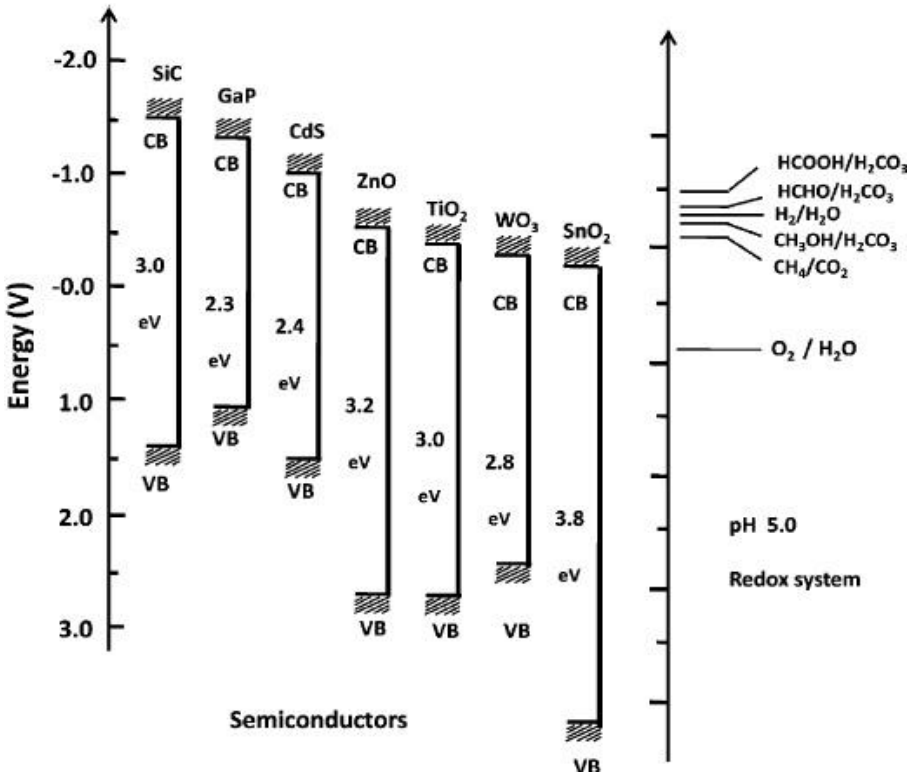

Figure 4-1. Conduction and valence band positions of various photocatalyst materials (Ref. [4, 10]).

improvement also leads an increase in the performance of catalysts [6, 9]. Another way of enhancing photocatalytic performance of TiO_2 materials was adopting nanostructure. Varghese et al. fabricated ~50 μm long TiO_2 nanotube catalysts by anodic oxidation of titanium. With a copper cocatalyst, the nitrogen-doped TiO_2 nanotubes produced hydrocarbons, including methane and others, at a rate of 104 $ppm \cdot cm^{-2} \cdot h^{-1}$.[8] Feng et al. reported a methane production rate of 25 $ppm \cdot cm^{-2} \cdot h^{-1}$ by using ~30 μm long TiO_2 nanotubes decorated with Pt nanoparticles via a microwave-assisted solvothermal approach [19]. Tan et al. achieved ~2.91 $ppm \cdot cm^{-2} \cdot h^{-1}$ by adopting TiO_2 nanorods decorated with Cu nanoparticles [20]. The other attempt was implemented with using cocatalysts. Various metals are usually chosen as cocatalysts such as Cu, Pt and Au. These metal cocatalysts help reactants to be adsorbed easily and to facilitate redox process [6-8, 11, 12]. Conventionally, previous research groups have incorporated these cocatalysts by sputtering [6], evaporation [11], wet impregnation method [7, 8, 11] or photoreduction [12]. These groups carried out cocatalyst deposition made of only small particles which appear to be ‘islands’ on the TiO_2 surface [6, 9].

4.1.2 Plasmonic Effect by Nanostructures

Nanostructures, such as nanowires and nanotubes have been used effectively for various materials in order to enhance the performance of a final application owing to their larger surface area or innate one-dimensional nature [6, 10, 13, 16, 19, 20, 22, 23, 29-32, 34].

In particular, metal nanostructures have unique optical properties due to a plasmonic effect. Nanostructured plasmonic metals feature strong interaction with the resonant frequency of incident photons via the excitation of surface plasmon resonance (SPR). Collective oscillation of valence electrons induced by resonant photons is established through the existence of frequency

matching between incident photons and surface electrons of a plasmonic metal [13]. The optical features, including resonant wavelength and SPR intensity, of plasmonic metals are different for different materials.

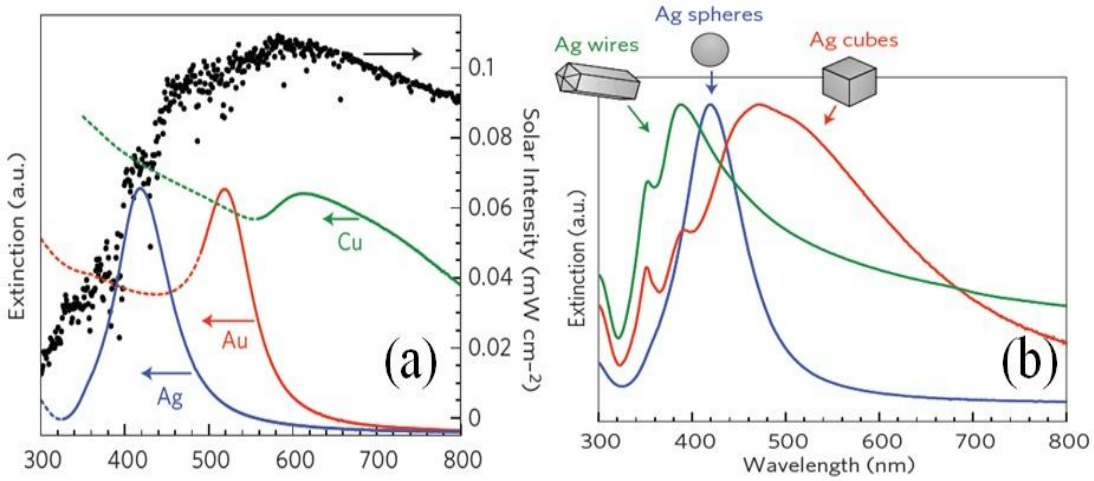

Figure 4-2. Plasmonic effect in various nanostructured metals: (a) Normalized extinction spectra of Ag, Au Cu nanoparticles with the intensity of solar radiation (black dots) (b) normalized extinction spectra depending on shape variation of Ag nanostructure (Ref. [13]).

Figure 4-2 (a) exemplifies different optical properties of various plasmonic metals. Plasmonic metals exhibit their own SPR in extinction spectra. Ag, Au and Cu interact with ultraviolet and visible photons as shown in Figure 4-2 (a). Moreover, the plasmonic behavior depends on the composition, size and shape of plasmonic metals. For example, extinction spectra of Ag can be controlled by changing its shape of wire, sphere or cube as shown in Figure 4-2 (b) [13].

SPR concentrates incoming photon energy at, or near, the surface of the nanostructure. Figure 4-3 (a) and (b) demonstrate the built-up intense and spatially non-homogeneous electric field surrounding a nanocube [13].

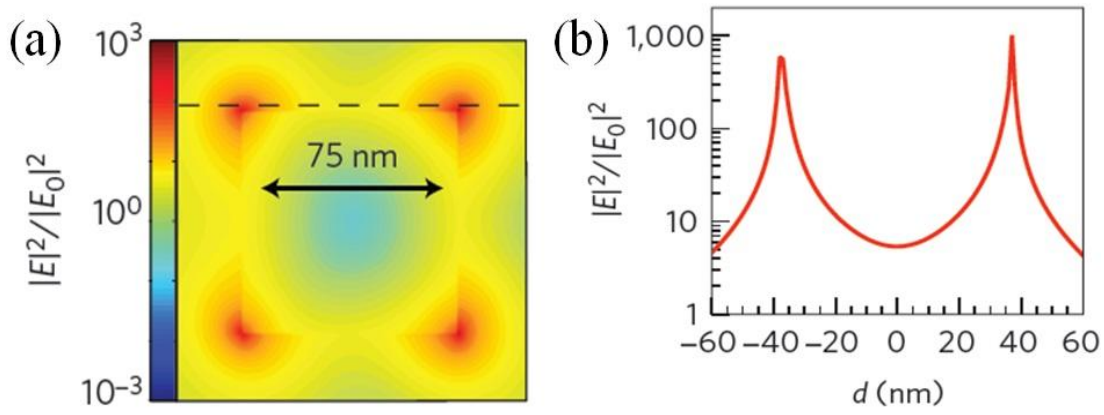

Figure 4-3. Unique features of plasmonic effect by Ag nanocube:(a) Spatial distribution of the SPR-induced enhancement of electric field intensity at the SPR peak wavelength (b) Enhancement in the electric field intensity at the SPR peak wavelength as a function of distance, d (Ref. [13]).

4.1.3 Energy Transfer Mechanisms through the Plasmonic Effect

Concentrated photon energy by SPR can be transferred to the materials that are in contact directly or indirectly to plasmonic nanostructures and this can contribute to improvement of photocatalytic performance via its energy transfer.

The energy transfer by the plasmonic effect is explained by three mechanisms. First, the energy through SPR is able to be injected to semiconductors from plasmonic metals at the semiconductor/plasmonic metal interface. This mechanism is called SPR-mediated charge injection [13]. An example of this is given in Figure 4-4. Figure 4-4 represents the schematic of an energy band diagram for a water splitting cell. Excited surface plasmons by interband transition make this mechanism possible to be explained. This mechanism can similarly describe what occurs in a dye-sensitization process in which dye molecules absorb light energy and inject generated electrons to the conduction band of semiconductor. Like the dye-sensitization process, plasmonic metal absorb resonant photons and electrons near the Fermi level of a metal, E_f are

excited to SP (surface plasmon) states. Electrons in SP states are subsequently transferred to allowed states within the semiconductor CB (conduction band). Injected electrons travel distance approximately equal to thecarrier diffusion length until they react with a chemical species near semiconductor surface. This mechanism is dominant in the structure composed of a plasmonic metal with a low SPR energy and a semiconductor when they are directly in contact. The structure of a semiconductor covered with plasmonic metal nanoparticles is one such example [13].

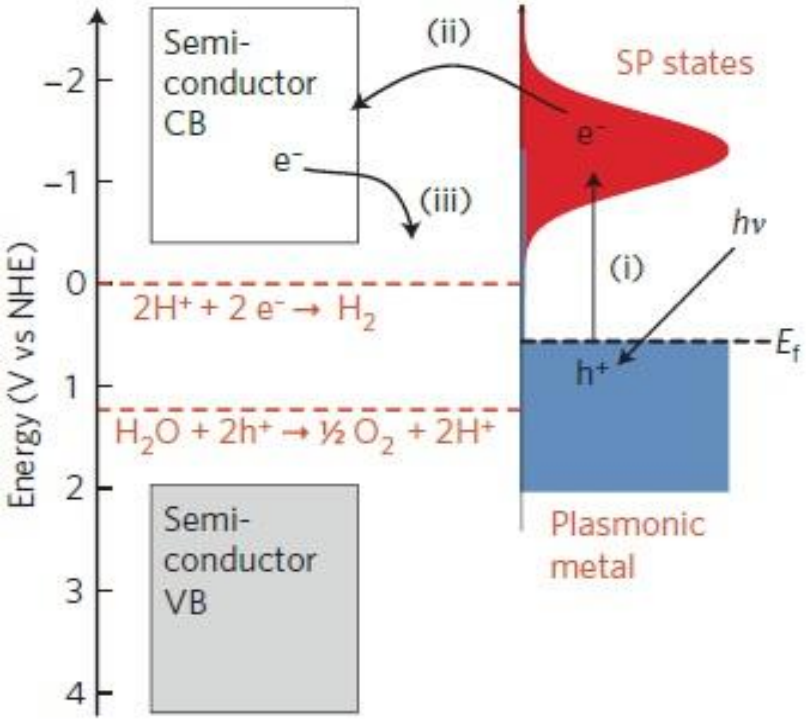

Figure 4-4. Energy diagram for SPR-mediated charge injection mechanism at semiconductor/plasmonic metal interface for water splitting cells (i) excitation of electron near metal Fermi level, E_f to SP (surface plasmon) states (ii) electron injection to semiconductor CB (conduction band) at semiconductor/plasmonic metal interface (iii) electron reaction with neighboring hydrogen ions for hydrogen evolution half reaction (Ref. [13]).

The second and third mechanisms are near-field electromagnetic and scattering mechanism. Anestablished intense and spatially non-homogeneous field by SPR- for instance, as shown in Figure 4-3 (a), not only at the surface but also near surface of a plasmonic metal. When semiconductors are in close proximity to the plasmonic metal, the semiconductors encounter the intense electric field even if two materials are separated by thin non-conductive spacer. This contact within the range of intense field leads the increase in the rate of electron-hole pair formation and probability of photoreaction. In addition to this, scattering also can occur in the presence of plasmonic nanostructured metal. Increased path length by scattering when passing through a plasmonic metal and semiconductor materials provides more passes for photon and increased electron-hole pairs in semiconductor [13].

4.1.4 Photocatalysis on Nanostructured Plasmonic Metal

Unstructured metals have been considered as poor photocataytic materials due to their poor charge-carrier formation and short lifetime in spite of inherent chemical activity and selectivity on chemical transformation [14, 15]. However, plasmonic metal nanostructures exhibit superior photocatalytic activity when interacting with resonant photons [11, 12, 16]. When the plasmonic metals encounter adsorbed gas species, they can transfer energy to the species directly just as in SPR-mediated charge injection mechanism of Chapter 4.1.3. This energy transfer model between plasmonic metals and nearby chemical gas species is described with energetic electron transfer from SP states to unpopulated adsorbate states. The negative ion which resulted from rapid reaction between the metal surface and the gas species is generally referred to as TNI (transient negative ion) [13, 35-37]. Figure 4-5 explains on this energy transfer mechanism. Adsorbates on the plasmonic metal are on their ground state initially (Figure 4-5 (a)). Electrons

scattered by light energy, hν, transfer energy to absorbates on the surface and produce TNI (δ^-). Adsorbates travel on TNI potential state for lifetime, τ as shown in Figure 4-5 (b). The absorbates return to their ground state once the electrons decay back from TNI to the metal Fermi level. If the transferred energy overcomes the activation barrier for dissociation, E_a, the reaction with the adsorbate will occur (Figure 4-5 (c)).

This mechanism has several features. It is reported that the probability of transformation driven by SPR-induced electron on plasmonic metal is affected by (1) availability of low-lying molecular orbitals on the absorbate, (2) the potential energy landscape for the charged and neutral adsorbates, (3) the lifetime of the charged adsorbate state (4) the surface-plasmon intensity and (5) temperature of the plasmonic nanostructures [13]. Another feature is that the plasmonic nanostructures can couple multiple stimuli efficiently. For example, the plasmonic nanostructures can couple the effect of the incoming photo flux and the thermal heating effect. General tendency in this case is that most reactions on a semiconductor are inversely proportional to temperature due to the negative relationship between temperature and the lifetime of excited charge carrier. However, plasmonic nanostructure leads higher photocatalytic reaction rates depending on temperature [13].

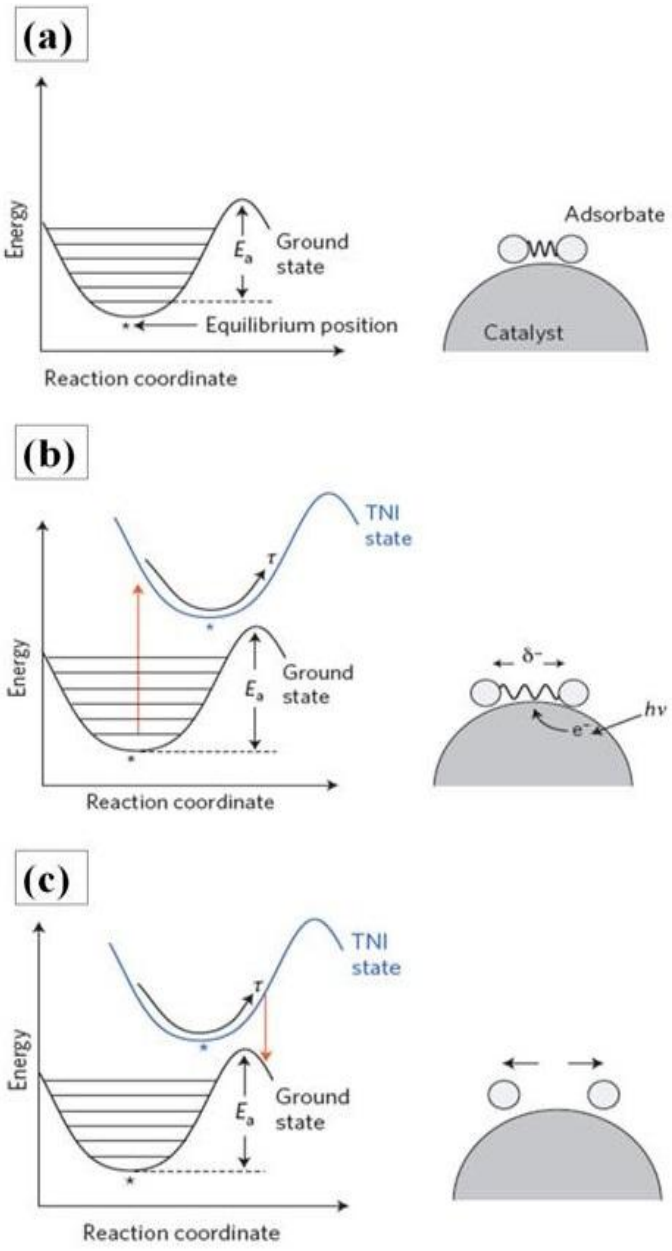

Figure 4-5. Mechanism for SPR-induced electron-driven oxygen dissociation on a photo-excited plasmonic metal proposed by S. Linic et al. (a) initial state (b) formation of TNI (δ^-) and travel on TNI potential surface during the life time, τ (c) Relaxation of TNI with larger energy than activation energy, E_a (Ref. [13]).

4.2 Motivation of Research

Photocatalysts that convert carbon dioxide into useful fuel have intrigued researchers because they simultaneously aid in the consumption of carbon dioxide and in the production of alternate energy sources. Also, unlike thermochemically [1] or electrochemically [2, 3] activated catalysis, photocatalysis is activated in a sustainable manner by solar energy without the need to apply any additional energy source.

In 1979, Inoue et al. reported the photocatalytic conversion of CO_2 into organic compounds, using various semiconductor powders such as TiO_2, WO_3, ZnO and CdS in aqueous solution [4]. Other research on liquid-based CO_2 conversion has been reported since this work [7, 17, 18]. However, for practical applications, gas-phase CO_2 conversion is more desirable, and direct CO_2 conversion to useful hydrocarbon fuels has also been demonstrated [6, 19, 20].

TiO_2 is considered to be one of the most appropriate materials for catalyzing CO_2 conversion to fuels due to its stability against corrosive reactants and its excellent oxidation properties. However, photocatalytic reactions mediated by TiO_2 alone are limited, due to its wide bandgap of 3.2 eV. The electrons that are excited and thus available for chemical reactions are only those that come from ultraviolet light. As a result, TiO_2 itself does not contribute much to the photocatalytic production of hydrocarbon fuel.

Strategies for enhancing the photocatalytic conversion of CO_2 to hydrocarbon fuels include the design of nanostructured catalysts and the decoration of TiO_2 with metal cocatalysts. Adopting TiO_2 nanotube or nanoload structures have been reported as one of favourable way for achieving more efficient chemical formation with CO_2 and H_2O gas species [6, 19, 20]. However, these studies have focused on nanostructuring of the TiO_2 catalysts to maximize surface areas. Since metal cocatalysts play an essential role in adsorbing chemical species and accelerating

chemical reactions, the metal cocatalysts themselves can also be engineered to achieve an increased conversion rate.

In addition, it is well known that metal nanoparticles, including Au, Ag, and Cu that is used as a CO_2 reduction cocatalyst, exhibit a plasmonic effect with response to the resonant frequency of photons. This plasmonic effect can act as an accelerator for photocatalytic reactions by enabling energy to be concentrated on or near the surface through the reaction between scattered electrons and adsorbates [11-13, 21-23].

To date, metal cocatalysts for CO_2 conversion have been prepared by sputtering [6], wet impregnation methods [7, 8, 18, 23] or electrochemical deposition [20] onto other catalysts. Cu nanostructures have been fabricated by reduction within aqueous solution with heat [24, 25], potentiostatic electrochemical deposition [26] and chemical vapor deposition [27]. Ideally, nanostructures grown on top of TiO_2 films and vertical nanostructures are desired in order to prevent the blocking of gas species during a reaction. Cu is promising because Cu exhibits not only excellent catalytic reactivity but also a plasmonic effect within the visible range ($\lambda_{max} \approx 600$ nm) for appropriately sized particles [13, 21, 23]. In addition, Cu has an advantage in cost over Au, Ag and Pt. Constructing a Cu nanostructure on the surface of TiO_2 is one way of utilizing and magnifying these advantages.

One method to obtain vertically aligned nanostructures of TiO_2 is to "sculpt" films using oblique angle evaporation. Sculptured thin films (STFs) are typically fabricated by obliquely directed physical vapor deposition via self-shadowing. STFs show porous or columnar morphologies, depending on the angle of vapor flux. Due to their high surface area and tailorable optical properties, STFs have been proposed and used in a variety of optical and biological applications [28-31].

In following sections, we demonstrate the fabrication of a nanostructured copper thin film sculptured using an obliquely evaporated vapor flux directly on top of a TiO_2 film, along with its

use as a cocatalyst for CO_2 conversion to methane. The performance of the TiO_2/Cu STF system was evaluated in terms of its methane production rate. The observation of a plasmonic effect with the Cu STFs is seen in the absorption spectra of the sample and a resulting enhancement in methane production rate is concomitantly observed. A threshold for this Cu plasmonic effect is found to be a function of the length of the Cu columnar structure.

4.3 Experimental Section

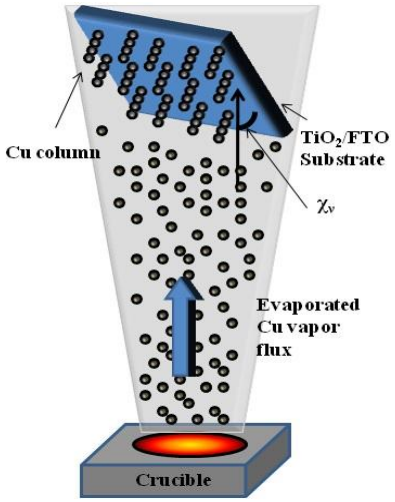

Figure 4-6. Schematic of sculptured copper thin films fabrication by electron beam evaporation.

TiO_2 films were prepared from a commercial TiO_2 paste (Dyesol, DSL 18NR-T, mean size: 20 nm) by doctor blading the TiO_2 paste to form a film with a thickness of approx. 11 μm. This technique has been described in Chapter 3.4.2 The TiO_2 samples were then annealed at 500 ℃ for 30 min with a 2.5 ℃/min ramping rate. This yielded 2×2 cm^2 samples of anatase TiO_2.

Copper STFs were grown directly on top of the TiO_2 films (referred to as "TiO_2/Cu STFs") by using electron beam evaporation. The deposition was implemented with an incident vapor flux angle, χ_v, of 5° by using a substrate holder installed obliquely as shown in Figure 4-6. The chamber was evacuated to a base pressure of 2×10^{-6} Torr before deposition. Then, Cu STFs were grown at room temperature at a rate between 2.53 and 3.52 Å/s to yield columnar structure lengths between 61 and 331 nm.

The physical shape and length of Cu STFs was characterized by field emission scanning electron microscopy (FESEM), and the materials deposited on the substrate were identified using powder X-ray diffraction (XRD) with Cu Kα radiation (1.5406 Å). The optical properties of the prepared samples were investigated with UV-visible absorption spectroscopy in the range of 300~850 nm.

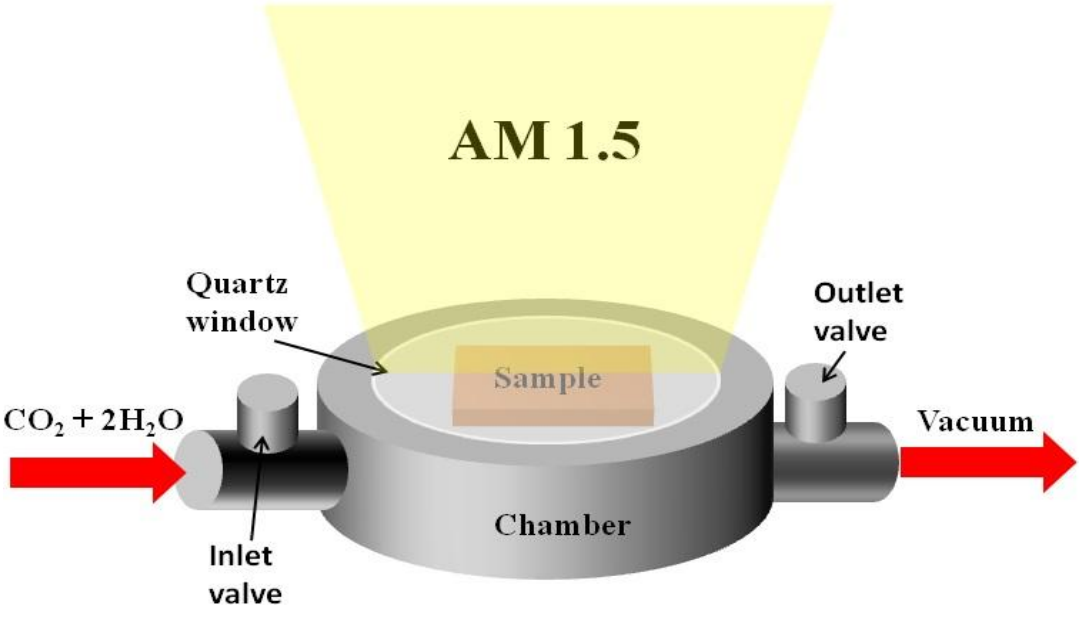

Figure 4-7. Schematic of CO_2 conversion rate measurement unit.

In order to measure the conversion rate of CO_2 to methane, a 2×2 cm^2 sample was loaded into the Teflon reaction chamber for each measurement. The chamber was evacuated to ~

40 mTorr in order to remove air. High purity (99.99%) gas phase CO_2 and water were introduced into the reaction chamber via a deionized water bubbler at a total flow rate of 3.18 mL/min. The introduction and evacuation process for CO_2 gas with H_2O was repeated five times. The relative humidity was measured to be ~ 80%. After the reaction chamber was again filled with the CO_2/H_2O mixture, it was illuminated under AM 1.5 illumination (100 mW/cm^2) for one hour. Quantitative detection of reactants and products was performed using a Shimadzu GC-2014 gas chromatograph (Restek Rt-QBond column, ID=0.53 mm, length=30 m) equipped with flame ionization (FID) and thermal conductivity detectors (TCD). Details of the reactor setup are described in Ref. [32] and shown in Figure 4-7.

4.4 Results & Discussion

Cu STFs were deposited at a 5° incident vapor flux angle directly onto the top of TiO_2 film. Six different TiO_2/Cu STF samples were evaluated for photocatalysis; 5 had a different deposition time for the Cu STFs (to produce samples with different Cu column lengths), and one was a TiO_2 film without a Cu STFs. As shown in the SEM image in Figure 4-8 (a), the TiO_2 films exhibit a porous and sponge-like structure, which consists of interconnected TiO_2 nanoparticles. Due to the oblique incident vapor flux, all of the Cu STFs grown on top of the TiO_2 are porous, slanted and have a columnar structure with a round top, as shown in Figure 4-8. This round columnar structure likely resulted from adatom diffusion during STF deposition. In general, lower melting point materials have higher adatom mobilities and thus longer adatom diffusion lengths, and vice versa [28]. When heated as the incident vapor flux arrives at the substrate, adatoms on the copper surface can diffuse further because copper has a relatively low melting point (1084 °C)

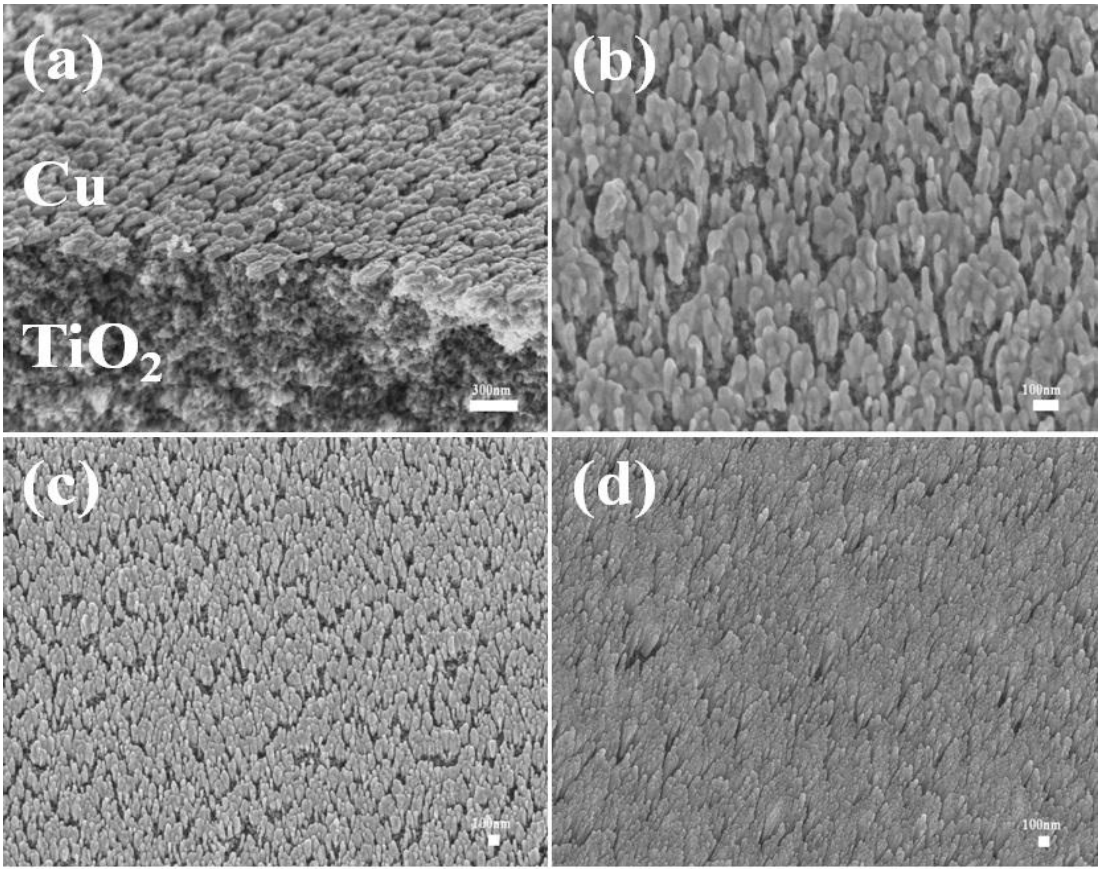

Figure 4-8. (a-c) SEM images showing the surface morphologies of TiO_2/Cu STFs with 160 nm Cu columns: (a) 45° cross sectional view, (b) top view at higher magnification, and (c) top view at lower magnification. (d) SEM image of TiO_2/Cu STF with 331 nm Cu columns. All Cu STFs were fabricated directly on top of a TiO_2 film by electron beam evaporator with 5° of incident vapor flux.

When compared to many other metal or oxide materials. For this reason, Cu STFs are sculpted into more round and smooth shapes in comparison with higher melting point materials such as Pt (1768 °C) and TiO_2 (1843 °C) due to their slower adatom diffusion rates. This can be seen in Figure 4-9 and in previous studies [30, 31].

The deposition parameters and corresponding Cu column lengths for all of the samples are listed in Table 4-1. The Cu column length of Sample II was estimated using the fitted curve in Figure 4-10, a plot of Cu column length vs. deposition time, since its small size made it difficult

to measure directly in the SEM. The Cu STFs grow as a non-linear function of deposition time. The growth rate of Cu STFs increases as deposition time increases up to 455 s but decreases with further deposition. We postulate that as the deposition time increases, the substrate is exposed to heated energetic particles during deposition and this leads to longer adatom diffusion on the Cu surface. This increased adatom diffusion can cause lateral growth of STF columns and a corresponding decreased vertical growth [28, 33]. This also creates more dense films as shown in Figure 4-8 (c) and (d).

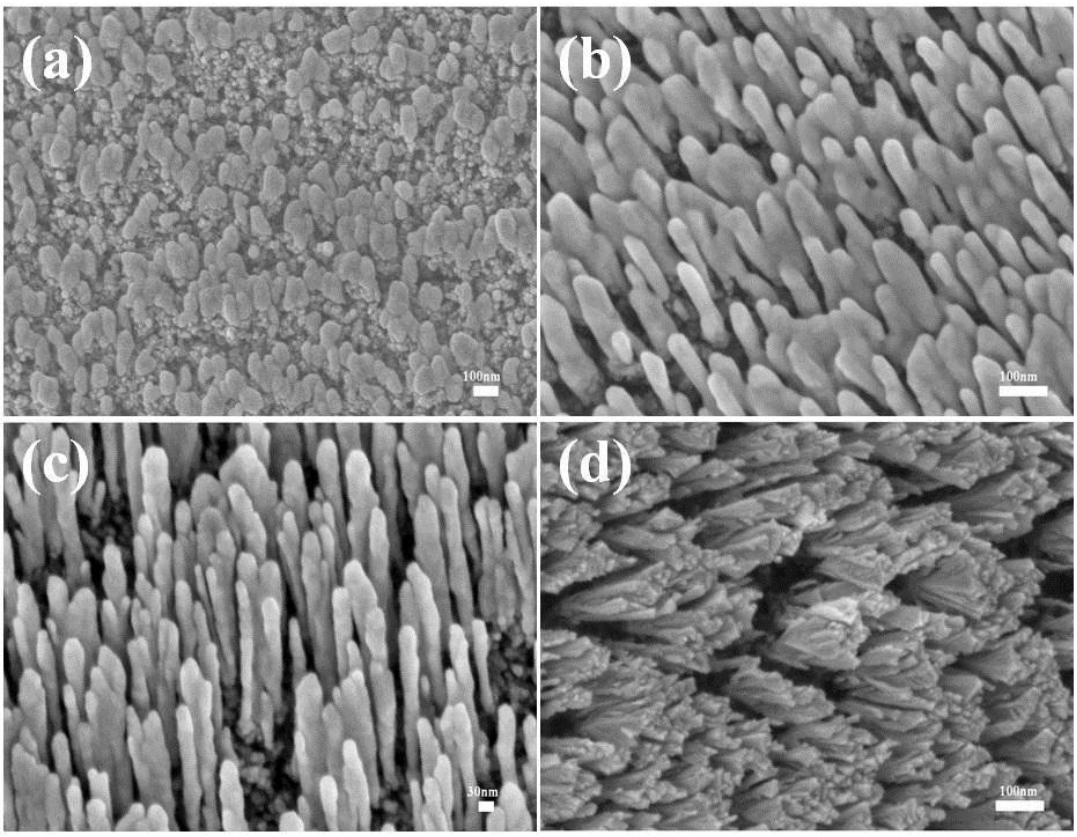

Figure 4-9. Surface morphology of TiO_2/Cu STFs with (a) 129 nm, (b) 206 nm and (c) 331 nm Cu columns and (d) Pt STFs for comparison. All STFs were sculptured with 5° angle of vapor flux by electron beam evaporator.

Sample Name	Deposition time [s]	Length of Cu column [nm]	Deposition rate [Å/s]
I	0	0	-
II	242	~61	2.5
III	393	129	3.3
IV	455	160	3.5
V	606	206	3.4
VI	1212	331	2.7

Table 4-1. Deposition parameters and corresponding lengths of Cu columns for Cu STFs on porous TiO_2 films. The length of the Cu column in Sample II was estimated using the fitted curve in Figure 4-10.

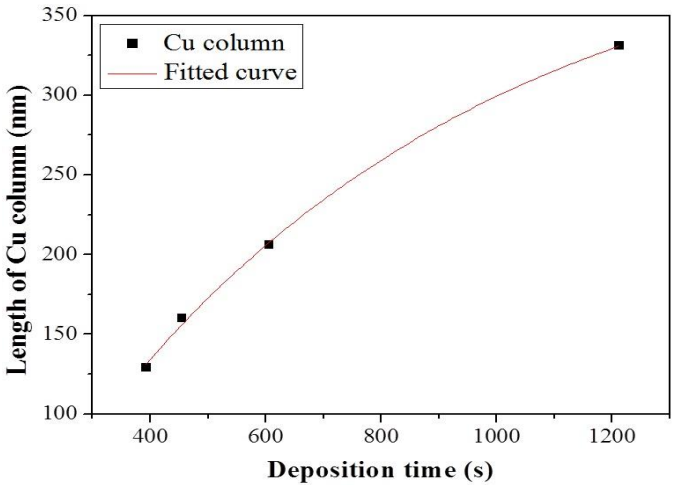

Figure 4-10. Correlation of the Cu column length with deposition time. A fitted curve is shown in the Figure. Fitted curve is expressed as Y= 418.349 - 507.335·exp(-0.00145x) where Y is length of Cu column and x is deposition time based on measured length.

Powder XRD patterns (Figure 4-11) for all of the prepared samples show evidence for nanocrystalline anatase-type TiO_2, with strong diffraction observed from the (004), (200), (105), (204), (220) and (215) planes. The (101) reflection is more intense than expected, suggesting that preferred orientation of the TiO_2 crystallites occurs in the anatase TiO_2 films, which have an average thickness of 10.75 ± 0.46 μm. The (111) reflection of Cu from samples II and III was not detectable by XRD due to the small amount of Cu in the samples. All other TiO_2/Cu STF samples show the (111) reflection of Cu. Although the existence of a thin oxidized layer on the surface of the Cu STFs is probable since the Cu STFs are exposed to H_2O and O_2 during the reaction [21], a crystalline CuO layer was not observed by XRD.

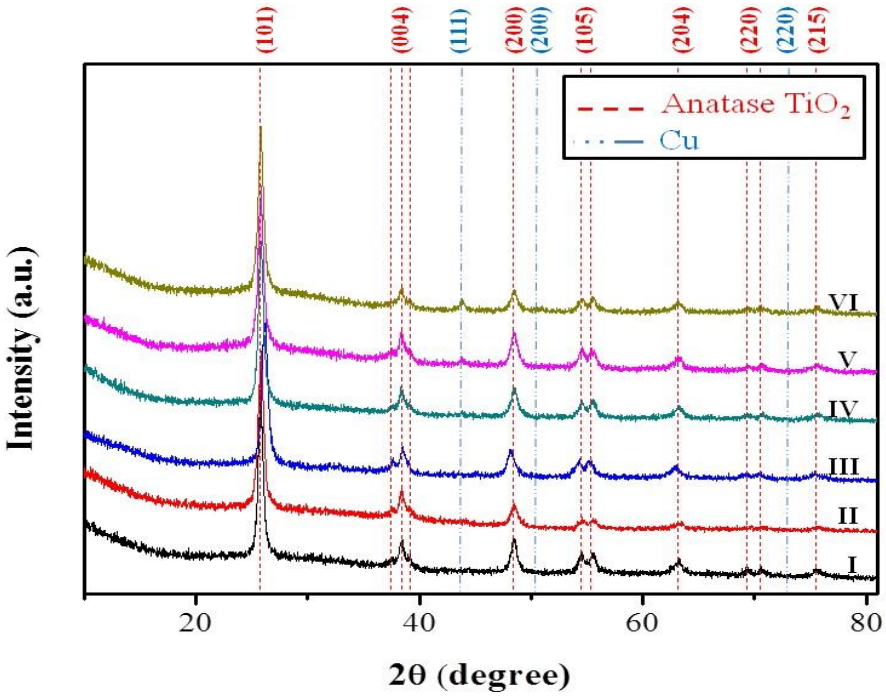

Figure 4-11. X-ray diffraction patterns of TiO_2/Cu STFs. Pattern labels correspond to the samples listed in Table 1.

Figure 4-12 presents the methane production rates measured for the six photocatalytic films. Without illumination, a baseline methane production rate of 1.14 ppm·cm^{-2}·h^{-1} was observed, which is believe to be due to unintentional exposure to light during injection of the CO_2. However, no measurable methane production was detected in the experiment when only argon (without CO_2 and H_2O) was introduced under AM 1.5 illumination. The sample with smallest Cu STF cocatalysts, with a column length of ~61 nm, shows a 2-4 fold increase in methane production rate relative to the sample without copper. Surprisingly, no further improvement of methane production rate was observed for the 129-nm-long Cu columns in sample III. However, a significant and reproducible increase to 124.3 ppm·cm^{-2}·h^{-1} was observed for the 160-nm Cu columns in sample IV. This represents a 160-fold increase in the methane production rate relative to the TiO_2 sample without Cu STF cocatalysts (sample I), and is higher than reported previously for other 1D TiO_2 nanostructures [6, 19, 20]. With a further increase in the length of Cu columns, the methane production rate is observed to decrease. We hypothesize that the number of accessible reaction sites may be decreased in the more dense STFs, which is consistent with the morphology shown in Figure 4-8 and Figure 4-9. Regardless, the samples still have good photocataytic performance, converting CO_2 into methane at a rate of more than 39.4 ppm·cm^{-2}·h^{-1}. Collectively, these methane production rates suggest the existence of a threshold Cu column length of between 129 and 206 nm for the highest methane production rates. During front side illumination experiments, where the illumination is directed onto Cu STFs, a similar trend is observed, with a maximum in methane production rate occurring for the 160-nm Cu STFs.

Two possible scenarios can help to explain this large enhancement in methane production rate: a threshold in reflection and/or a plasmonic effect. Since Cu itself is a reflective material, Cu can reflect light penetrating through the TiO_2 film. An elongated path length of light in the TiO_2 induced by reflection may be able to contribute more electron-hole pairs within TiO_2. However, TiO_2 can absorb photon energy only within the range of <400 nm due to its wide bandgap of 3.2

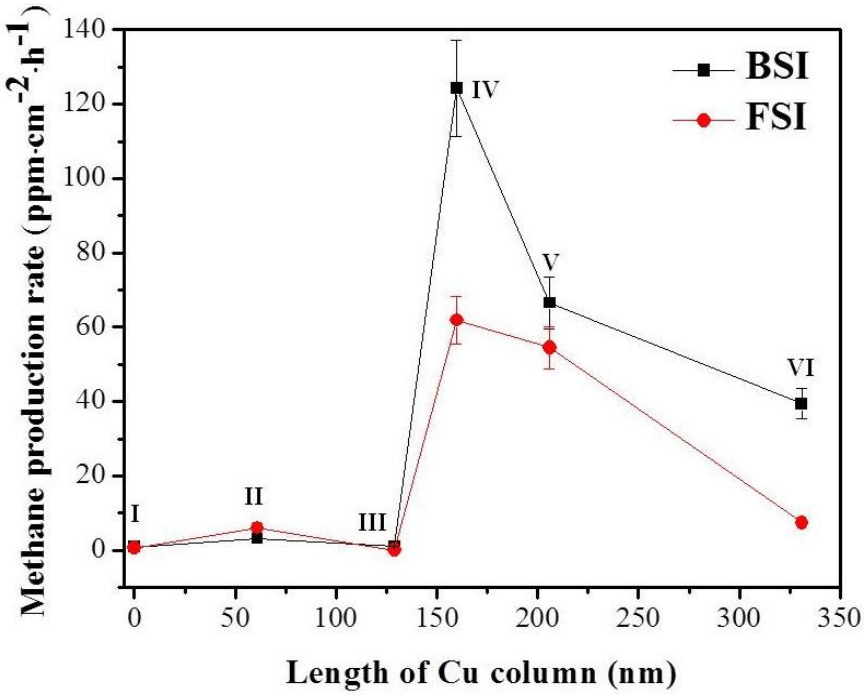

Figure 4-12. Methane production rate vs. length of Cu columns for TiO2/Cu STFs. All measurements were carried out under AM 1.5 illumination (100 mW/cm^2) for 1 hour. Illumination was directed at the glass substrate for back side illumination (BSI) and at Cu STF for front side illumination (FSI).

eV, and most of the light energy within this range is absorbed by the TiO_2 because its thickness is more than 10 μm. Hence, we suspect that only a small fraction of reflected light energy may participate in electron-hole pair generation in TiO_2 and contribute to the observed methane production rates.

The other possible scenario is a plasmonic effect due to the Cu STFs. Plasmonic effects, which are well known for Cu nanostructures [13, 20, 21, 23], can produce energetic electrons on the surface of a catalyst through surface plasmon resonance, and these electrons can then transfer their energy to that needed for dissociation of gas species that are attached to the surface. If the transferred energy is sufficient to overcome the activation barrier for dissociation, dissociation will occur and dissociated species can be involved in CO_2 conversion [13]. Figure 4-13 shows the

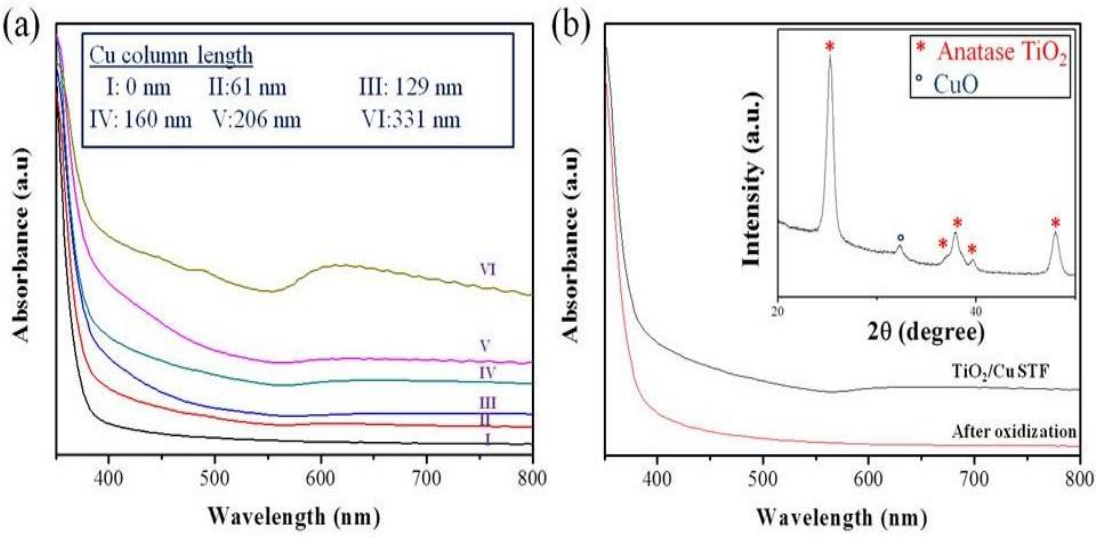

Figure 4-13. UV-visible absorption spectra of (a) TiO_2/Cu STFs and (b) TiO_2/Cu STFs with 160 nm Cu columns before (black) and after (red) oxidation. Inset: powder XRD pattern after oxidization of TiO_2/Cu STF sample with 160 nm Cu columns.

UV-Visible absorption spectra for all TiO_2 and TiO_2/Cu STF samples. All the samples exhibit significant absorption in the ultraviolet region, which results from interband transitions of TiO_2. All TiO_2/Cu STF samples also show noticeable absorption beginning at around ~600 nm due to the presence of the Cu STFs. However, this absorption starts to become more significant beginning with the 160-nm Cu columnar structures (Sample III), and the absorption peak becomes more pronounced as the length of Cu column increases. This absorption peak at ~600 nm has been previously reported to correspond to a Cu plasmonic effect [13, 20, 21, 23]. A control sample consisting of a TiO_2 film containing a 60-nm planar Cu sample without nanostructuring does not show a significant absorption peak at ~600 nm (Figure 4-14), suggesting that the columnar nanostructuring plays a key role in the observed plasmonic effect. The Cu plasmonic effect is most noticeable in sample VI (160 nm Cu columns) with regard to the abrupt enhancement in methane production rate. Therefore, we hypothesize that the large enhancement in methane production rate originates, at least in part, from the plasmonic effect caused by the Cu

STF nanostructure. We speculate that the high surface area Cu STFs, coupled with the plasmonic enhancement, help to facilitate one or more of the chemical reactions necessary for CO_2 conversion into methane.

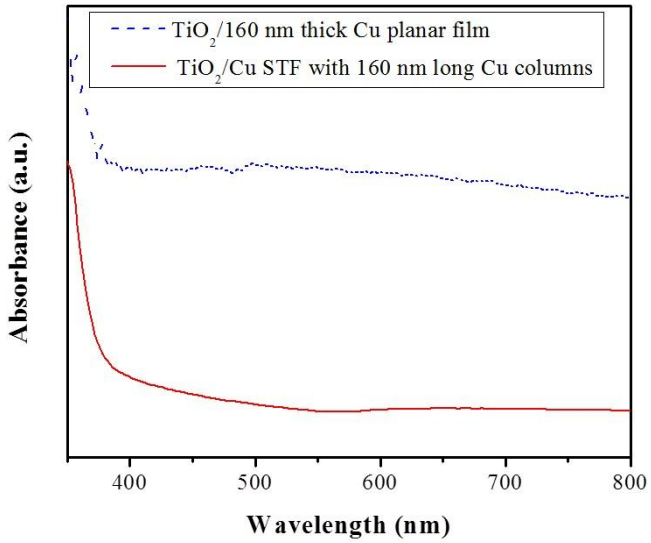

Figure 4-14. UV-visible absorbance spectra of TiO_2 film with planar Cu film (top) and TiO_2/Cu STF with 160 nm Cu columns.

One possible drawback to the use of Cu cocatalysts is that partial oxidation of Cu is inevitable under the reaction conditions. The oxidation of Cu nanoparticles is well known, but it has been reported that if the diameter of the Cu core is greater than 2 nm, the plasmonic effect will still be observed [21, 23]. In the case of our Cu STF samples, the column diameters are all greater than 30 nm. We evaluated sample IV after the Cu STFs were completely oxidized to CuO under ambient air and found that the methane production rate decreased concomitantly with loss of the plasmonic effect from sample IV as shown in Figure 4-13(b). The methane production rate decreased to 0.15 $ppm \cdot cm^{-2} \cdot h^{-1}$ (below the baseline production rate), although production rates of other hydrocarbons increased. For example, in the case of propane, the production rate was measured as 4.37 $ppm \cdot cm^{-2} \cdot h^{-1}$ after complete oxidation of the Cu STFs, while propane was not

detected at all with sample IV before it was oxidized. We speculate that this is due to a difference in selectivity between Cu and CuO to absorbed gas species and to the differences in photocatalytic activity.

4.5 Summary

We have demonstrated that Cu STFs directly grown by e-beam evaporation at a 5° angle of incident vapor flux on top of a TiO_2 porous film are an excellent cocatalyst for photocatylitic CO_2 conversion to methane. Cu STFs have a porous slanted nanocolumnar structure with a high surface area. Examination of the absorbance spectra for Cu STFs of different lengths revealed an increase in absorption at ~600 nm for columns > 160 nm, which can be attributed to surface plasmon resonance. It is found that there is a large enhancement in methane production rate with the 160 nm long Cu columnar structure and that a threshold exists between Cu column lengths of 129 nm and 160 nm. The methane production rate reached a maximum of 124.3 $ppm \cdot cm^{-2} \cdot h^{-1}$, which is more than 160 times higher than the TiO_2 films that did not contain a Cu STF. This transition was largely attributed to a plasmonic effect by the Cu STFs, along with a possible small effect from reflection. TiO_2/Cu STFs with Cu columnar structure longer than 160 nm showed a decrease in methane production rate in spite of an intense plasmonic effect. We speculate that this is because Cu STFs become denser and have less active catalytic sites for thicker STF depositions, however even the denser films with less active areas show an excellent methane conversion rate of more than 39.4 $ppm \cdot cm^{-2} \cdot h^{-1}$. Overall, the use of Cu STFs on TiO_2 demonstrates an alternate route for fabricating highly efficient photocatalytic thin films for CO_2 conversion to methane.

4.6 Chapter 4 Reference

[1] R. L. Martin, Use of Solar Energy to Reduce Carbon Dioxide, *Solar Energy* Vol. 24 (**1980**) 271-277.

[2] M. Gattrell, N. Gupata, A. Co, Electrochemical reduction of CO_2 to hydrocarbons to store renewable electrical energy and upgrade biogas, *Energy Conversion and Management* Vol. 48 (**2007**) 1255-1265.

[3] S. Kaneco, N. Hiei, Y. Xing, H. Katsumata, H. Ohnishi, T. Suzuki, K. Ohta, Electrochemical conversion of carbon to methane in aqueous $NaHCO_3$ solution at less than 273 K, *Electrochimica Acta* Vol. 48 (**2002**) 51-55.

[4] T. Inoue, A. Fujishima, S. Konishi, K. Honda, Photoelectrocatalytic reduction of carbon dioxide in aqueous suspensions of semiconductor powders, *Nature* Vol. 277 (**1979**) 637-638.

[5] M. Halmann, Photoelectrochemical reduction of aqueous carbon dioxide on p-type gallium phosophide in liquid junction solar cells, *Nature* Vol. 275 (**1978**) 115-116.

[6] O. K. Varghese, M. Paulose, T. J. LaTempa, C. A. Grimes, High-rate Solar Photocatalytic Conversion of CO_2 and Water Vapor to Hydrocarbon Fuels, *Nano Letters* Vol.9 (**2009**) 731-737

[7] K. Adachi, K. Ohta, T. Mizuno, Photocatalytic Reduction of Carbon Dioxide to Hydrocarbon Using Copper-loaded Titnium Dioxide, *Solar Energy* Vol. 53 (**1994**) 187-190.

[8] Q. Zhang, W. Han, Y. Hong, J. Yu, Photocatalytic reduction of CO_2 with H_2O on Pt-loaded TiO_2 catalyst, *Catalyst Today* Vol. 148 (**2009**) 335-340.

[9] C. Belver, R. Bellod, S. J. Stewart, F. G. Requejo, M. Fernánandez-García, Nitrogen-containing TiO_2 photocatalysts part 2. photocatalytic behavior under sunlight excitation, *Applied Catalysis B: Environmental* 65 (**2006**) 309-314.

[10] S. C. Roy, O. K. Varghese, M. Paulose, C. A. Grimes, Toward solar fuels: photocatalytic conversion of carbon dioxide to hydrocarbons, *ACS Nano* Vol. 4 No. 3 (**2010**) 1259-1278.

[11] W. Hou, W. H. Hung, P. Pavaskar, A. Goeppert, M. Aykol, S. B. Cronin, Photocatalytic Conversion of CO_2 to Hydrocarbon Fuels via Plasmon-Enhanced Absorption and Metallic Interband Transistions, *ACS catalysis* Vol. 1 (**2011**) 929-936.

[12] E. Kowalska, O. O. P. Mahaney, R. Abe, B. Ohtani, Visible-light-induced photocatalysis through surface plasmon excitation of gold on titania surfaces, *Physical Chemistry Chemical Physics* Vol. 12 (**2010**) 2344-2355.

[13] S. Linic, P. Christopher, D. B. Ingram, Plasmonic-metal nanostructures for efficient conversion of solar to chemical energy, *Nature Materials* Vol. 10 Dec (**2011**) 911-921.

[14] K. Watanabe, D. Menzel, N. Nilius, H. Freund, Photocemistry on metal nanoparticles, *Chemical Reviews* Vol. 106 No. 10 (**2006**) 4301-4320.

[15] J. M. White, Using photons and electrons to drive surface chemical reactions, *Journal of Molecular Catalysis A: Chemical* Vol. 131 (**1998**) 71-90.

[16] P. Christopher, H. Xin, S. Linic, Visible-light-enhanced catalytic oxidation reactions on plasmonic silver nanostructures, *Nature Chemistry* Vol. 3 June (**2011**) 467-472.

[17] M. Halmann, M. Ulman, B. Aurian-Blajeni, Photochemical solar collector for the photoassisted reduction of aqueous carbon dioxide, *Solar Energy* Vol. 31 (**1983**) 429-431.

[18] M. Anpo, H. Yamashita, Y. Ichihashi, S. Ehara, Photocatalytic reduction of CO_2 with H_2O on various titanium oxide catalysts, *Journal of Electroanalytical Chemistry* Vol. 396 (**1995**) 21-26.

[19] X. Feng, J. D. Sloppy, T. J. LaTempa, M. Paulose, S. Komarneni, N. Bao, C. A. Grimes, Synthesis and deposition of ultrafine Pt nanoparticles within high aspect ratio TiO_2 nanotube arrays: application to the photocatalytic reduction of carbon dioxide, *Journal of Materials Chemistry* Vol. 21 (**2011**) 13429-13433.

[20] J. Y. Tan, Y. Fernàndez, D. Liu, M. Maroto-Valer, J. Bian, X. Zhang, Photoreduction of CO_2 using copper-decorated TiO_2 nanorod films with localized surface palsmon behavior, *Chemical Physics Letters* Vol. 531 (**2012**) 149-154.

[21] T. Ghodselahi, M. A. Vesaghi, A. Shafiekani, Study of surface Plasmon resonance of $Cu@Cu_2O$ core-shell nanoparticles by Mie theory, *Journal of Physics D: Applied Physics* Vol. 42 (**2009**) 1-6.

[22] D. B. Ingram, S. Linic, Water splitting on composite plasmonic-metal semiconductor photoelectrodes: evidence for selective Plasmon-induced formation of charge carrier near the semiconductor surface, *Journal of the American Chemical Society* Vol. 133 (**2011**) 5202-5205.

[23] Z. Li, J. Liu, D. Wang, Y. Gao, J. Shen, $Cu_2O/Cu/TiO_2$ nanotube ohmic heterojunction arryays with enhanced photocatalytic hydrogen production activity, *International Journal of Hydrogen Energy* Vol. 37 (**2012**) 6431-6437.

[24] Y. Cho, Y. Huh, Synthesis of ultralong copper nanowires by reduction of copper-amine complexes, *Materials Letters* Vol. 63 (**2009**) 227-229.

[25] A. R. Rathmell, S. M. Bergin, Y. Hua, Z. Li, B. J. Wiley, The growth mechanism of copper nanowires and their properties in flexible, transparent conducting films, *Advanced Materials* Vol. 22 (**2010**) 3558-3563.

[26] T. Gao, G. Meng, Y. Wang, S. Sun, L. Zhang, Electrochemical synthesis of copper nanowires, *Journal of Physics: Condensed Matter* Vol. 14 (**2002**)355-363.

[27] H. Choi, S. Park, Seedless growth of free-standing copper nanowires by chemical vapor deposition, *Journal of the American Chemical Society* Vol. 126 (**2004**) 6248-6249.

[28] K. Robbie, M. J. Brett, Sculptured thin films and glancing angle deposition: Growth mechanics and applications, *Journal of Vacuum Science &Technology A* Vol. 15 (**1997**) 1460-1465.

[29] H. Tan, O. K. Ezekoye, J. V. D.Schalie, M. W. Horn, A. Lakhtakia, J. Xu, W. Burgos, Biological reduction of nanoengineered iron(III) oxide sculptured thin films, *Environmental Science & Technology* Vol. 40 (**2006**) 5490-5495.

[30] S. M. Pursel, M. W. Horn, A. Lakhtakia, Tuning of sculptured-thin-film spectral-hole filters by postdeposition etching, *Optical Engineering* Vol. 46 (**2007**) 040507-1-040507-3.

[31] S. M. Pursel, M. W. Horn, Prospects for nanowire sculptured-thin-film devices, *Journal of Vacuum Science &Technology B* Vol. 25 (**2007**) 2611-2615.

[32] S. In, D. D. Vaughn II, R. E. Schaak, Hybrid CuO-$TiO_{2-x}N_x$ hollow nanocubes for photocatalytic conversion of CO_2 into methane under solar irradiation, *Angewante Chemie International Edition* Vol. 51 (**2012**) 3915-3918.

[33] N. S. Dellas, J. M. E. Harper, Effect of deposition angle on fiber axis tilt in sputtered aluminum nitride and pure metal films, *Thin Solid Films* Vol. 515 (**2006**) 1647-1650.

[34] O. K. Varghese, M. Paulose, C. A. Grimes, Long vertically aligned titania nanotubes on transparent conducting oxide for highly efficient solar cells, *Nature Nanotechnology* Vol. 4 September (**2009**) 592-597.

[35] D. N. Denzler, C. Frischkorn, C. Hess, M. Wolf, G. Ertl, Electronic excitation and dynamic promotion of a surface reaction, Physical Review Letters Vol. 91 No. 22 (**2003**) 226102-1-226102-4.

[36] T. Olsen, J. Gavnholt, J. Schiøz, Hot electron mediated desorption rates calculated from excited state potential energy surfaces, *Physical Review B* Vol. 79 (**2009**) 035403-1-035403-12.

[37] T. Olsen, J. Schiøz, Origin of power laws for reactions at metal surfaces mediated by hot electrons, *Physical Review Letters* Vol. 103 (**2009**) 238301-1-238301-4.

Chapter 5

Tin Sulfide Thin Film Deposited by Radio Frequency Magnetron Sputtering for Solar Cell Applications

Semiconductor materials incorporating IV-VI elements such as PbS, PbSe and SnS feature excellent optical properties, in particular for the IR region. The innate narrow band gap of IV-VI semiconductors facilitates their application to near infrared or infrared devices such as solar cells and infrared detectors [1-3]. Tin sulfide (SnS) is one of the semiconductor materials in IV-VI group and has been considered as a promising light absorber material for the photovoltaic industry. SnS also has the advantage of being nontoxic and earth-abundant. SnS exhibits a remarkable absorption coefficient of 10^4 cm^{-1} at its fundamental absorption edge [4]. SnS can have both indirect and direct bandgap types and the electrical, optical and material properties of SnS can be engineered depending on annealing temperature or Sn/S ratio [5-8].

Chapter 5.1 provides a literature review on the fundamental properties of SnS materials and thin films and reviews solar cells that have been demonstrated by other groups. Motivation for the research of SnS thin films will be explained in Chapter 5.2. Experimental setup and technique will be described in Chapter 5.3. Chapter 5.4 will discuss the results on deposition of SnS thin films. A summary for this chapter will be given in 5.5

5.1 Literature Review on SnS Thin Film and Solar Cell Application

5.1.1 SnS Thin Film Fabrication and its Properties

SnS films have diversity in their fabrication method. Physical or chemical methods have been reported for SnS thin film deposition. For example, thermal evaporation [4, 6, 8], electron

beam evaporation [9], radio frequency sputtering [10], spray pyrolysis [11], atomic layer deposition [12], chemical vapor deposition [13] and chemical bath deposition [14] have been conventionally used for the thin film preparation.

As of now, thermal evaporation has been the most reported method for preparation of SnS thin films. Thermally evaporated SnS thin films have been investigated by many researchers. The pioneer study on thermally evaporated SnS thin films for solar cells was published by Noguchi et al. in 1994 [4]. They reported that their SnS thin films had an energy gap, E_g of 1.48 eV, mobility of 400-500 $cm^2/V \cdot s$ and resistivity of 13-20 $\Omega \cdot cm$. A 10^4 cm^{-1} of absorption coefficient at the fundamental absorption edge was also reported. Devika et al. [15] evaluated 50 nm thin films prepared by thermal evaporation deposited at 150°C. After annealing, the films had an E_g of 1.98 eV, mobility of 41 $cm^2/V \cdot s$ and carrier concentration of 4.2 $x10^{15}$ cm^2 and had a <111> orthorhombic structure. Ghosh et al. [16] reported on evaporated SnS and post deposition annealing in an argon ambient. Top-down scanning electron microscopy (SEM) images show significant microstructure for all samples. They reported a direct bandgap that ranged from 1.33-1.53 eV, a resistivity from 80-120 ohm·cm and mobility between 0.8 and 28.6 cm^2/Vs. Guo et al. [17] studied the influence of substrate temperature on vacuum evaporated SnS. They succeeded in the deposition of a stoichiometric SnS film and reported an E_g of 1.402 eV for a film grown at 150°C. They measured a ratio of dark-to-photoconductivity of 8. Zhang and Cheng incorporated Cu into SnS films for doping up to 23 atom% by a two step evaporation process (SnS then Cu) then annealed [18]. They reported a decrease in the direct E_g with the doping (1.54 eV → 1.17 eV) and a large increase in carrier concentration (1.53×10^{15} cm^{-3} → 8.57×10^{19} cm^{-3}) with a corresponding decrease in mobility (802 $cm^2/V \cdot s$ → 0.312 $cm^2/V \cdot s$). Bashkirov et al. [19] deposited SnS by hot wall deposition, which is another evaporation technique. They reported direct E_g that ranged from 1.07 eV to 1.27 eV depending on film thickness for samples made at 210 °C and 300 °C, respectively.

Reference	SnS growth method	Direct E_g (eV)	Carrier mobility ($cm^2/V \cdot s$)	Carrier concentration (cm^{-3})	Resistivity ($\Omega \cdot cm$)
[4]	Thermal evaporation	1.48	400-500	6.3×10^{14}-1.2×10^{15}	13-20
[15]	Thermal evaporation	1.98	41	4.2×10^{15}	36-128
[16]	Thermal evaporation	1.33-1.53	0.8-31.6	10^{15}-10^{16}	80-120
[17]	Thermal evaporation	1.402	-	-	100
[18]	Thermal evaporation	1.54	1.53×10^{15}	802	899
[19]	Hot wall deposition	1.07-1.27	-	-	-
[11]	Spray pyrolysis	1.32	128	1.65×10^{15}	30
[14]	Chemical bath deposition	1.38	-	-	-
[12]	Atomic layer deposition	1.87	-	-	-
[10]	RF sputter	1.08-1.18			1100-97000
[20, 21]	RF sputter	1.1-1.8	-	-	0.1-147

Table 5-1. SnS thin film properties deposited by various methods. All the values listed here are the numbers at room temperature without any doping.

A variety of other techniques have also been reported. Reddy et al. [11] reported on SnS thin films prepared by spray pyrolysis. These films exhibited orthorhombic structure and showed an average electrical resistivity of 30 ohm·cm, Hall mobility of 128 $cm^2/V{\cdot}s$ and carrier density of 1.6 x 10^{15} cm^{-3}. These films had an optical band gap of 1.32 eV with an absorption coefficient greater than 10^4 cm^{-1}. A. Tanuševski [14] prepared SnS thin films from a chemical bath deposition. The resulting films had a 1.38 eV direct optical band gap and 0.96 eV indirect band gap. With thermal treatment, the indirect band gap increased, but the direct band gap remained unaffected. J. Y. Kim and others [12] implemented SnS film growth by atomic layer deposition through sequential exposures of tin(II) 2,4-pentanedionate ($Sn(acac)_2$) and hydrogen sulfide (H_2S). Sn/S ratio was unchanged (~1.0) and they reported a bandgap of ~1.87 eV.

Sputtering has been also used for deposition of SnS films. Hartman et al. [10] reported on RF sputtered SnS thin films with an indirect band gap of 1.08-1.18 eV and resistivity was ranged from 1100 to 97,000 ohm-cm. Structured SnS films with "rice shaped" grains were observed in SEM images as shown in Figure 5-1. Stadler et al. [20, 21] is the only group to publish multiple papers on sputtered SnS thin films. This group used a 2-inch sputter gun and has evaluated throw

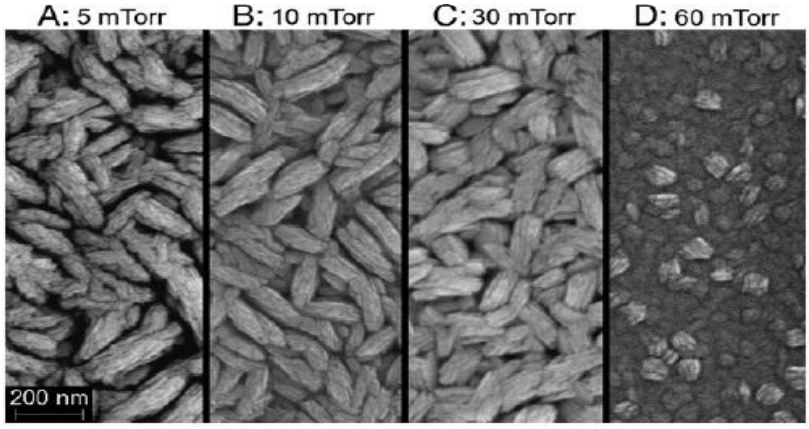

Figure 5-1. Surface morphology of sputtered thin films depending on the deposition pressure by Hartman et al. [10].

distance (2.5-6 inches), pressure, power, substrate temperature and frequency (dc to pulsed-dc to RF). They have characterized the films using UV-Vis NIR and 4-point probe for electrical conductivity. They reported an E_g of 1.1-1.8 eV and resistivities of 0.1-147 Ω·cm, as well as an absorption coefficient > 1 x 10^4 cm^{-1}. All the parameters of SnS thin film properties by various deposition tools are summarized in Table 5.1.

In order to modify the properties of SnS thin films further after deposition by various deposition techniques, annealing can be considered. Johnson et al. [6] reported that dark- and photo-conductivity of evaportated SnS thin films can be varied by post-deposition annealing for 10 min in air and argon, by using the heater installed inside of the chamber. Devika et al. [8] found out that the post-deposition annealing can allow the grain size and surface roughness to be varied, accompanying by possible re-evaporation of sulfur. The resistivity of the SnS thin films decreased from 37.4 to 9 Ω·cm as the annealing temperature decreased. In addition, a shift to the shorter wavelength of transmittance peak was observed with increasing temperature. Ogah et al. [23] also reported the effect of annealing for evaporated SnS thin films. They found out that, by annealing the SnS thin films, more oriented and crystalline films can be obtained. Moreover, annealing have an influence on the narrowed optical absorption edge and decreased the resistivity. Ramakrishna Reddy et al. [11] used the annealing technique in a sulfur atmosphere to improve physical properties for SnS thin films by chemical spray phyrolysis. They reported that the annealing in a sulfur atmosphere is effective in suppressing low intensity peak other than that of (111) peak and decreasing resistivity from 30 Ω·cm to 5 Ω·cm. In general, post-deposition annealing seemed to produce a favorable change in the deposited SnS films.

5.1.2 SnS Thin Films and Energy Band Diagram Models

A band diagram model for SnS films is invaluable in the design of solar cells, from metal contact formation to designing the junction formation between window layer and absorber layer. Since the reported properties of SnS are greatly varied depending on the deposition conditions, a study on the energy band diagram model of SnS films can become a stepping stone for fabrication of solar cells. Basically, SnS is known as a p-type semiconductor material established by Sn vacancy [33, 45]. The SnS energy diagram model for SnS thin films has been suggested by M. Devika and others [32] for their thermally evaporated samples and is shown in Figure 5-2 (a). The model was described with 4.2 eV of work function, Φ_s and 3.14 eV of electron affinity, χ_s. Another energy diagram model for the SnS prepared with chemical spray pyrolysis exhibits similar band gap of 1.33 eV but relatively higher electron affinity of 3.7 eV and work function of 4.92 eV as shown in Figure 5-2 (b). It was found that two donor defect levels, D_s^{2+}, D_s^{4+}, which result either from sulfur vacancies or existence of Sn^{2+} and Sn^{4+} ionized states of Sn, can exist

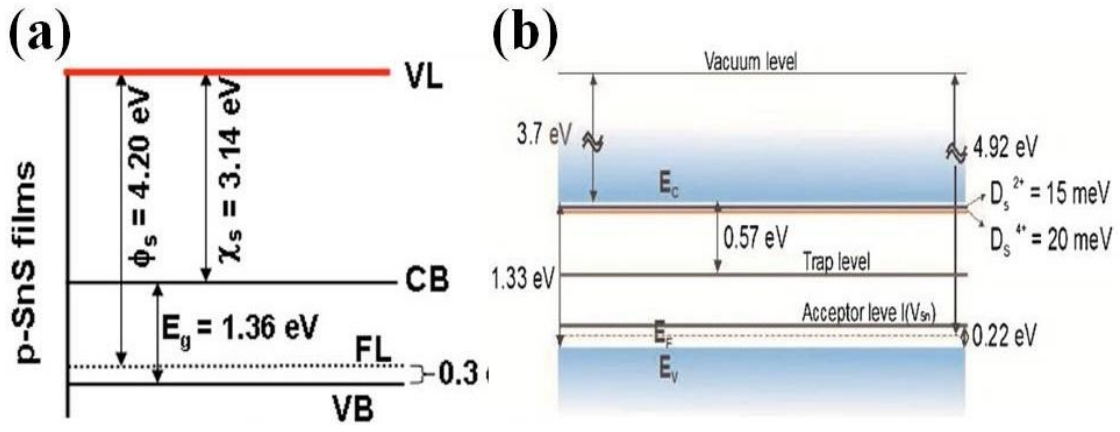

Figure 5-2. Suggested energy diagram model for SnS film by (a) M. Devika et al. from Ref. [32] where Φ_s is work function, χ_s is electron affinity, E_g is band gap, FL is Fermi level, VB is valance band, CB is conduction band VL is vacuum level (b) T. H. Sajeesh et al. from Ref. [33] where E_F is Fermi level, D_s^{2+} and D_s^{4+} are donor defect levels.

within its bandgap in Figure 5-2 (b) [33].

In addition, it is reported that trap levels can be formed within the band gap resulting from the presence of oxygen [33]. As shown in the examples of SnS energy band diagrams in Figure 5-2, unique band diagram is necessary for sputtered SnS thin films since the band diagram of SnS thin films is varied, depending on deposition condition or method.

5.1.3 CdS/SnS Heterojunction Solar Cells

For SnS solar cells, multiple types of structures have been studied. The main stream of SnS solar cells are heterojunction with n-type semiconductor materials such as CdS, Cd_2SnO_4 or CdO, making p-n junction [4, 22, 23]. Noguchi et al. [4] was one of the first to report a SnS/CdS heterojunction cell. The SnS was evaporated at 200-300 °C and had 1.48 eV of energy gap, E_g,

SnS growth Technique	CdS growth technique	V_{oc} (mV)	J_{sc} (mA/cm^2)	FF	η	Ref.
Spray pyrolysis	Vacuum evaporation	260	9.6	0.53	1.3	[11]
Electrochemical deposition	Photochemical deposition	170	3.3	0.37	0.20	[28]
Chemical bath deposition	Chemical bath deposition	340	6.0	--	--	[29]
Vacuum evaporation	Vacuum evaporation	120	7.0	0.35	0.3	[4]

Table 5-2. CdS/SnS thin film solar cells grown by various techniques. The parameters, V_{oc}, J_{sc}, FF and η stands for open circuit voltage, photocurrent density, fill factor and conversion efficiency, respectively.

0.29 % of conversion efficiency, η, 0.35 of fill factor, FF, 7 mA/cm^2 of photocurrent density, J_{sc} and 0.12 V of open circuit voltage, V_{oc}. The Ogah group [23] has reported on SnS/CdS heterojunction cells. Annealing at 400 ℃ for 30 min densified the film and reduced minority phases. They reported 7 mA/cm^2 of J_{sc}, 200 mV of V_{oc} and 0.3 of FF in separate devices. Table 5-2 below summarizes results for this type of heterojunction made by different techniques [23].

5.1.4 Other Strategies for Efficient SnS Solar Cells

Sugiyama et al. [24] reported on band offset for CdS/SnS solar cell with a Ga:ZnO/ZnO window layer on the CdS and the SnS grown on SnO_2 or ITO (indium tin oxide). Jiang et al. used this material to make a heterojunction with a-Si with a Mo contact to the SnS yielding a J_{sc} of 1.55 mA/cm^2 and a V_{oc} of 0.289 V [25]. The lone prior art for a SnS/ZnO heterojunction was from Ghosh and others. In their paper, they deposited a 0.3 μm ZnO by electodeposition onto ITO-coated glass and then thermally evaporated 1 μm thick SnS film. They showed good ohmic contacts using indium. They reported a V_{oc} of 0.12 V, a J_{sc} of ~39.91 uA/cm^2 and an efficiency of 0.003 %. Both the ZnO and the SnS are shown to have significant morphology on the order of 100 nm [26].

Electrochemical solar cells using SnS film as an absorber were demonstrated by Wang and others [31]. SnS films deposited by chemical bath deposition were fabricated with liquid electrolyte and Pt/FTO counter electrode. These solar cells showed a higher voltage of 0.471 V but lower current of 0.3 mA/cm^2, leading to 0.1 % of conversion efficiency.

Homojunction solar cells using SnS nanowire have also been demonstrated by using a doping technique. Yue et al. [27] prepared SnS crystalline nanowire for solar cells via Au catalyzed chemical vapor deposition process and boron and phosphorus doped to the SnS

nanowire to make a p-n junction. The solar energy conversion efficiency of 1.95 % was reported with higher short circuit current density of 7.64 mA/cm^2 and open circuit voltage of 650 mV.

Recently, efficient SnS solar cells have been demonstrated by Sinsermsuksakul et al. [32] via band-offset engineering. They fabricated SnS/ZnO heterojunction solar cells, inserting the layer composed of zinc oxysulfide buffer layer. The SnS film was deposited by pulsed chemical vapor deposition. A 25~30 nm thick zinc oxysulfide layer and 10-nm-thick zinc oxide layer were deposited by atomic layer deposition on top of the SnS film. A 2.04 % of NREL certified conversion efficiency was reported [32].

Junction Type	Window Layer	V_{oc} (mV)	J_{sc} (mA/cm^2)	FF	η	Ref.
Hetero	Zinc Oxide	0.12	0.03991	0.33	0.003	[26]
Hetero	Titanium Dioxide	471	0.3	0.71	0.1	[31]
Hetero	Amorphous Silicon	289	1.55	0.37	0.17	[25]
Homo	n-type Tin Monosulfide	650	7.64	0.39	1.95	[27]
Hetero	Zinc Oxide	244	19.42	0.4297	2.04	[32]

Table 5-3. SnS thin film solar cells incorporating various window layers.

5.1.5 SnS Thin Film Research at the Pennsylvania State University

Initial research on SnS solar cells at the Pennsylvania State Univerisity began with theoretical analysis that performed by AMPS-1D (Analysis of Microelectronic and Photonic

Structure-1D) which is devised by Dr. Fonash's group at the Pennsylvania State University [50]. As shown in Figure 5-3 (a) below, the suggested structure of SnS/ZnO thin film solar cells has a finger shape front contact with high work function metal such as Pt and a Mg/Mo metal contact used as a back contact. The extracted energy band diagram from AMPS-1D is shown in Figure 5-3 (b). The analysis on this structure suggests that the SnS/ZnO heterojunction solar cells are promising and expected light-to-electricity conversion efficiency is more than 20 % [46].

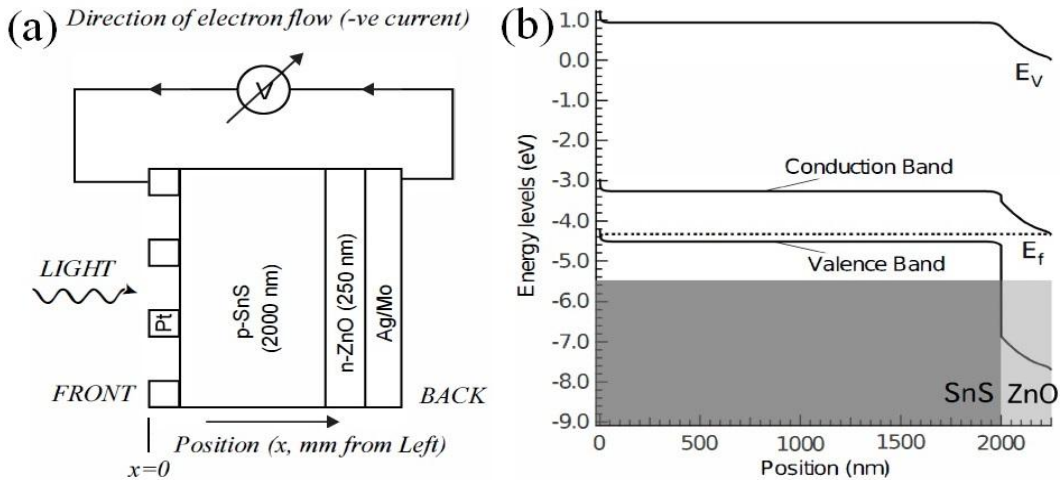

Figure 5-3. Simulation of SnS/ZnO thin film solar cells by AMPS-1D: (a) schematic of SnS/ZnO thin film solar cells with Pt and Ag/Mo conctact (b) Energy band diagram of SnS/ZnO thin film solar cells. E_f is Fermi level and E_V is vacuum level. (Ref. [46]).

In order to realize this simulation, SnS thin film deposition and characterization was begun by the Horn & Brownson group. SnS thin films were deposited by radio frequency magnetron sputtering [38, 40, 47]. A wide variety of SnS thin films were deposited and all were nearly stoichiometric (1:1 of tin to sulfur ratio) films. Significant changes of the films in the shape, size and density of crystallites were observed under various deposition conditions. XRD patterns of all the samples were well-matched to herzenbergite SnS and preferential growth orientations were (111) and (101). For optical analysis, spectroscopic ellipsometry (SE) was utilized. The absorption coefficient as a function of energy is shown in Fig 5-4. The figure shows

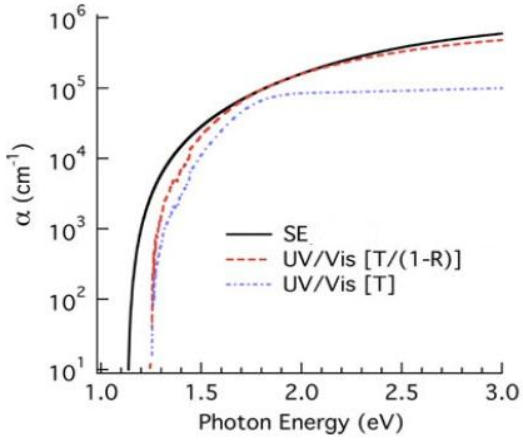

Figure 5-4. Absorption coefficient obtained by SE (spectroscopic ellipsometry) and UV/Vis (ultraviolet-visible spectrophotometry). Black bold is the absorption coefficient obtained by SE. Red and blue dashed lines are the absorption coefficients from UV/Vis by considering reflection and by ignoring reflection, respectively (Ref. [38]).

good agreement between the modeled SE data and that measured with UV-vis transmittance and reflectance, in particular, in higher energy region. A high absorption coefficient of $>10^5$ cm^{-1} at >1.6 eV of photon energies is shown. In addition, a 1.2-1.3 eV of indirect gap, 1.3-1.34 eV of the forbidden gap and 1.47-1.55 eV of direct gap has been calculated [38].

Recently, it has been reported on the possible existence of multiple phases in SnS thin films sputtered [40]. Rietveld anlaysis of XRD patterns confirms the existence of the multiple phases as shown in Table 5-4. It is found that although the predominant phase is the herzenbergite phase, a secondary peak such as orthrthorombic (Cmcm) or cubic ($Fm\bar{3}m$) can exist in the SnS films, depending on the deposition parameters. Also, it is reported that deposition rate is the essential parameter to decide the phase randomness and substrate heating suppresses changes by various deposition modes [40].

PDF Card Number	Crystal Structure	Polymorph	Space Group	Lattice Parameter (Å) a	b	c	Notes
39-354	Herzenbergite	α-SnS	Pbnm	4.3291	11.1923	3.9838	Standard card quoted in the literature
4-4-3831	Orthorhombic	β-SnS	Cmcm	4.128	11.48	4.173	Data collection at 1000K
4-4-3833	Herzenbergite	α-SnS	Pbnm	4.242	11.32	4.05	Data collection at 700K
4-4-8426	Cubic	Rock Salt	$Fm\bar{3}m$	5.8	5.8	5.8	Compound preparation: epitaxial growth onto (100)NaCl at 670-770 K
4-4-8696	Herzenbergite	α-SnS	Pbnm	4.32	11.15	3.97	Data collection at 300K

Table 5-4. Summary of card data for potential SnS phases (Ref. [40]).

5.2 Motivation for Research of Sputtered SnS

Tin Sulfide is of great interest for promising absorber materials in a field of solar cells. Since tin sulfide materials themselves are abundant in earth crust and non-toxic, SnS thin films are more advantageous in environmentally friendly solar cell applications when compared with other thin film light absorber materials such as CdS and CdTe. Moreover, SnS exhibits more than 10^4 cm^{-1} of high absorption coefficient at fundamental absorption edge and its band gap reported by research groups is ~1.3 eV, which is close to the ideal value that Loferski suggested [4, 35].

As of now, SnS thin films have been deposited by various physical and chemical methods. For example, thermal evaporation, electron beam evaporation, radio frequency sputtering, spray pyrolysis, atomic layer deposition, chemical vapor deposition and chemical bath deposition have been used for the preparation [4, 6-14, 20, 21]. These research groups have investigated on the morphological, optical electrical properties of the SnS thin films by the multiple deposition techniques. However, previous research is inconclusive as to what is the best choice of the film for solar cell fabrication. Considering mass production in the thin film solar cell industry that will be expected for SnS thin films, a physical vapor deposition technique such as radio frequency sputtering or evaporation should be highlighted. Among these two techniques, only a few research groups have investigated SnS thin film deposition by sputtering while

evaporation has been extensively studied as a SnS deposition tool [4, 6, 8-10, 20, 21]. Further fundamental research on the SnS thin film formation by RF sputtering is necessary for the realization of efficient and economical commercial SnS solar cells.

In this chapter, SnS thin films deposited radio frequency sputtering for solar cell application are discussed. Several SnS thin films were prepared with various deposition conditions such as deposition power, deposition pressure, throw distance and substrate temperature to understand the effect on SnS thin films depending on the deposition parameters. In order to understand their properties, the deposited SnS thin films were characterized morphologically, optically and electronically by field emission scanning electron microscope, atomic force microscope, X-ray diffraction, spectroscopic ellipsometry and transfer length method for film resistivity. The possible solar cell structures for these sputtered SnS thin films are also demonstrated.

5.3 Experimental Section

5.3.1 SnS Thin Film Deposition by RF Magnetron Sputtering

Tin monosulfide thin films were deposited in a Radio-Frequency (RF) magnetron sputtering system in a downward vertical geometry under Ar plasma atmosphere as shown in Figure 5-5 (a) and (b). High vacuum was achieved using a turbo molecular pump with backing-up roughing pump. Argon plasma ignition was accomplished at 30 mTorr and 115 W with target shutter closed. Predepositions were carried out at desired deposition pressure and power ranging from 10 to 50 mTorr and 105 W-155 W, respectively for 2 min. After that, a SnS thin film was deposited at the desired deposition pressure and power. The range of the reflected power for the

film deposition was from >5 W to ~25 W, depending on deposition power. The target used for these depositions was SnS of 99.999% purity (LTS Research Laboratories, Inc.) and was 3 inches in diameter. Tin monosulfide films were deposited by RF-magnetron sputtering onto crystalline silicon wafers covered with 500 Å of silicon nitride (SiN_x) and transparent slide glasses with or without substrate heating. Colloidal graphite was painted on the substrates prior to deposition. After deposition, the painted graphite was removed with isopropyl alcohol in ultrasonic bath to provide a step for profilometry measurements.

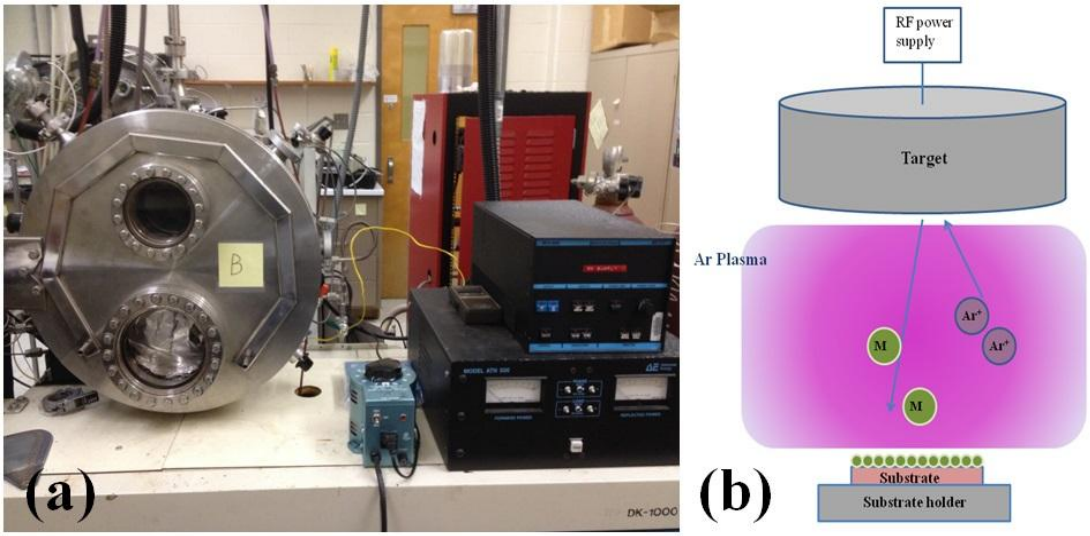

Figure 5-5. SnS thin film deposition by radio-frequency magnetron sputter: (a) deposition setup and (b) schematic showing sputtering under Ar plasma atmosphere for SnS thin film deposition.

5.3.2 Characterization of SnS Thin Films

Several characterization methods have been used to characterize these films. Profilometry measurements in conjunction with spectroscopic ellipsometry (SE) have been used to determine

thickness and growth rates of the films and to extract extinction coefficient, κ for the calculation of the absorption coefficient, α. SE measurements show comparable thicknesses to the profilometry measurements. Details for calculation will be discussed in Chapter 5.4.2. Field emission scanning electron microscopy (FESEM, Leo 1530) and atomic force microscopy (AFM) were used to examine the surface morphology of the SnS thin films. Root mean square (RMS) roughness of the films was determined by AFM. Resistivity for SnS films was obtained from transfer length method (TLM) on probe station. In each section, the specific analysis method and the instrument used will be discussed in detail.

5.4 Results & Discussion

In this chapter, various aspects of SnS thin films by RF magnetron sputter are examined. Chapter 5.4.1 investigates varying morphological and crystal structural features of the SnS thin films, depending on deposition parameters: deposition power, deposition pressure, throw distance, and substrate temperature. Optical properties of the SnS thin films are studied in Chapter 5.4.2 with spectroscopic ellipsometry. Chapter 5.4.3 provides the electrical properties obtained with transfer length measurement. The attempts at the fabrication of the SnS thin film solar cells will be shown in Chapter 5.4.4.

5.4.1 Morphology and Crystal Structure of SnS Thin Film Sputtered by RF Power

Figure 5-6 shows surface morphologies of SnS films deposited by RF sputter at deposition pressure of 10 mTorr and 30 mTorr, respectively with various RF power. All SnS films deposited at 10 mTorr exhibit an elongated grain shape, which is called “rice-like” grain,

with lots of voids in the top view. This rice-like morphology is similar to that reported by another group [10]. The length of the elongated grain size of SnS is ~100 [nm]. No significant changes in morphology is found among Figure 5-6 (a), (b) and (c) in spite of the variation in RF power from 155 W to 105 W. SnS films shown in Figure 5-4 (d) through (f) were prepared at 30 mTorr with different RF power. This set of samples also appears to have similar morphologies regardless of RF power magnitude change. The depositions were done with similar rate for each set of sample as shown in Figure 5-7 (a). The thickness of each film was (a) 214 nm (b) 239 nm (c) 212 nm (d) 73 nm (e) 76 nm and (f) 81 nm, respectively in Figure 5-6.

X-ray diffraction patterns follow the tendency in morphology. As shown in Figure 5-7 (b), a set of SnS samples have reflections on (110), (120), (021), (101), (111), (131), (002), (211), (112), (042) and (212). These reflections are well-matched to herzenbergite SnS phases as both in our previous reports (PDF #: 39-354) [38, 40, 47] and in other groups by various deposition techniques with (101) and (111) predominant peaks [10, 11, 16, 26]. Most sputtered SnS films had either (111) or both (101) and (111) phases as preferred growth orientation. Almost the same XRD patterns were observed each set of samples in Figure 5-7 (b) and (c). Large reflection at ~55° including a shifted peak at ~54° is attributed to the Si_3N_4/Si substrate, which may be resulted from porous and columnar nature of deposited SnS film with thin thickness (few hundred nanometers). It is noted that (111) or (101) XRD peak in Figure 5-7 does not exactly match the reference peak provided XRD software. It is possible that this distortion in XRD pattern is resulted from strain in the film and variation of the lattice constant, which is caused by interfacial interaction between the film and the substrate as reported by Nozaki et al. [39]. In the similar aspect, our group reported that α-SnS (herzenbergite structure) itself can have various lattice constants as in Table 5-4 under different crystal formation energy conditions. This can cause the distortion in XRD pattern [40]. More importantly, this indicates that the SnS depositions are affected by the energy applied during the deposition. In order to elucidate the origin of these

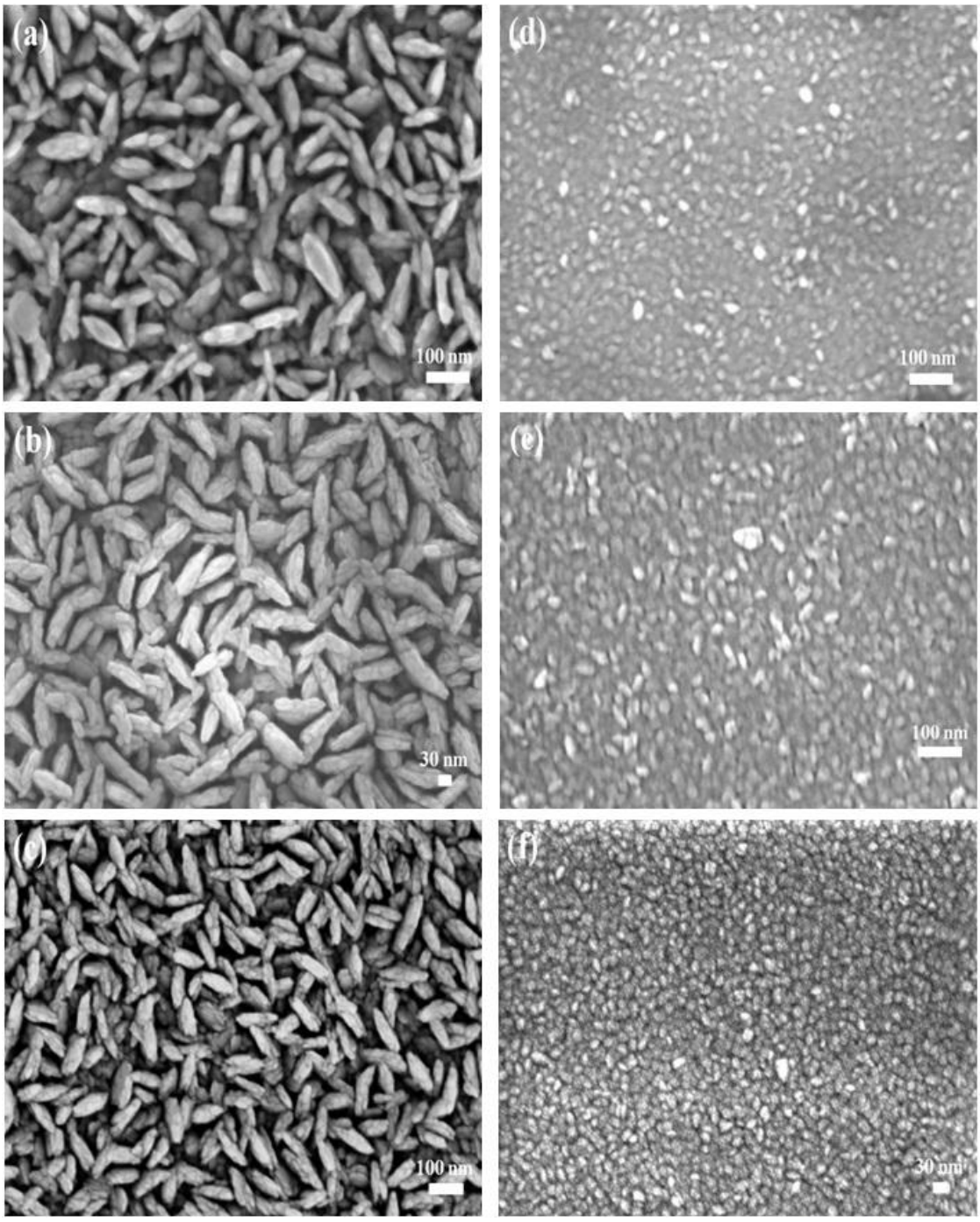

Figure 5-6. Deposition power dependence: SnS films sputtered with (a) 155 W at 10 mTorr, (b) 115 W at 10 mTorr and (c) 105 at 10 mTorr, (d) 155 W at 30 mTorr (e) 145 W at 30 mTorr (f) 105 W at 30 mTorr. All these samples were deposited in 17 cm throw distance for 10 min at room temperature.

findings or to understand the relationship between SnS deposition and the crystal formation above, the mean free path of vapor flux should be considered first. The mean free path, ℓ, is expressed as below,

$$\ell = \frac{1}{\sqrt{2}\pi a^2 n} \tag{5.1}$$

where a is the molecular diameter and n is the gas concentration [41]. Also, the gas concentration can be expressed as,

$$n = \frac{pN_A}{R_g T} \tag{5.2}$$

where p is the pressure, N_A is Avogadro's number, R_g is the gas constant and T is the temperature in absolute number. The equation (5.1) and (5.2) indicate that high pressure provides higher gas concentration and shorter mean free path and vise versa. Considering a typical molecule with 0.3 nm diameter at 10 mTorr at 25 ℃, the mean free path is 0.78 cm following the equation (5.1) and (5.2). Hence, according to the definition of Knudsen number, Kn below,

$$Kn = \frac{\ell}{L} \tag{5.3}$$

where L is the distance between the source and substrate. The 0.78 cm mean free path, in this case, is included in the intermediate range, considering 17 cm throw distance here since Knudsen diffusion is dominant for Kn >1 and vapor transport by molecular diffusion is dominant for Kn<0.01 [41]. In the intermediate range, collisions and scattering with other gas species are not negligible in this case and the transport of the vapor flux led by two diffusion mechanisms, namely, Knudsen diffusion and the molecular diffusion. Hence, the total diffusion, J is expressed below [41, 48],

$$J = -D_{Ae}\frac{dn}{dx} \tag{5.4}$$

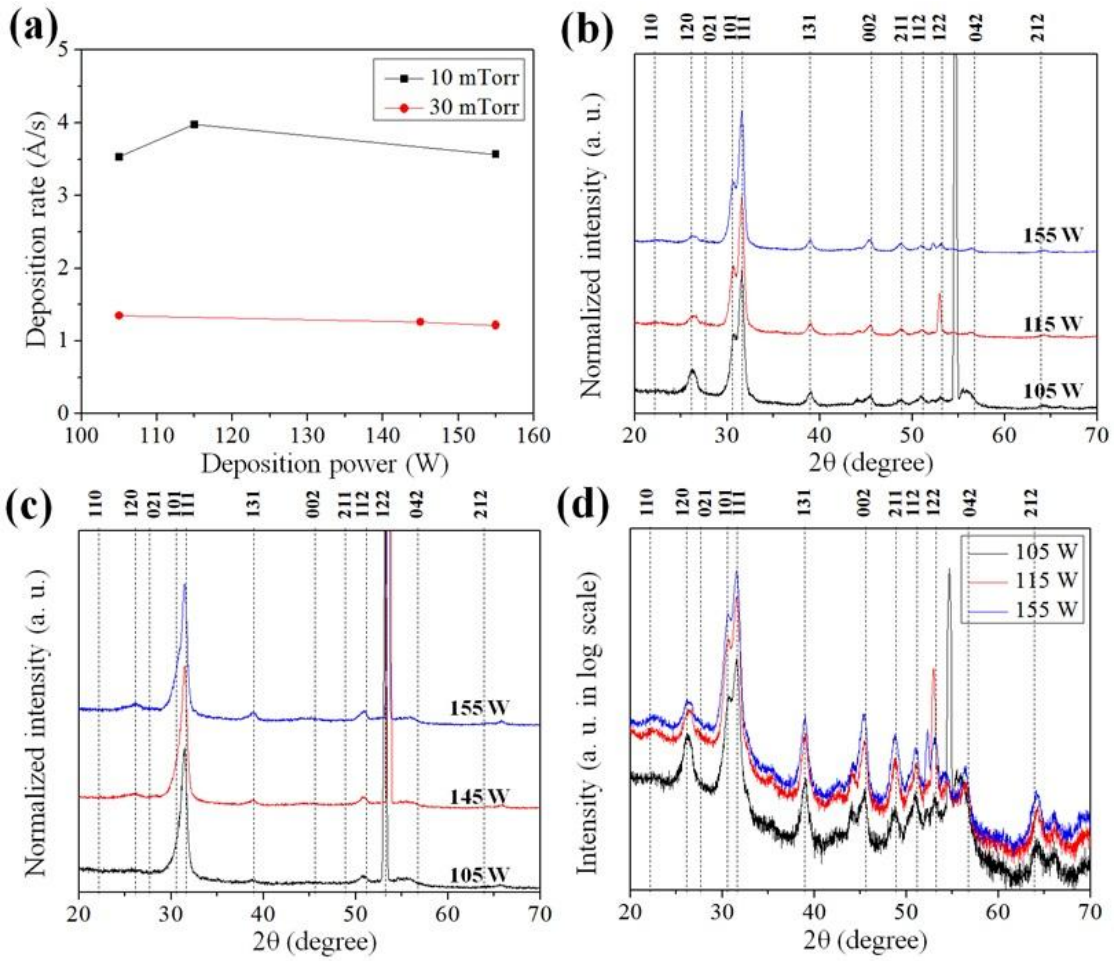

Figure 5-7. SnS films by varied deposition power: (a) deposition rate Vs deposition power, normalized X-ray diffraction pattern of SnS films sputtered (b) at 10 mTorr with 105 W, 115 W and 155 W (c) at 30 mTo rr with 105 W, 145 W and 155 W. (d) X-ray diffraction pattern in log scale for Figure 5-6 (b). All these samples were deposited in 17 cm throw distance for 10 min at room temperature.

where D_{Ae} is effective diffusion coefficient and dn/dx is one dimensional concentration gradient.

The effective diffusion coefficient, D_{Ae} is expressed as [48],

$$\frac{1}{D_{Ae}} = \frac{1}{D_{KA}} + \frac{1}{D_{AB}} \tag{5.5}$$

where D_{KA} is Knudsen diffusion coefficient and D_{AB} is binary gas phase diffusion coefficient. In equation (5.5), since D_{KA} is proportional to L while D_{AB} is proportional to ℓ, $D_{Ae} \approx D_{AB}$. The

vapor flux flow in this situation can be explained with molecular diffusion. Since D_{AB} is also proportional to mean speed of molecule, it is found that the deposition in this situation is related to the kinetic energy of vapor flux.

Therefore, small differences XRD pattern in log scale (Figure 5-7 (c)) by varied power power, which are found at ~25° and ~45° are possibly caused by the fact that higher power deposition provides vapor flux with higher initial kinetic energy and contributes to either the formation of more crystallites or the various formations of SnS polymorphs by the energy.

Another finding from the Figure 5-7 (b) and (c) is the presence of (101) growth orientation. A 10 mTorr deposition includes the (101) peak in Figure 5-7 (b) but the 30 mTorr has no (101) growth orientation in Figure 5-7 (c). Since the set of the samples were deposited under 30 mTorr in Figure 5-7 (c), ℓ is 1/3 shorter than that under 10 mTorr. This means that vapor flux has more chance to experience collision and scattering and to lose their kinetic energy during their travel to the substrate. Therefore, it is surmised that (101) peak is related to higher energy deposition.

The effect of deposition pressure on the growth of SnS deposited at 105 W and 155 W of RF power is shown in Figure 5-8. As shown in Figure 5-8 (a) through (c), like the previous results of SnS films deposited with 10 mTorr above, SnS samples sputtered with 105 W at 10 mTorr show rice-like morphology but the surface morphology of the SnS thin films turns into the film with smaller round shape grains as deposition pressure increased. The crystallite size of the SnS films decrease into few nanometers length at 50 mTorr deposition as the deposition pressure increase. This transition in grain shape is found in the set of other SnS films prepared with 155 W in Figure 5-8 (d) to (f) in the same manner. At this time, deposition rate were dependant on deposition pressure as shown in Figure 5-9 (a). The thickness of each sample investigated here was (a) 214 nm (b) 81 nm (c) 30 nm (d) 174 nm (e) 73 nm and (f) 51 nm, respectively in Figure 5-8.

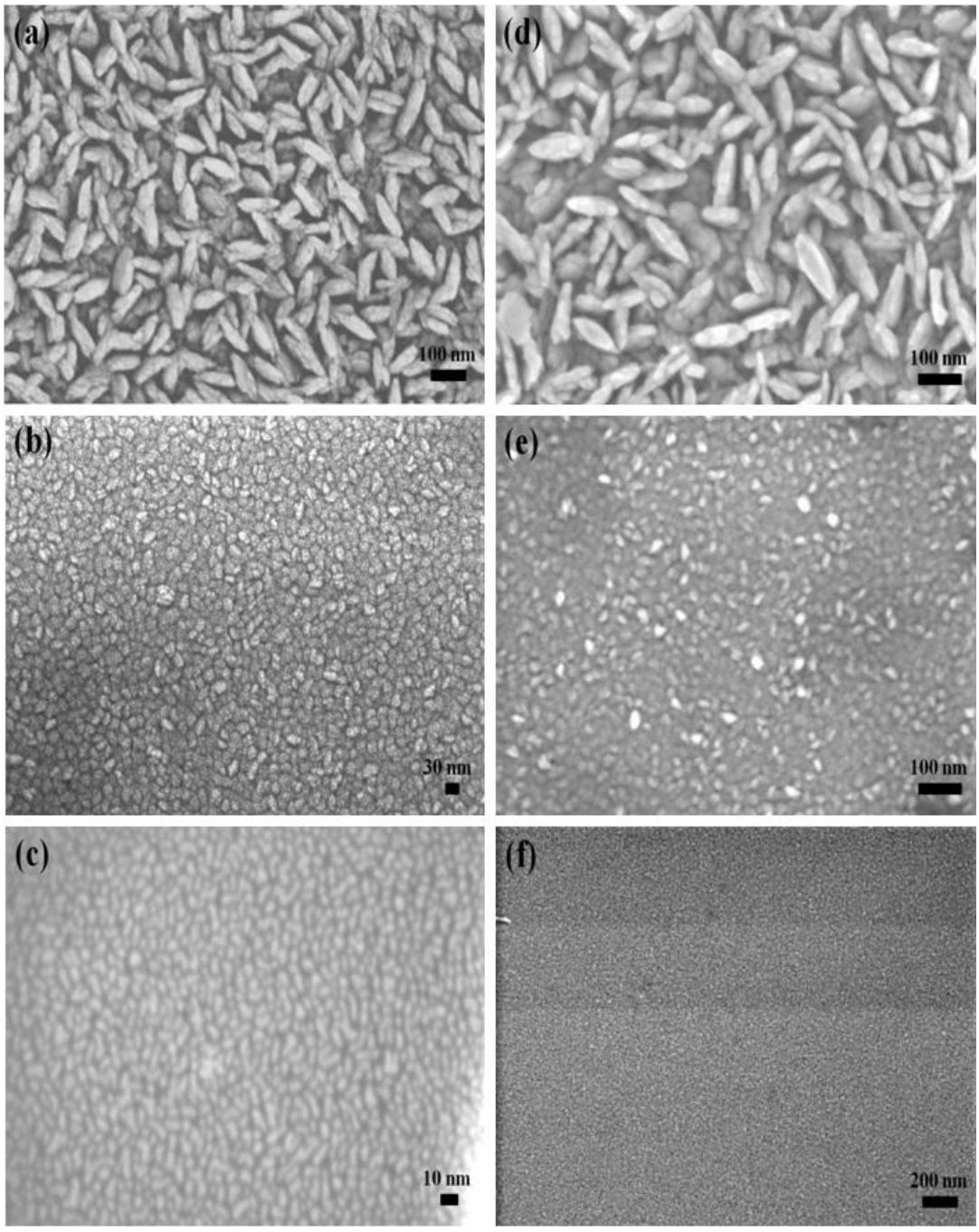

Figure 5-8. Deposition pressure dependence: SnS film sputtered with (a) 105 W at 10 mTorr, (b) 105 W at 30 mTorr (c) 105 W at 50 mTorr (d) 155 W at 10 mTorr (e) 155 W at 30 mTorr (f) 155 W at 50 mTorr. All samples were deposited for 10 min with 17 cm throw distance at room temperature.

XRD results in Figure 5-9 (b) and (c) reflect the transition in surface morphology. Although large peak still exists from substrate due to the thin thickness of the films, the XRD pattern for the most of the SnS thin films in Figure 5-9 (b) and (c) represent (101) or (111) growth orientation like in above experiment, again, being well-matched to herzenbergite SnS phases. The remarkable difference between higher and lower pressure depositions is that the number of growth orientations is limited in higher pressure deposition. The SnS thin films in Figure 5-8 (b), (c), (e) and (f) exhibit only two or three phases with an amorphous hump while the SnS thin films in Figure 5-8 (a) and (d) have relatively more growth orientations. Moreover, like in Figure 5-6 and 5-7, (101) phase is observed in the SnS thin film deposited only under 10 mTorr deposition pressure in Figure 5-9 (b) and (c).

Considering the fact that all the depositions implemented under 10 mTorr, 30 mTorr and 50 mTorr shown in Figure 5-8, the depositions are carried out in the intermediate range by equation (5.1) through (5.3) owing to large L. In particular, the deposition under 50 mTorr of deposition pressure has nearly 0.01 of a Knudsen number. This means that the vapor flux is transported by molecular diffusion and almost no Knudsen diffusion occurs in this condition. For all SnS samples here, the total molecular diffusion during the deposition, J can be explained as below,

$$J = -D_{Ae}\frac{dn}{dx} = -\left(\frac{1}{4}\bar{c}\ell\right)\frac{dn}{dx} \tag{5.6}$$

Where D_{Ae} is the effective diffusion coefficient, dn/dx is one dimensional concentration gradient and $\bar{c}$ is the mean speed of molecule [41]. It is obvious that when the vapor flux travels in lower pressure (e.g. 10 mTorr), the vapor flux will experience less collision and scattering with other gas species, which means longer mean free path helps to conserve the kinetic energy of vapor flux more efficiently. That is to say, higher $\bar{c}$ is expected in shorter ℓ when the vapor flux arrived

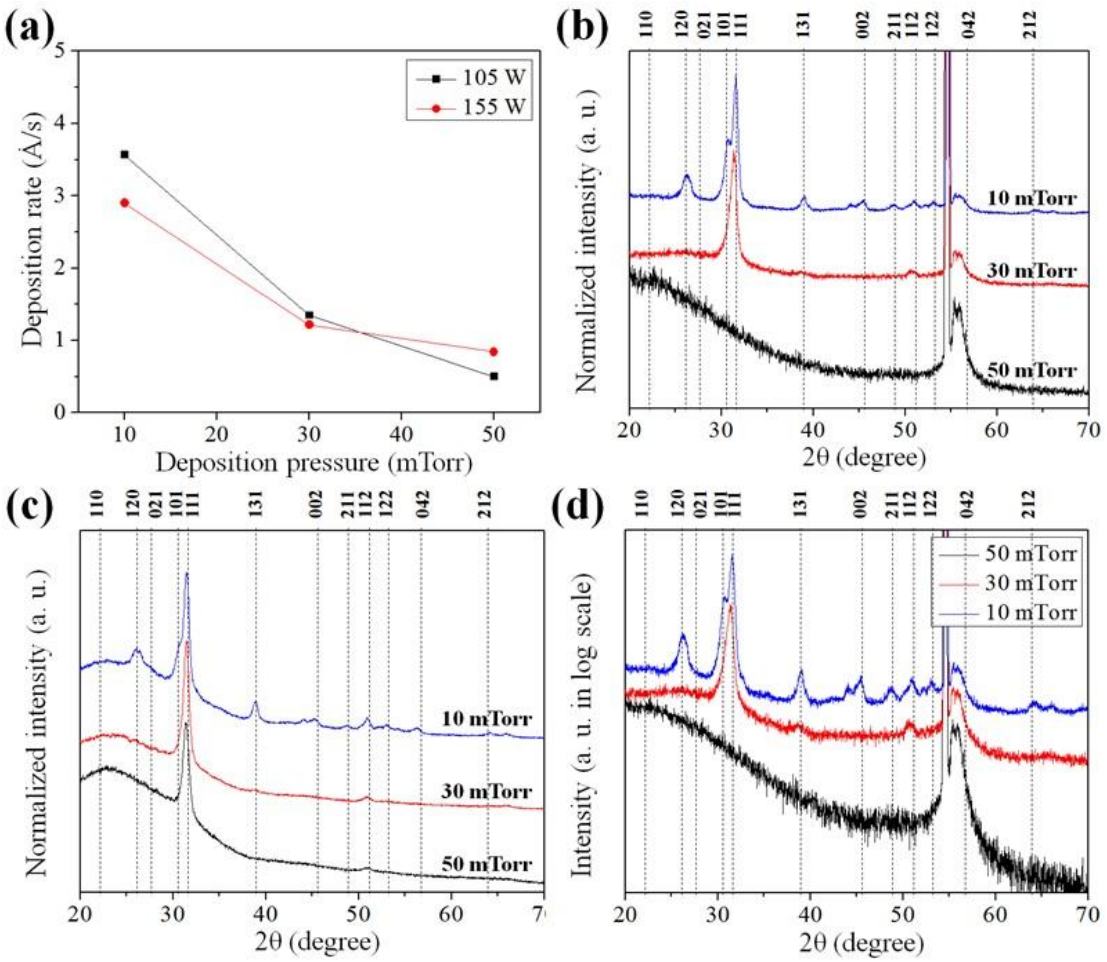

Figure 5-9. SnS films by varied deposition pressure: (a) deposition rate Vs deposition pressure, normalized X-ray diffraction pattern for SnS films sputtered (b) with 105 W at 10 mTorr, 30 mTorr and 50 mTorr (c) with 155 W at 10 mTorr, 30 mTorr and 50 mTorr (d) X-ray diffraction pattern for Figure 5-8 (b). All samples were deposited in 17 cm throw distance at room temperature.

at the substrate. So, the deposition with higher energy is favorable in formation of more crystallites in various growth orientations. In addition, the fact that (101) phase are only measured with the samples under 10 mTorr pressure reconfirms the speculation that (101) phase is related to higher energy deposition.

In another aspect, the lower pressure deposition condition is favorable for more vapor flux diffusion than that in higher pressure due to longer mean free path and subsequent enhanced diffusion coefficient. This larger diffusion also attributes to higher deposition rate onto the substrate during the deposition. For example, the deposition rate of SnS thin films under 10 mTorr, 30 mTorr and 50 mTorr with 105 W power (Figure 5-8 (a)-(c)), are 2.9 Å/s, 1.22 Å/s, and 0.23 Å/s, respectively.

Another important finding from Figure 5-9 (b) and (d) is that additional reflection that is not matched to herzenbergite SnS was measured at ~44°. This indicates that secondary peaks formed by various SnS polymorphs having another crystal structure such as orthorhombic or cubic structure can exist in herzenbergite SnS as reported by our group [40]. Under high-energy deposition, formation of such various phases for SnS is probable, following the Table 5-4. It has been known that the rock salt form of SnS has slightly larger energy of formation than that of α-SnS and β-SnS has the largest energy of formation [42]. Therefore, the SnS thin films deposited here can includes additional peaks possibly from rock salt or β-SnS structure other than the peaks from herzenbergite crystal structure and this results in difference in XRD pattern from Figure 5-9 (b) and (c).

Moreover, the energy provided from vapor flux onto deposited film possibly also has an influence on the surface morphology. Since the deposition under lower pressure takes place with higher energetic vapor flux, more energetic adatoms can diffuse further onto the surface of the SnS film during lower pressure deposition to form additional phases with higher energy. It is speculated that this surface diffusion by the energetic adatoms and the subsequent formation of a high-energy phase stimulate the vertical direction growth as shown in Figure 5-8 (a) and (d). In contrast to this, higher deposition pressure, such as 50 mTorr, leads to a slower deposition rate and vapor flux transport with relatively lower energy due to more possibility of higher collision and scattering during deposition owing to reduced mean free path. This higher pressure

deposition facilitates lower energy crystal formation with less crystallinity. In the end, denser and thinner films are obtained under higher pressure such as shown in Figure 5-8 (c) and (f).

In Figure 5-10, the effect of throw distance for SnS thin film deposition is investigated. As shown in the examples in Figure 5-10, SnS thin films were prepared at throw distances of 6.5 cm, 12 cm, and 17 cm, respectively at a 10 mTorr deposition pressure. Although Figure 5-10 (b) and (c) appears to be similar other than less lateral growth in Figure 5-10 (b), Figure 5-10 (a) that is deposited at 6.5 cm exhibits a visible difference in surface morphology. So-called "rice-like" crystallites are not observed any longer in Figure 5-10 (a). Larger and more bulky features are contained in the film instead. The deposition rate was increased as throw distance was increased as in Figure 5-11 (a). The film thickness of each sample used was (a) 1057 nm (b) 381 nm, and (c) 281 nm, respectively in Figure 5-10.

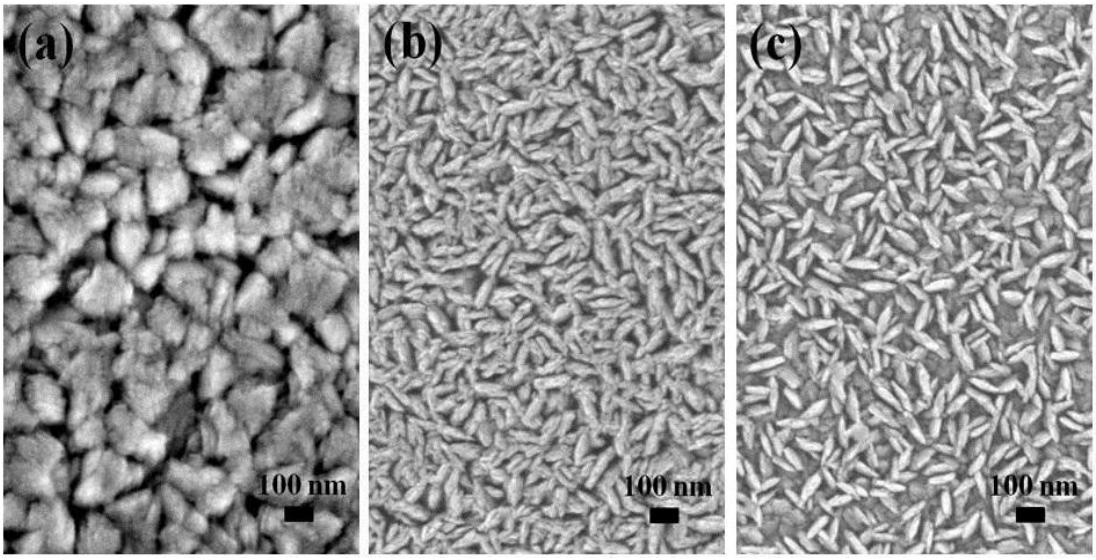

Figure 5-10. Deposition pressure dependence: SnS film sputtered at the throw distance of (a) 6.5 cm (b) 12cm (c) 17 cm. All samples were deposited with 155 W under 10 mTorr at room temperature. The deposition time was 10 min.

This change is also observed in XRD pattern from Figure 5-11 (b)-(d). A shorter throw distance yields a more narrow intensity peaks in (111) and (101) angles. This implies that shorter throw distance deposition is favorable to obtain more crystallized SnS thin films. In addition, some differences are observed in secondary growth orientations. The differences in reflections between the SnS thin films are measured at ~44°, 55° and 66° as shown in Figure 5-11. It is surmised that this additional growth orientation in the films or change in the preferential growth orientations has an influence on the surface morphology of the SnS thin film. These differences

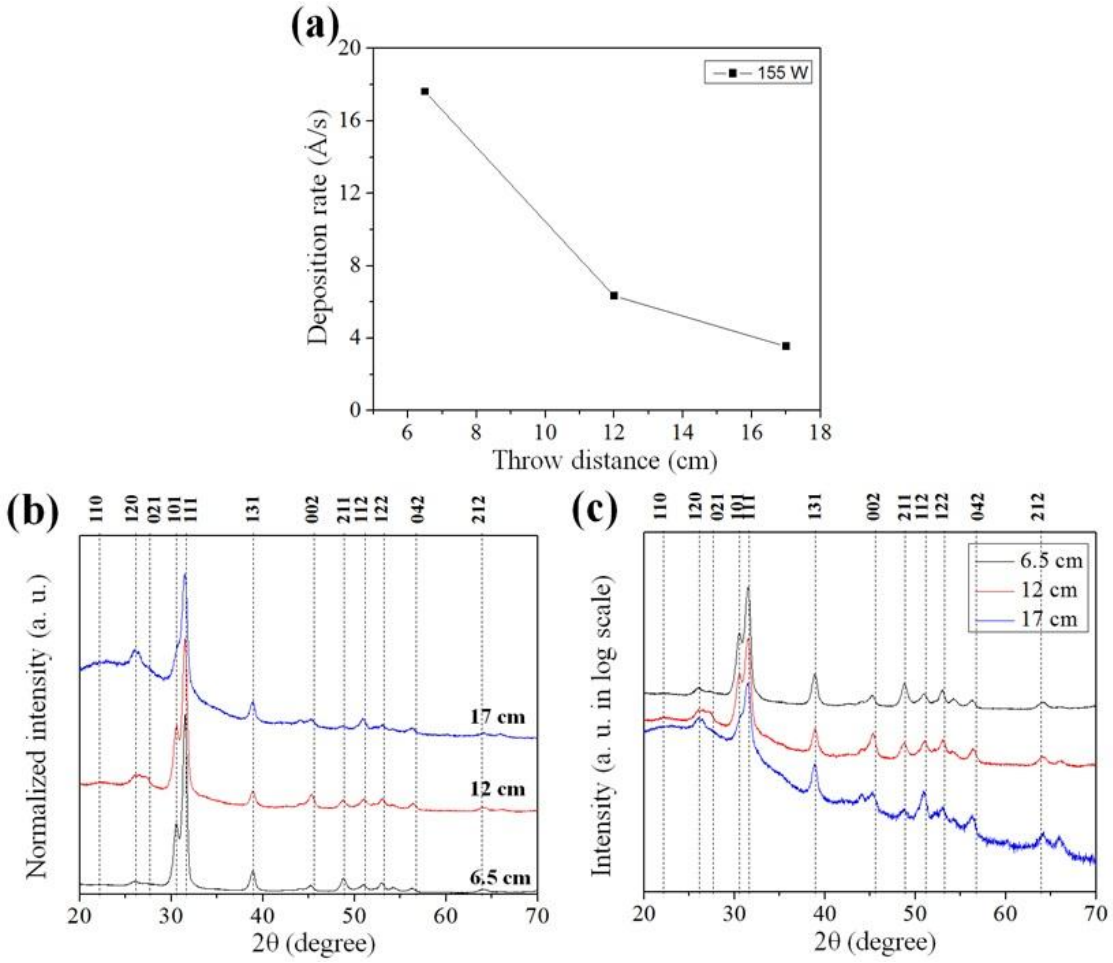

Figure 5-11. SnS thin film by varied throw distance: (a) deposition pressure Vs throw distance, (b) normalized and (c) log scaled X-ray diffraction pattern for the samples from Figure 5-10.

facilitate the growth of the film not only in vertical but also lateral direction as shown in Figure 5-10 (a).

This change in surface morphology and XRD pattern also can be explained by the mean free path and kinetic energy of vapor flux. Reduced throw distance leads larger Knudsen number, following the equation (5.3), and, at the same time, this indicates lesser possibility of collision and scattering, and vapor flux with higher energy reaching to the substrate. In the end, this shorter throw distance helps the SnS thin film to form higher energy crystal structure and, thereby, the SnS thin film is possible to include secondary phases such as rock salt or β-SnS which other than those of herzenbergite phases. These findings suggest that the SnS film is able to form secondary crystal structure when the film is grown with higher energy, at this time using a reduced throw distance.

Moreover, according to the change in throw distance, large difference in deposition rate is observed. The deposition rates were 17.62 Å/s, 6.35 Å/s and 3.57 Å/s when the depositions were implemented with 6.5 cm, 12 cm, and 17 cm of throw distances, respectively. Since the shortest throw distance is 6.5 cm and this distance is still much longer than mean free path of vapor flux, the equation (5.6) is still valid. As shown in equation (5.6), deposition rate is related to vapor flux diffusion. In this case, considering the fact that all these depositions were done in the same deposition conditions except for throw distance, diffusion transport is independent on the mean free path, ℓ However, the total diffusion is affected by the gradient of vapor flux, dn/dx since the diffusion is exponentially decreased in terms of distance—namely, shorter throw distance mode provides higher dn/dx,— and by mean speed of molecule, $\bar{c}$ due to consecutive collision. This leads to a larger diffusion and results in higher deposition rate that have an influence on the various oriented growth.

Figure 5-12 shows the SnS thin films deposited at various substrate temperatures. The substrate was heated with the heater installed the inside of the chamber in vacuum in order to study the annealing effect during deposition. Morphological changes of SnS thin films are observed by FESEM in Figure 5-12. The interesting changes in surface morphology are observed in Figure 5-12 (a)-(c). The depositions were done under 60 mTorr deposition pressure. The grain shape is changed with added heat in the form of elongated shapes which have been observed in

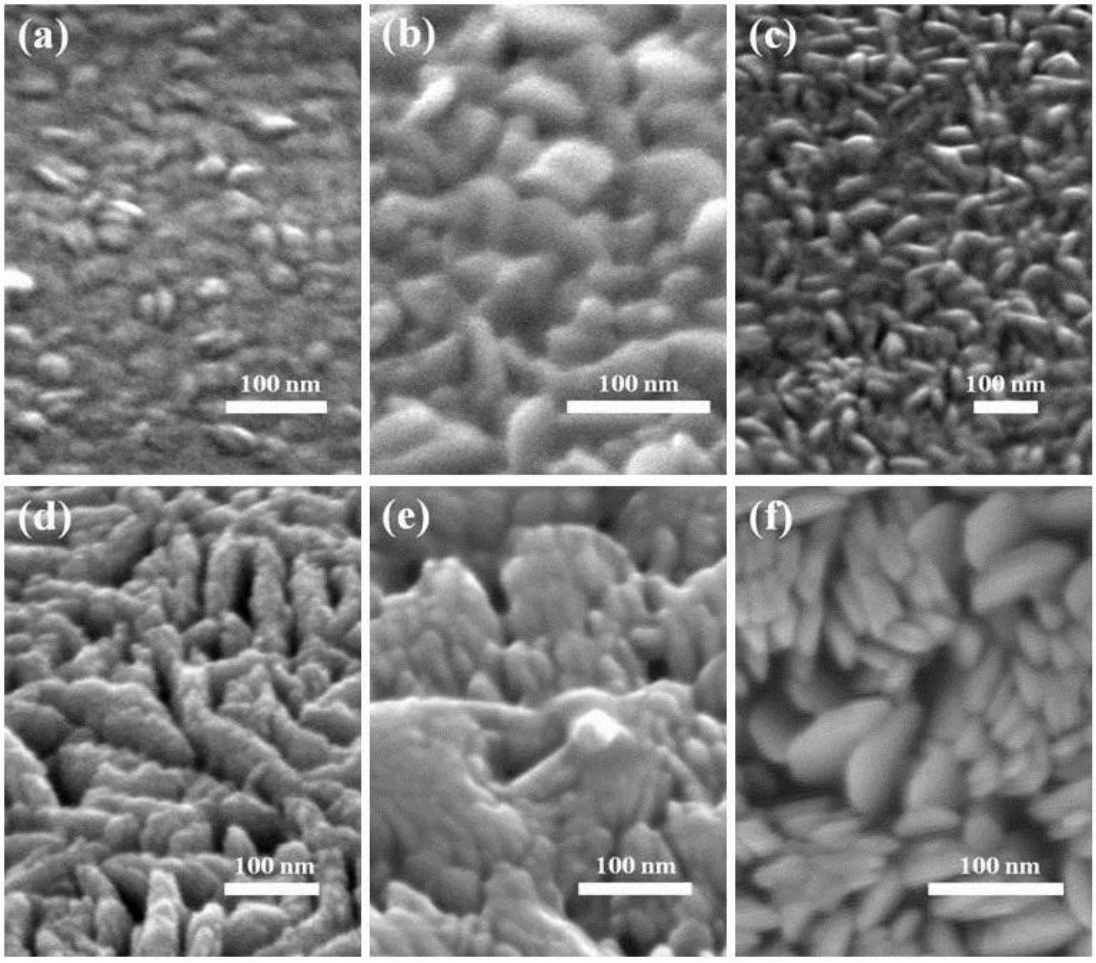

Figure 5-12. SnS film deposition with substrate heating at (a) room temperature (b) 149 ℃ (c) 281 ℃. (d) room temperature (e) 198 ℃ (f) 234 ℃. The samples of (a)~(c) and (d)~(f) were deposited at 60 mTorr for 20 min and 10 mTorr for 20 min, respectively with 155 W in 12 cm throw distance.

the deposition with lower pressure and higher energy. A set of the samples prepared at 10 mTorr pressure is shown in Figure 5-12 (d)-(f) which shows a change in morphology as the temperature changes. Unlike the set of the samples in Figure 5-12 (a)-(c), the samples at 10 mTorr deposition pressure in Figure 5-12 (d)-(f) are remarkable in lateral growth. The thicknesses of the samples used for this investigation were ~200nm for (a)-(c) and ~868 nm for (d)-(f), respectively in Figure 5-12.

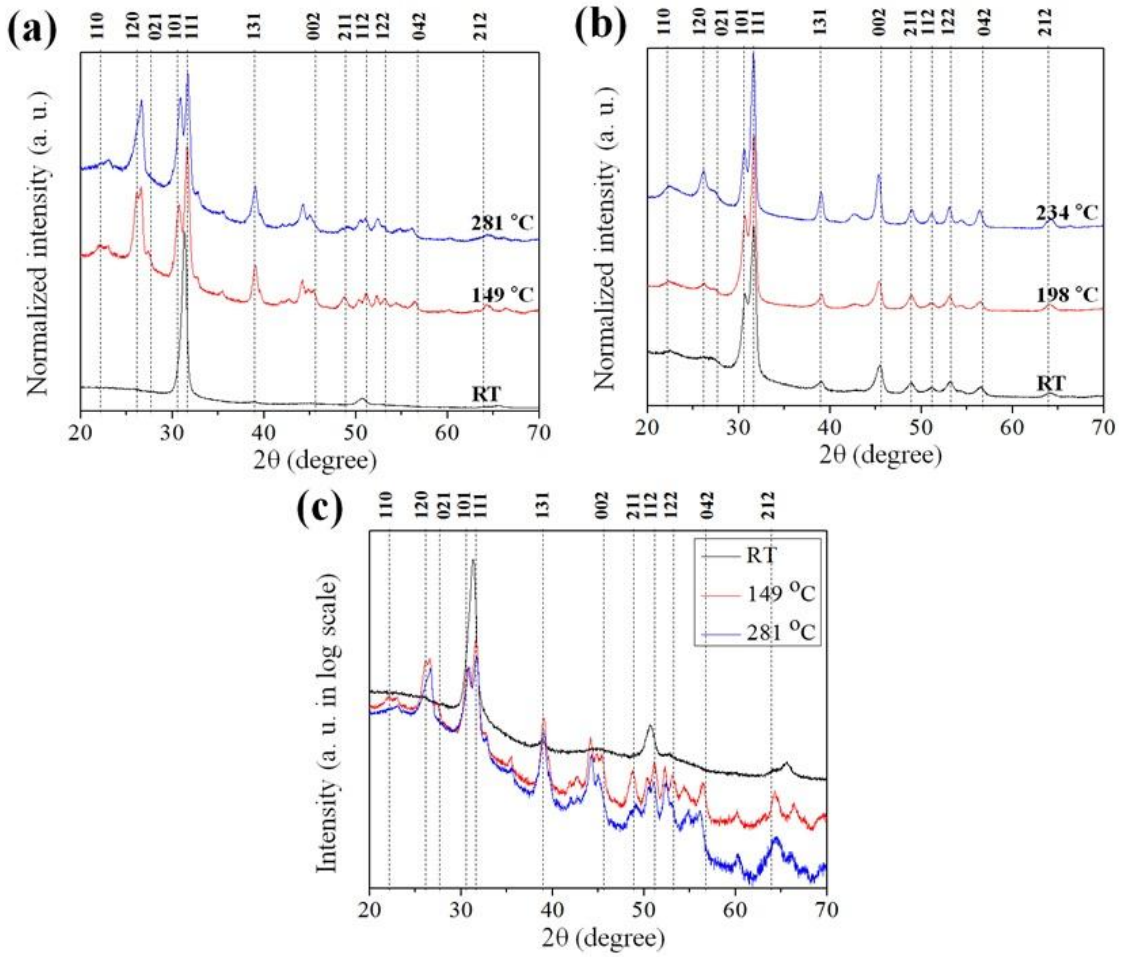

Figure 5-13. SnS thin films by varied substrate temperature: normalized X-ray diffraction pattern of the SnS film depositions with substrate heating at (a) RT (room temperature), 149 ℃ and 281 ℃ (from Figure 5-12 (a)-(c)), (b) at RT, 198 ℃ and 234 ℃ (from Figure 5-12 (d)-(f)) and (c) X-ray diffraction pattern in log scale (from Figure 5-12 (a)-(c)).

Figure 5-13 shows the XRD patterns for the SnS thin films in Figure 5-12. In an XRD study of these films shown in, especially, Figure 5-13 (a) and (c), the (101) orientation reflection which has been observed only in the deposition with lower pressure and higher energy from the SnS films prepared at 149 ℃ and 281 ℃ even if the SnS thin films were prepared at lower energy. The more growth orientations were measured in various peaks from the SnS thin films at higher temperature while SnS thin film deposited at RT has no (101) orientation reflection and exhibits limited growth orientations.

Moreover, heated samples during deposition exhibit additional growth orientations at 2 theta angles of ~35 °, ~44° and ~55°. Again, all findings from here prove that secondary phases exist with added heat, namely, with additional energy. In the same manner, Figure 5-13 (b) shows additional growth orientation at ~44° and narrower peaks in (120), (101) and (111) orientations. It is implied that further crystal structure change is possible with increased thermal energy.

5.4.2 Optical Properties of SnS Thin Film Sputtered by RF Power

The absorption coefficient, α is an essential parameter for determining absorption capability and bandgap of a semiconductor film. A general way of obtaining α is based on Beer-Lambert law shown with uniform α through the material below,

$$I(x) = I(0)\exp(-\alpha x) \tag{5.7}$$

where I(x) is the light intensity in terms of distance and I(0) is the intensity just inside of surface. Then, if the reflectance, R is negligible, the equation (5.7) can be expressed as below,

$$\alpha = -\frac{1}{d}\ln(T) \tag{5.8}$$

where d is thickness of the film and T is transmittance from I(x)/I(0).

In the same way, in case of nonnegligible R, the equation (5.8) can also be expressed as,

$$\alpha = -\frac{1}{d}\ln\left(\frac{T}{1-R}\right) \tag{5.9}$$

For a more convenient method for obtaining the absorption coefficient, a spectroscopic ellipsometer can be used [37, 38, 40, 47]. In particular, analysis, in conjunction with transmittance data using a structural model has been demonstrated by our group [38, 40]. The optical constants, namely, index of refraction, n and extinction coefficient, k were extracted from a SnS model that was based on Tauc-Lorentz and Cody-Lorentz oscillator. The α was obtained from the extinction coefficient measured by the SE system. Extraction of α follows the equation below,

$$\alpha = \frac{4\pi k}{\lambda} \tag{5.10}$$

where λ is wavelength in cm. Optical energy direct band gaps also were extracted from Tauc equation below.

$$\left(\alpha h\nu\right)^n = \beta\left(h\nu - E_g\right) \tag{5.11}$$

where α is absorption coefficient, h is plank constant, ν is frequency of photon, β is constant and E_g is optical bandgap and n is an exponent. In this equation, the band gap type is determined by n. $(\alpha h\nu)^2$ vs hν and $(\alpha h\nu)^{1/2}$ vs hν can be used for direct and indirect bandgap, respectively [4, 14, 15]. Here, in this section, equation (5.10) and (5.11) are used to assess the absorption coefficient and the bandgap of different SnS thin films based on the analysis method suggested by our group [38, 40].

In order to investigate optical properties of SnS thin films, several kinds of samples were chosen. Since higher power is favorable in obtaining higher deposition rate and analyzing sample easily, SnS films were deposited with 155 W at various deposition pressures and throw distances. The prepared samples are shown in Table 5-5 below. All these depositions were carried out at

room temperature for 10 min and the base pressure was 1 x 10^{-6} Torr. The samples in Table 5-5 were used in this section and the following section (Chapter 5.4.3) for optical properties and electrical properties, respectively.

Sample Name	Deposition Power (W)	Deposition Pressure (mTorr)	Throw distance (cm)
A	155	10	12
B	155	30	12
C	155	50	12
D	155	10	17
E	155	30	17
F	155	50	17

Table 5-5. SnS thin films by RF sputter.

Figure 5-14 shows the surface morphology investigated by atomic force microscopy (AFM). Just like in previous reports and the SEM pictures shown previously, the same porous structure with rice-like grains at lower deposition pressures were observed through AFM. The variation in size and shape of grains are identified, depending on deposition pressure variation and throw distance. The samples prepared at a lower deposition pressure in Figure 5-14 showed larger grain size and columnar shape while the samples made at higher deposition pressures show smaller and round shape grains as shown in Chapter 5.4.1. As shown in Figure 5-15 (a), deposition rate increased with decrease in deposition pressure and decrease in throw distance. Highest deposition rate was 6.35 Å/s in 10 mTorr with 12 cm throw distance and lowest deposition rate of 0.56 Å/s was observed in 50 mTorr with 17 cm throw distance. Figure 5-15 (b)

shows the Root mean square (RMS) roughness of the samples. The RMS roughness decreased generally with an increase of deposition pressure as shown in sample D through F. However,

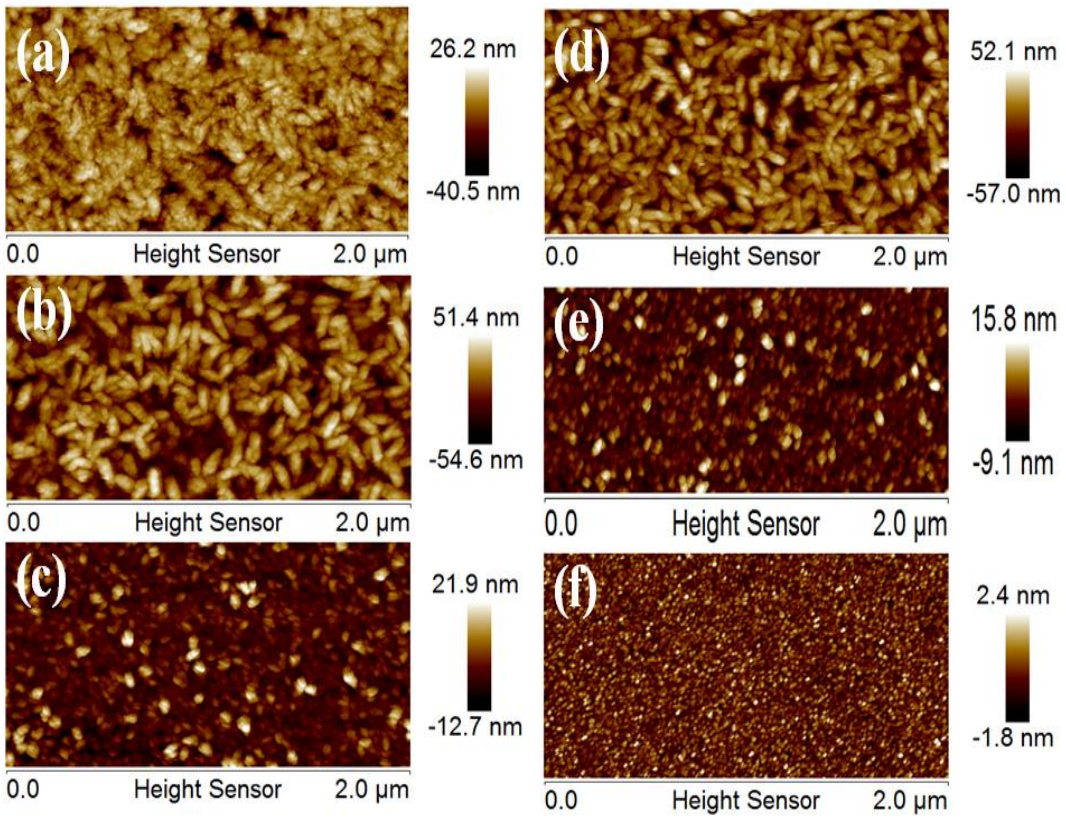

Figure 5-14. Surface morphologies of SnS films by atomic force microscopy. The films deposited with deposition parameters as shown in Table 5-3.

deviation from this tendency was observed in a set of the samples prepared with 12 cm throw distance samples. The RMS roughness of the sample A rather decreases in spite of the highest deposition rate among the samples.

This appears to be the results of the film growth in other crystal orientations. Since shorter throw distance has multiple growth orientations or different orientation growth patterns which are formed by higher energy during deposition except for (111) or (101) growth orientation

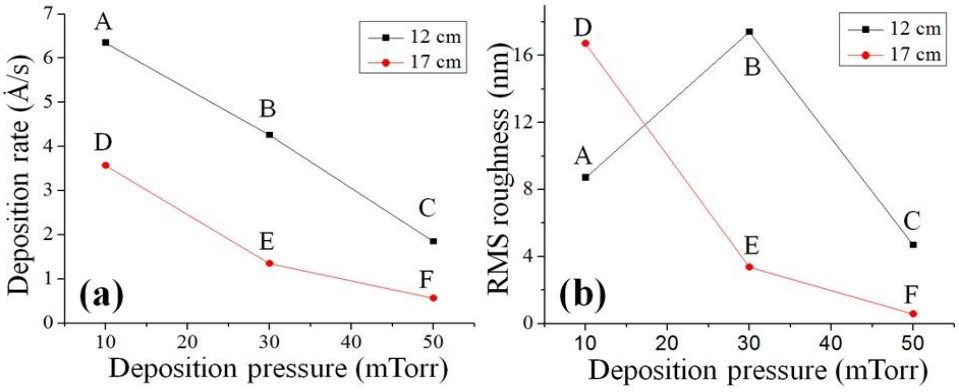

Figure 5-15. Deposition rate and RMS roughness of SnS films by change of deposition pressure and throw distance. All the samples are fabricated at room temperature.

as shown in Figure 5-11, the film becomes rather dense and compact even if the sample is deposited at a higher deposition rate.

Figure 5-16 shows the absorption coefficients for this series of SnS thin films, A through F, in terms of wavelength. All the prepared samples exhibit high absorption coefficients of more

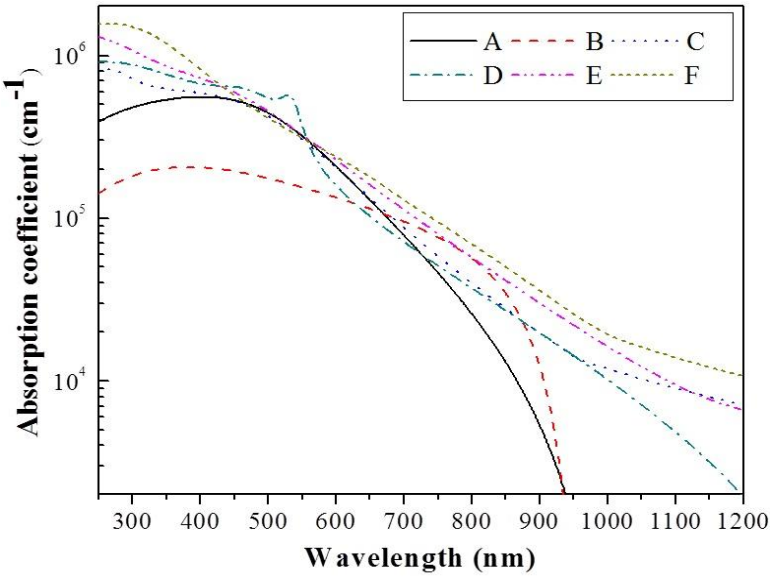

Figure 5-16. Absorption coefficient of SnS thin films.

than 10^4 cm^{-1} in the ultraviolet and visible range of wavelength, as reported in previous researches. In particular, the samples with relatively higher deposition pressure exhibit broader and higher absorption coefficient in longer wavelength region. For instance, sample C, E and F have almost 10^4 cm^{-1} even at 1100 nm and the absorption is very high in the range of <400 nm.

Figure 5-17 and 5-18 shows $(\alpha h\nu)^2$ Vs photon energy plot and $(\alpha h\nu)^{1/2}$ Vs photon energy for the calculation of direct and indirect bandgap, respectively following the equation (5.11), namely, the Tauc equation. Direct bandgaps of SnS films determined by the Tauc equation from Figure 5-17 are ranged from 1.33 to 1.55 eV and the indirect bandgaps are ranged from 1.07 to 1.39 eV, depending on the deposition conditions in Figure 5-18. All the values for the direct and indirect band gap are summarized in Table 5-6. In case of Figure 5-18, the indirect band gap obtained does not account for phonon energy since the indirect band gap values here mean the summation of the indirect band gap and phonon energy [49]. However, the values from Figure 5-17 are still meaningful since they provide the approximated values for indirect band gap with small phonon energy reported [49]. The remarkable point here is that all the samples exhibit higher absorption coefficient even in the range of longer wavelength than in their bandgaps. This indicates that the SnS thin films experiences high density of Urbach tail states below its conduction band edge or above it valence band edge, which is related to the distance of molecules or their orientation [43]. This is well-matched to the fact that the SnS thin films can have various polymorphs, depending on the deposition modes as mentioned in Chapter 5.4.1. In addition to this, absorption is possibly affected from high density of defect levels within the bandgap as found by Sajeesh et al [33]. The defect levels can be formed by unwanted oxidization of the films within bandgap. No noticeable tendency was found in the change of bandgap with deposition conditions.

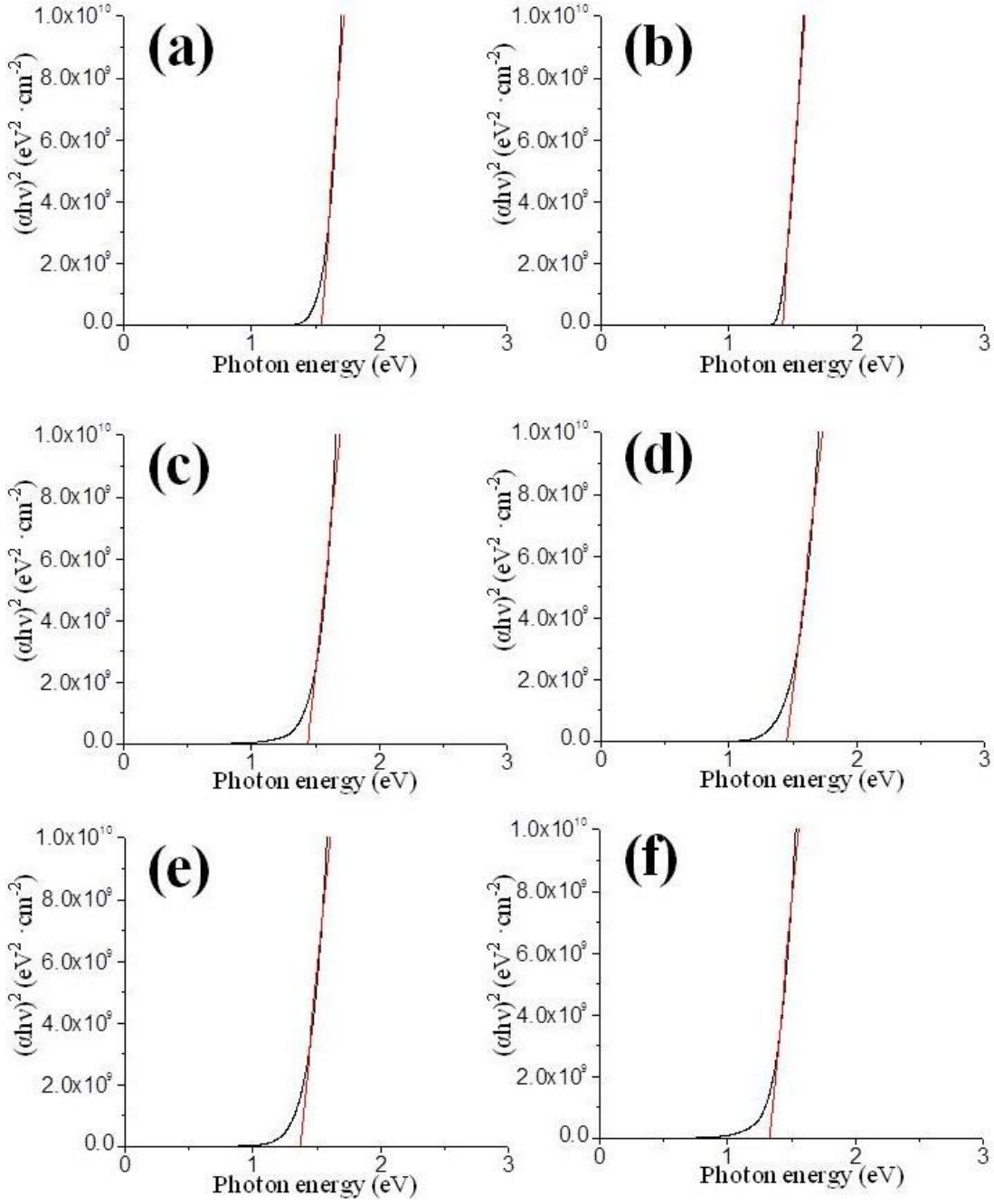

Figure 5-17. Plots of $(\alpha h\nu)^2$ Vs photon energy for the direct bandgap investigation SnS thin films. Red bold line for each graph is linearly fitted line. The graph (a) through (f) are matched to the sample A through F, respectively.

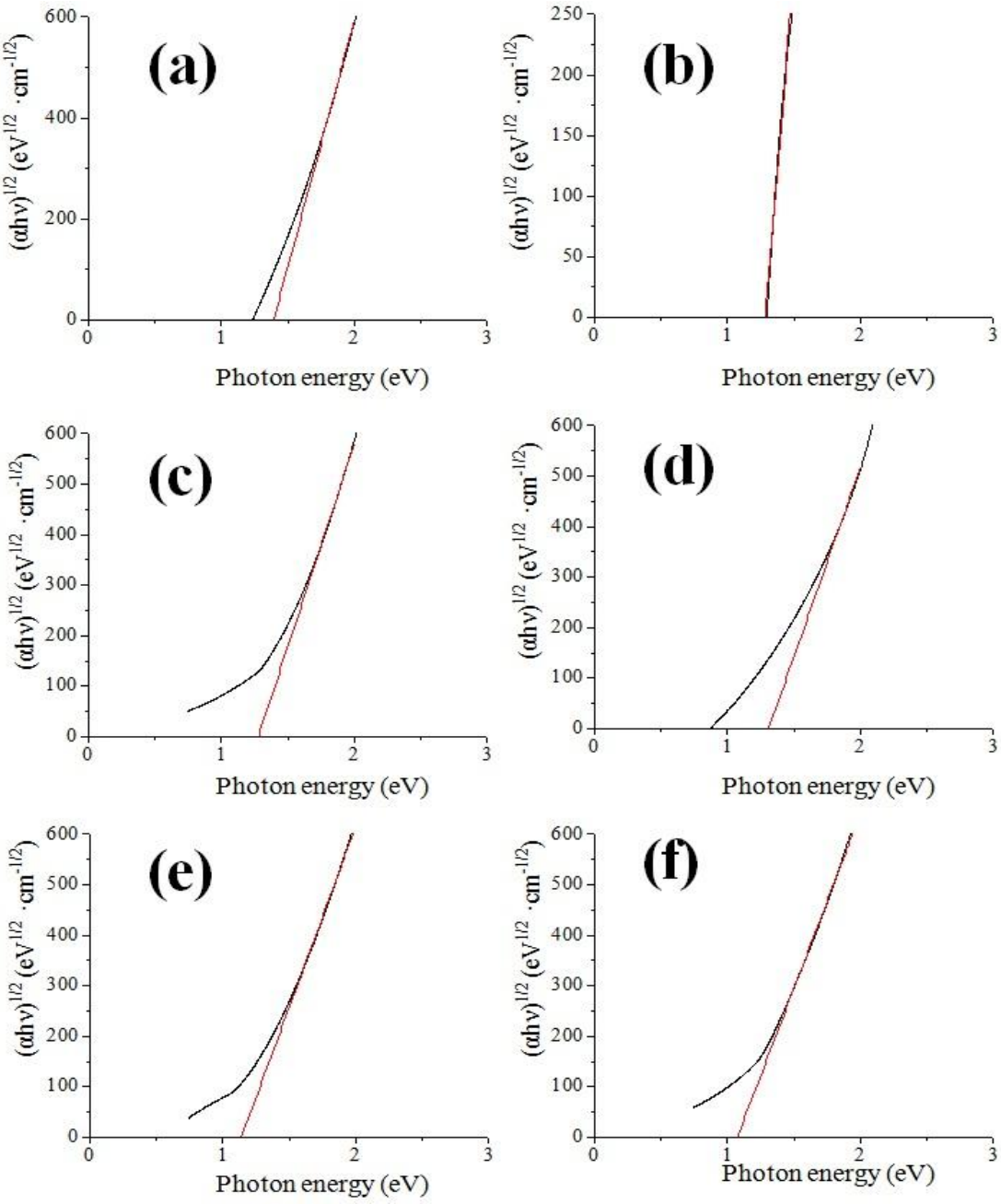

Figure 5-18. Plots of $(\alpha h\nu)^{1/2}$ Vs photon energy for the indirect bandgap investigation of SnS thin films. Red bold line for each graph is linearly fitted line. The graph (a) through (f) are matched to the sample A through F, respectively.

Sample Name	Direct bandgap (eV)	Indirect bandgap (eV)
A	1.55	1.39
B	1.39	N/A
C	1.44	1.28
D	1.46	1.31
E	1.37	1.16
F	1.33	1.07

Table 5-6. Direct and indirect bandgap of SnS thin films. N/A means “not applicable.”

5.4.3 Electrical Properties of SnS Thin Film by Radio-frequency Magnetron Sputter

Electrical properties of SnS thin films were investigated for the set of SnS thin film samples from Table 5-5. These electrical properties of the films were evaluated by using transfer length measurement (TLM). TLM is one of the convenient ways to determine electrical properties of the films. The electrical properties that can be discovered by TLM include sheet resistance, contact resistance and resistivity. The most essential goal of this measurement here is to determine the metals that can make an ohmic contact to SnS. This is because making ohmic contact to SnS is the first and crucial step for other electrical characterization of thin films and device fabrication. The size and shape of pattern used here for TLM is shown in Figure 5-19. Several metals have been reported as possible ohmic contact metals to SnS materials. Indium is the most common materials used for ohmic contact to SnS [15, 26, 33, 36, 37]. Moreover, Al, Sn

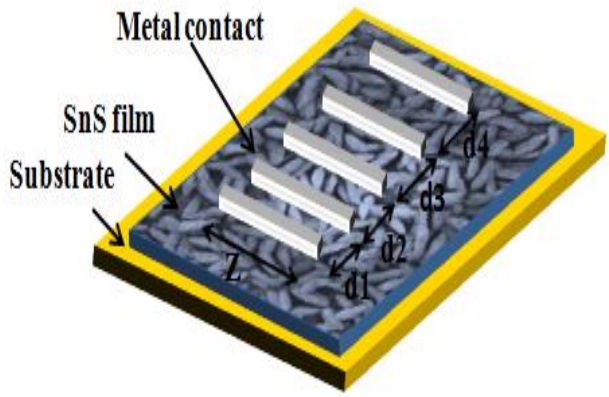

Figure 5-19. Pattern of transfer length method for SnS films (d1: 200 μm, d2: 300 μm, d3: 500 μm d4: 700 μm and Z: 6 mm). d denotes the distance between two metal bars and Z is the lengh of the metal bar.

and Ag are reported as promising materials for metal contact of SnS when accompanied with thermal treatment [33, 37].

Figure 5-20 show the results by TLM from the SnS film prepared with 155 W at 10 mTorr in 12 cm throw distance. The metal used here was a 100-nm-thick indium contact that was prepared with a shadow mask by thermal evaporation. As shown in Figure 5-19 and 5-20, four measurements were done for each sample with five metal bar contacts. The TLM has four different distances between two bars to measure I-V curve: 200 μm, 300 μm, 500 μm and 700 μm. To determine the ohmic contact, the linearity of I-V curve at each measurement is required first and the total resistances calculated from I-V curves should show the linearity again in terms of distance. The linearity can be evaluated by the square of correlation coefficient, r^2 and $r^2 = 1$ is the ideal ohmic contact [32]. The prepared SnS film in

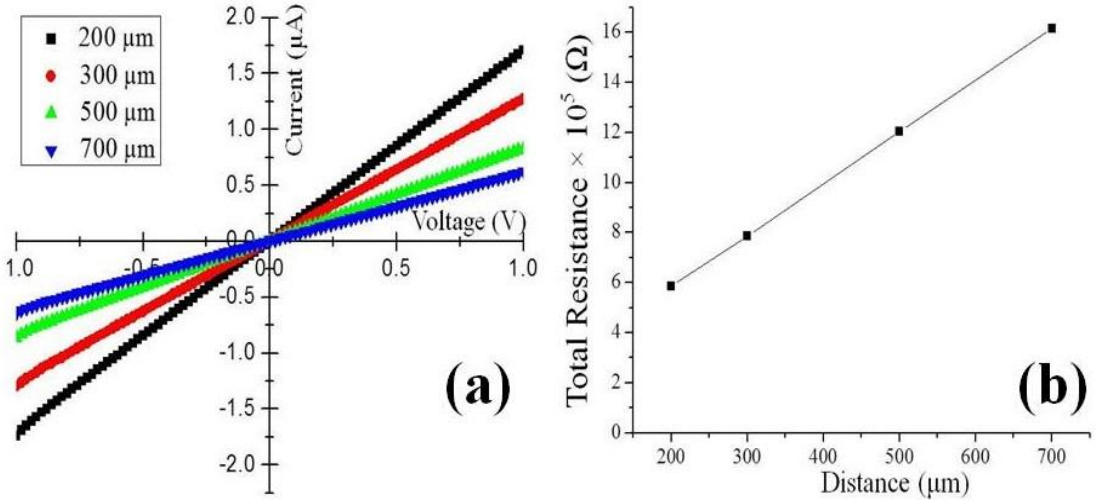

Figure 5-20. Transfer length method for SnS films: (a) I-V characteristics depending on various distances (b) Total resistance in terms of distance. Fitted curve (black solid line) was expressed as Y= 2061x + 172528. The SnS films used here were deposited at 155 W and 10 mTorr for 10 min at a 12 cm throw distance and In contact was used.

Figure 5-20 exhibits linearity with In contact in I-V curve and total resistance plot in terms of distance (r^2 =1). This indicates indium contact make ohmic contact to SnS. By using linear fitting, the sheet resistance and contact resistance were determined from the gradient of the graph in Figure 5-20 (b) with film thickness. The sheet resistance and contact resistance are 2.1 x 10^3 Ω/□ and 1.7 x 10^5 Ω, respectively. Resistivity of the film was 471 Ω·cm, which is extracted using the film thickness from 5-20 (b).

Figure 5-21 shows results from TLM patterns on SnS films with In contact. All samples exhibit linearity in the I-V curve indicating an ohmic contact between SnS and In metal contact (see Figure 5-21 (a) and (c)). No trend in total resistance in terms of deposition pressure can be found because of film thickness variations as shown in Figure 5-15. However, interesting points in this experiment were found in results of RMS roughness and resistivity as show in Figure 5-21 (b) and (d). Figure 5-21 (b) and (d) show the resistivity and RMS roughness in terms of

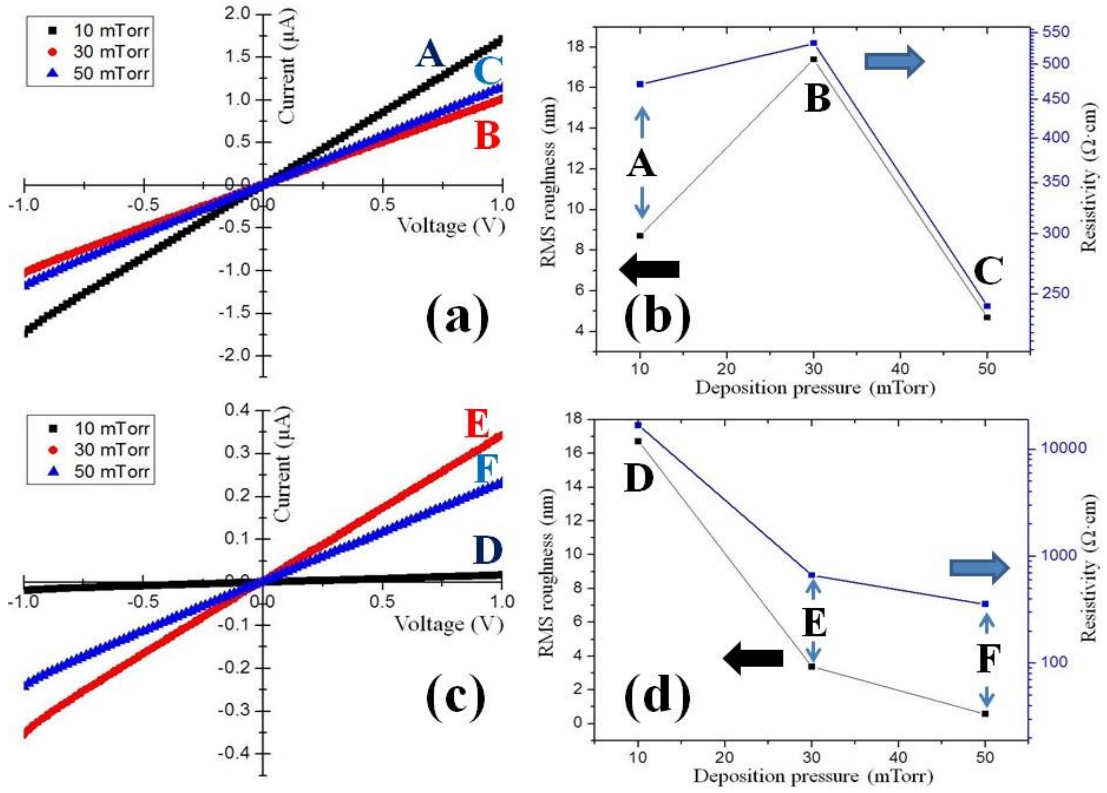

Figure 5-21. SnS films deposited at varied deposition pressure and throw distance with In contact: (a) I-V characteristics of SnS fims prepared in 12 cm throw distance measured at 200 μm transfer length (b) Root mean square roughness and resistivity of SnS films prepared in 12 cm (c) I-V characteristics of SnS fims prepared in 17 cm throw distance measured at 200 μm transfer length (d) Root mean square roughness and resistivity of SnS films prepared in 17 cm.

deposition pressure and throw distance. The trend of the resistivity follows that of RMS roughness in Figure 5-21.

Highest and lowest points of RMS roughness correspond to highest and lowest points of resistivity. Considering SEM and AFM results on morphology in Chapter 5.4.1 and Figure 5-14 together, it is suspected that the samples with columnar and vertical structure such as sample B and D have higher RMS roughness and highest resistivity (B: 17. 4 nm & 533 Ω·cm, D: 16.7 nm & 1.68 $\times 10^4$ Ω·cm, respectively) while the samples with denser morphology such as C and F

have a lower RMS roughness and resistivity (C: 4.69 nm & 241 Ω·cm, F: 0.577 nm & 358 Ω·cm, respectively). Since TLM is in the lateral direction, it is possible that there is a longer carrier pathway in case of porous and columnar structure films. With this range of resistivity, the majority carrier mobility, μ can be estimated, by following the equation below,

$$\rho = \frac{1}{e\mu n_s} \tag{5.12}$$

where ρ is the resistivity and n_s is the carrier concentration. The carrier concentration that has been reported for SnS films is the range of 10^{15}-10^{16} cm^{-3}[4, 11, 16]. Then, if one assumes 5×10^{15} cm^{-3} as the carrier concentration, the mobility can be estimated with the range of 0.07-5.19 $cm^2/V\cdot s$.

Other metals, Al, Ti and Pt were deposited to investigate another candidate for SnS contact materials as shown in Figure 5-22 (a)-(c). Yet, the I-V curve does not show good linearity in the curve and, thus, the resulting currents are in the range of few tens of nanoamperes. Indium is the excellent material to make an energetically favorable for ohmic contact to SnS but the low

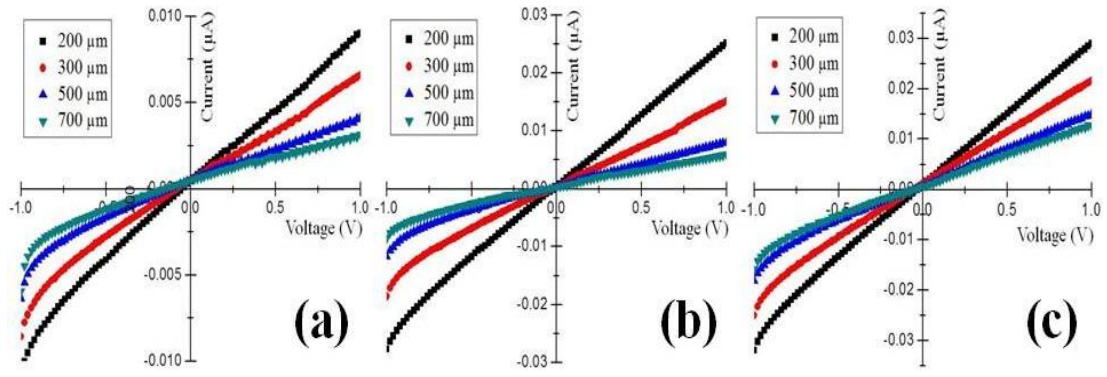

Figure 5-22. I-V characteristics of SnS films with various metal contacts: (a) Al contact (b) Ti contact (c) Pt contact.

melting temperature of indium (~157 ℃) limits the availability in high temperature process such as annealing and high-energy deposition. Further study on other possible metal contacts or techniques to make ohmic contact is necessary.

The photoresponse was also investigated with a set of SnS films as shown in Figure 5-23. In this measurement, SnS thin films deposited with 155 W power at 12 cm throw distance are evaluated at varying deposition pressures; these are the A, B and C samples in Table 5-5. The experiment was carried out under dark condition and AM 1.5 illumination (100 mW/cm^2) with indium TLM pattern as shown in Figure 5-18. The conductivity, σ was obtained via general expression for conductivity, or resistivity below,

$$\sigma = \frac{1}{\rho} = \frac{L_c}{RWt} \tag{5.13}$$

where R is the total resistance, W is the width of metal contact, L_c is the distance between two metal contacts and t is the film thickness. In this measurement, W was 300 and L_c is 300 μm. Due to inherent high resistivity, the dark conductivity, σ_d calculated from the equation (5.13) is low: (a) 5.53×10^{-5} $\Omega^{-1}\cdot cm^{-1}$, (b) 3.33×10^{-5} $\Omega^{-1}\cdot cm^{-1}$ and (c) 2.01×10^{-4} $\Omega^{-1}\cdot cm^{-1}$ in Figure 5-22. Calculated photoconductivity, σ_{ph} in the same manner exhibits only small difference in the magnitude and the ratio of σ_{ph} to σ_d are 1.21, 1.23 and ~1 for Figure 5-23 (a), (b), and (c), respectively. This is the evidence that the SnS thin films absorb the light energy and transports generated carrier under applied bias. The interesting finding is shown in Figure 5-23 (c). The σ_{ph}/σ_d is ~1 for the SnS thin film deposited under 50 mTorr in spite of higher σ_d. Obviously, the sample C has capability to absorb the light energy efficiently as shown in Figure 5-16 but the results mean that no photogenerated carrier transport is occurring in the Sample C for this particular lateral measurement. The reasons can be surmised that either no carrier generation has occurred in the Sample C or the carrier transport is affected by lots of defects. The former is not plausible

because Sample C also has been determined and its bandgap and the simulator illuminates Sample C with the wavelengths that give higher energy than that of the bandgap. The latter is more possible since the Sample C was deposited with higher deposition pressure- that is, lower energy deposition. SnS thin films prepared in higher deposition pressure include lower crystallinity by lower energy deposition and the crystallites that exist in the SnS films are very small as mentioned in Chapter 5.4.1. Hence, lots of crystallite interfaces can lead lots of defects in the film and, thereby, the generated carriers can be consumed by trap states that are generated by the defects.

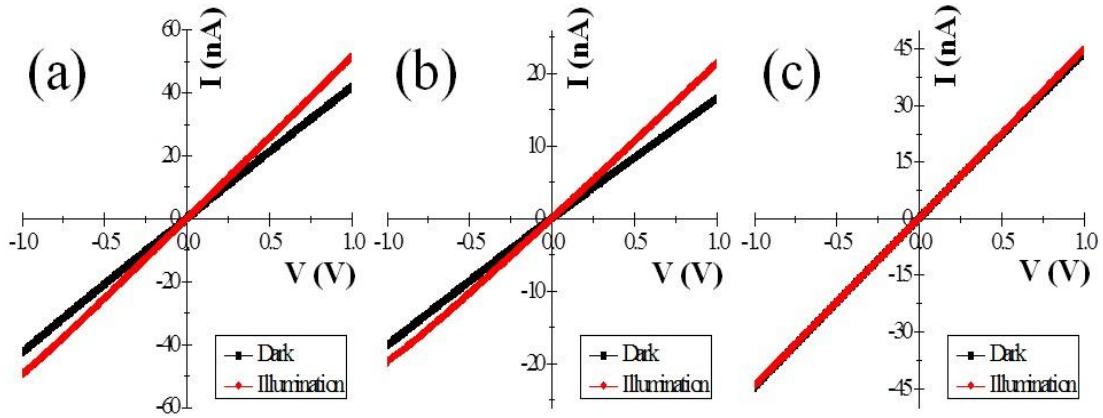

Figure 5-23. Photoresponse of SnS thin films with indium metal contacts. The SnS thin films are deposited with 155 W at 12 cm throw distance under (a) 10 mTorr (b) 30 mTorr (c) 50 mTorr. I and V represent current and voltage, respectively. Black and red bold lines represent the I-V curve measured under dark condition and under AM 1.5 illumination, respectively.

5.4.4 Fabrication of SnS Thin Film Solar Cells

SnS thin films deposited by RF sputtering have been used to make solar cells in two different configurations. The first attempt was carried out using ZnO thin films to form a heterostructure, similar to the device simulation done by AMPS-1D. For the device fabrication,

~200 nm thick SnS thin film was prepared with 155 W of power at 17 cm throw distance under 10 mTorr in deposition pressure. This was deposited on a 100-nm-thick film of n-type Al doped-ZnO that was deposited by plasma enhanced atomic layer deposition from Dr. Jackson's group. A 100-nm-thick aluminum metal contact- which is considered as a promising ohmic contact material to SnS at that time,- deposited onto the SnS thin films through electron beam evaporation. Figure 5-24 (a) show the I-V curve obtained from the SnS/ZnO heterojunction thin film solar cells under AM 1.5 illumination. As in the experiment from Chapter 5.4.3, photoresponse was indentified in the range of higher voltage area but the structure has no open circuit voltage and, thereby, no photocurrent in the lower voltage region. This implies that SnS/ZnO heterojunction has unfavorable band alignment to establish internal electric field within the structure as reported by Sinsermsuksakui et al. [31]. Investigations on energy band diagram model for sputtered SnS thin films and band-offset engineering based on that is necessary for further research on this type of SnS thin film solar cells. The lack of photoresponse could also be due to several other factors, including high surface recombination on the very columnar SnS or poor electrical contacts to the

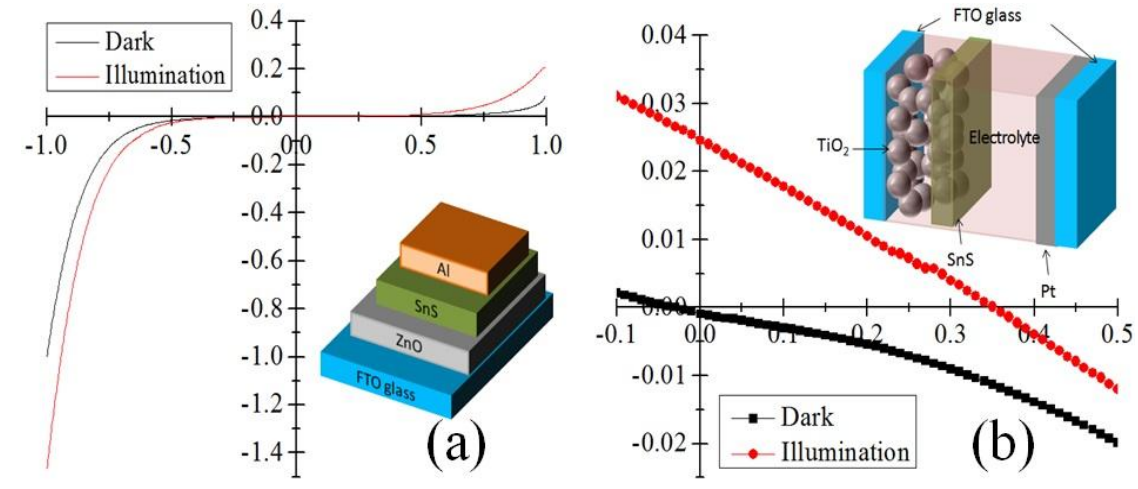

Figure 5-24. SnS thin films solar cells: (a) FTO/AZO (100 nm)/SnS (200 nm)/Al (100 nm) solar cells (b) FTO/TiO_2 (6 μm)/SnS (30 nm)/liquid electrolyte/Pt (40 nm) electrochemical solar cells.

heterostructure.

Another attempt to use SnS in a solar cell configuration was to implement it in a type of electrochemical cell. As shown in Figure 5-24 (b), TiO_2 films were obtained from a commercial TiO_2 paste (DSL 18 NR-T, Dyesol) by the doctor blade technique described previously. After annealing at 450 ℃ for 30 min, a 6-μm-thick TiO_2 film was obtained. A SnS thin film was deposited with 155 W power at 12 cm throw distance under 10 mTorr pressure. A 40-nm-thick Pt counter electrode was prepared by electron beam evaporation. To make a cell, ~40-μm-thick parafilm was used as a spacer and the commercial liquid electrolyte (EL-HPE, Dyesol) was injected between the TiO_2/SnS electrode and the Pt counter electrode. This SnS electrochemical cell shows 0.025 mA/cm^2 of short circuit current, 350 mV of open circuit voltage, and a fill factor of 0.251. The resulting conversion efficiency is 0.0022 %. Photocurrent can be extracted from the solar cells owing to existence of V_{oc}, although the magnitude is too small, even with the comparison with previous SnS electrochemical solar cells [30]. Moreover, 350 mV of the open circuit voltage is relatively smaller than that in the solar cells by Wang et al. or conventional DSSCs which have similar structure [44]. This is believed to result from a low concentration of carrier injection since the open circuit voltage from this structure is obtained from the difference between Fermi level of TiO_2 and redox level of the electrolyte. As in Figure 5-24 (a), it is speculated that unfavorable TiO_2/SnS junction is one of reason for the low current density. In addition to this, long carrier path length due 8μm thick TiO_2 film may have an influence on the conversion efficiency.

Figure 5-25 (a) and (b) shows SEM pictures of sputtered SnS thin films at normal angle and the films that are sculptured with 5° of obliquely incident vapor flux on TiO_2 colloidal thin film. For this time experiment, a relatively thin TiO_2 film (~3 μm) was used to reduce the effect of a long carrier path length. The deposited SnS STFs show a highly ordered columnar structure in Figure 5-25 (b). A solar cell was prepared in the same way as described for that of Fig 5-24 (b).

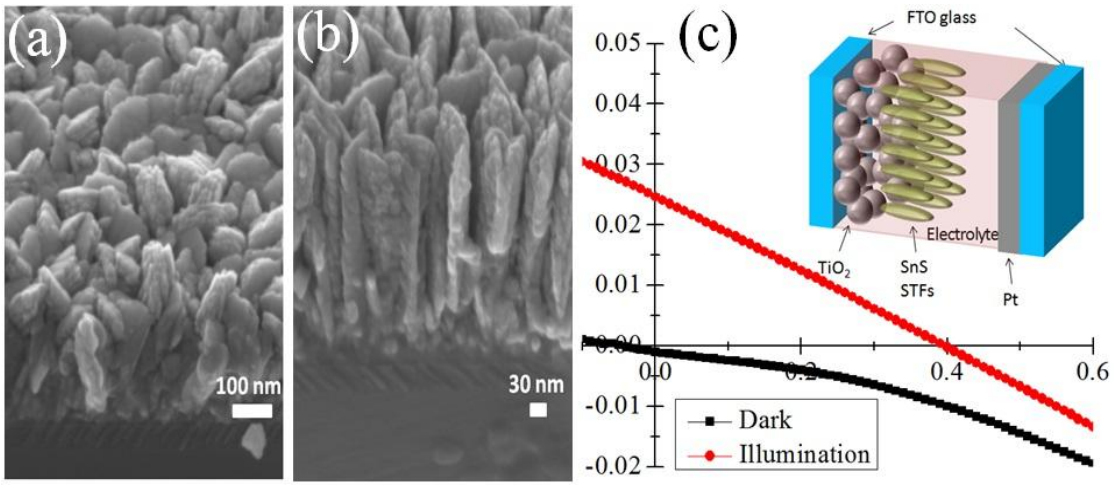

Figure 5-25. Sculptured SnS thin films and electrochemical cells: (a) surface morphology of non- sculptured SnS thin films (b) surface morphology of sculptured SnS thin films by 5° obliquely incident vapor flux (c) I-V curve for SnS electrochemical solar cells incorporating sculptured SnS thin films. I and V in Figure 5-22 denotes current and voltage, respectively. The inset in Figure 5.24 (c) show the schematic of SnS electrochemical cells consisting TiO_2 (3 μm)/SnS (200 nm)/liquid electrolyte/Pt(40 nm).

Small increases in open circuit voltage and fill factor are measured (V_{oc}= 0.38, FF=0.26), respectively in Figure 5-25 (c). It seems that improved series resistance is resulted by the reduced thickness of the TiO_2 film and, in particular, enhanced V_{oc} is resulted from more injected carrier from SnS to TiO_2 since V_{oc} is determined by the difference between Fermi level of TiO_2 and redox potential of electrolyte in this system [51]. Therefore, we believe that the highly ordered columnar structures lead to improved conversion efficiency, 0.0025 % due to structural features of STFs.

5.5 Summary

SnS thin films were deposited by RF magnetron sputtering under variation of deposition parameters, including deposition power, deposition pressure and deposition time, throw distance and substrate heating temperature. Almost all of the grown SnS films exhibited herzenbergite crystal structure. Applied deposition power was one of factors to obtain the change in growth orientations in SnS thin films. Surface morphology of SnS film deposited varied in deposition modes from columnar and porous structure to dense film with small crystallites. The deposition pressure had a large influence on formation of specific surface morphology. Shorter throw distance and substrate heating also contributed to additional growth orientation. The possibility on the inclusion of secondary phases and existence of various lattice parameters were discussed according to deposition mode and found that is remarkable in higher energy deposition.

All these changes in surface morphology and crystal structure can be somewhat correlated to the energy arriving at the substrate based on the mean free path and mean speed of vapor flux. Also, it was found that deposition rate is related to the diffused vapor flux.

Optical properties of the SnS films were investigated by spectroscopic ellipsometry and Tauc equation. The measured absorption coefficient was more than 10^4 cm^{-1} even in the range of >1000 nm wavelength. Less crystallized SnS films exhibited broader absorption wavelength and higher absorption coefficient. The direct bandgap and indirect bandgap of SnS thin films was calculated and ranged from 1.33 to 1.55 eV and from 1.07 to 1.39 eV, respectively. The SnS thin films prepared under lower energy deposition exhibited a higher possibility of existence of Urbach tails and trap states within their bandgaps.

In examining the electrical properties of SnS films by the transfer length method, indium was found to make ohmic contact to sputtered SnS films. It was found that the measured

resistivity of the SnS films is related to their surface morphology. The SnS films with lower root mean square roughness exhibited lower resistivity while more structured SnS film showed higher resistivity. Estimated mobility varied from 0.07 to 5.19 $cm^2/V \cdot s$. Photoresponse was observed in the SnS films deposited under lower pressure. The ratios of photoconductivity to dark conductivity were 1.21 and 1.23 while SnS thin films with higher deposition pressure showed no photoresponse, indicating the existence of trap states.

Solar cells with SnS thin film were fabricated in two different types. Improved photocurrent was observed in higher voltage area but no open circuit voltage measured for SnS thin film solar cells. In electrochemical SnS thin film solar cells, 0.025 mA/cm^2 of short circuit current, 350 mV of open circuit voltage, 0.251 of fill factor were measured. When the SnS STF were incorporated, enhancement in open circuit voltage, fill factor and efficiency are observed (V_{oc}= 0.38, FF=0.26 and η=0.0025 %=) owing to structural features of STFs. For more efficient solar cells incorporating SnS thin films, it seems that deeper understanding on SnS materials themselves is necessary, including work function, electron affinity or defect levels. At the same time, investigating the proper candidate of n-type semiconductor materials is also important.

5.6 Chapter 5 Reference

[1] A. L. Rogach, A. Eychmüller, S. G. Hickey, S. W. Kershaw, Infrared-emitting colloidal nanocrystals: synthesis, assembly, spectroscopy, and application, *Small* Vol. 3 No. 4 (**2007**) 536-557.

[2] J. Gao, C. L. Perkins, J. M. Luther, M. C. Hanna, H. Chen, O. E. Semonin, A. J. Nozik, R. J. Ellingson, M. C. Beard, n-type transition metal oxide as a hole extraction layer in PbS quantum dot solar cells, *Nano Letters* Vol. 11 (**2011**) 3263-3266.

[3] K. S. Leschkies, T. J. Beatty, M. S. Kang, D. J. Norris, E. S. Aydil, Solar cells based on junctions between colloidal PbSe nanocrystals and thin ZnO films, *ACS Nano* vol. 3 No. 11 (**2009**) 3638-3648.

[4] H. Noguchi, A. Setiyadi, H. Tanamura, T. Nagatomo, O. Omoto, Characterization of vacuum-evaporated tin sulfide film for solar cell materials, *Solar Energy Materials and Solar Cells* vol. 35 (**1994**) 325-331.

[5] M. Parenteau, C. Carlone, Influence of temperature and pressure on the electronic transitions in SnS and SnSe semiconductors, *Phycal Review B* Vol. 41 No. 8 (**1990**) 5227-5234.

[6] J. B. Johnson, H. Jones, B. S. Latham, J. D. Parker, R. D. Engelken, C. Barber, Optimization of photoconductivity in vacuum-evaporated tin sulfide thin films, *Semiconductor Science and Technology* Vol. 14 (**1999**) 501-507.

[7] S. C. Ray, M. K. Karanjai, D. DasGupta, Structure and photoconductive properties of dip-deposited SnS and SnS_2 thin films and their conversion to tin dioxide by annealing in air, *Thin Solid Films* Vol. 350 (**1999**) 72-78.

[8] M. Devika, N. Koteeswara Reddy, K. Ramesh, K. R. Gunasekhar, E. S. R. Gopal, K. T. Ramakrishna Reddy, Influence of annealing on physical properties of evaporated SnS films, *Semiconductor Science and Technology* Vol. 21 (**2006**) 1125-1131.

[9] A. Tanuševski, D. Poelman, Optical and photoconductive properties of SnS thin films prepared by electron beam evaporation, *Solar Energy Materials & Solar Cells* Vol. 80 (**2003**) 297-303.

[10] K. Hartman, J. L. Johnson, M. I. Bertoni, D. Recht, M. J. Aziz, M. A. Scarpulla, T. Buonassisi, SnS thin-films by RF sputtering at room temperature, *Thin Solid Films* Vol. 519 (**2011**) 7421-7424.

[11] K.T. Ramakrishna Reddy, N. K. Reddy, R. W. Miles, Photovoltaic properties of SnS based solar cells, *Solar Energy Materials & Solar Cells* Vol. 90 (**2006**) 3041-3046.

[12] J. Y. Kim, S. M. George, Tin monosulfide thin films grown by atomic layer deposition using Tin 2,4-Pentanedionate and hydrogen sulfide, Proceeding of *the International Society for Optics and Photonics* Vol. 7769 No. 776907 (**2010**) 1-13.

[13] G. H. Yue, Y. D. Lin, X. Wen, L. S. Wang, Y. Z. Chen, D. L. Peng, Synthesis and characterization of the SnS nanowires via chemical vapor deposition, *Applied Physics A* Vol. 106 (**2012**) 87-91.

[14] A. Tanuševski, Optical and photoelectric properties of SnS thin films prepared by chemical bath deposition, *Semiconductor Science and Technology* Vol. 18 (**2003**) 501-505.

[15] M. Devika, N. Koteeswara Reddy, K. R. Gunasekhar, Structural, electrical, and properties of as-grown and heat treated ultra-thin SnS films, *Thin Solid Films* Vol. 520 (**2011**) 628-632.

[16] B. Ghosh, R. Bhattacharjee, P. Banerjee, S. Das, Structural and optoelectronic properties of vacuum evaporated SnS thin films annealed in argon ambient, *Applied Surface Science* Vol. 257 (**2011**) 3670-3676.

[17] Y. Guo, W. Shi, Y. Zhang, L. Wang, G. Wei, Influence of Substrate Temperature on Properties of Tin Sulfide Thin Films in Proceedings of *SPIE* Vol. 6984 (**2008**) 69841P.

[18] S. Zhang, S. Cheng, Thermally evaporated SnS:Cu thin films for solar cells, *Micro & Nano Letters* Vol. 6 (**2011**) 559-562.

[19] S. A. Bashkirov, V. F. Gremenok, V. A. Ivanov, Physical Properties of SnS Thin Films Fabricated by Hot Wall Deposition, *Semiconductors* Vol. 45 No. 6 (**2010**) 749-762.

[20] A. Stadler, H. Schimper, U. Brendel, D. Topa, A. Basch, H. Dittrich, Analyzing UV/Vis/NIR spectra with the single-layer model—Sputtered SnS thin films I: Space–time dependencies, *Thin Solid Films* Vol. 519 (**2011**) 7951-7958.

[21] A. Stadler, H. Dittrich, Analysing UV/Vis/NIR spectra with the double-layer model — Sputtered SnS thin-films II: Gas law and plasma parameter dependencies, *Thin Solid Films* Vol. 519 (**2011**) 6568-6578.

[22] M. Ristov, G. Sinadinovski, M. Mitreski, M. Ristova, Photovoltaic cells based on chemically deposited p-type SnS, *Solar Energy Materials & Solar Cells* Vol. 69 (**2001**) 17-24.

[23] O. E. Ogah, K. Ramakrishna Reddy, G. Zoppi, I. Forbes, R. W. Miles, Annealing studies and electrical properties of SnS-based solar cells, *Thin Solid Films* Vol. 519 (**2011**) 7425-7428.

[24] M. Sugiyama, K.T. Ramakrishna Reddy, N. Revathi, Y. Shimamoto, Y. Murata, Band offset of SnS solar cell structure measured by X-ray photoelectron spectroscopy, *Thin Solid Films* Vol. 519 (**2011**) 7429-7431.

[25] F. Jiang, H. Shen, W. Wang L. Zhang, Preparation of SnS Film by Sulfurization and SnS/a-Si Heterojunction Solar Cells, *Journal of the Electrochemical Society* Vol. 159 (**2012**) H235-H238.

[26] B. Ghosh, M. Das, P. Banerjee, S. Das, Fabrication of the SnS/ZnO heterojunction for PV applications using electrodeposited ZnO films, *Semiconductor Science and Technology* Vol. 24 (**2009**) 025024-1-025024-7.

[27] G. Yue, Y. Lin, X. Wen, L. Wang, D. Peng, SnS homojunction nanowire-based solar cells, *Journal of Materials Chemistry* Vol. 22 (**2012**) 16437-16441.

[28] M. Gunasekaran, M. Ichimura, Photovoltaic cells based on pulsed electrochemically deposited SnS and photochemically deposited US and Cd1-xZnxS, *Solar Energy Materials and Solar Cells* Vol. 91 (**2007**) 774.

[29] D. Avellaneda, G. Delgado, M.T.S. Nair, P.K. Nair, Structural and chemical transformations in SnS thin films used in chemically deposited photovoltaic cells, *Thin Solid Films* Vol. 515 (**2007**) 5771-5776.

[30] Y. Wang, H. Gong, B. Fan, G. Hu, Photovoltaic behavior of nanocrystalline SnS/TiO_2, *Journal Physical Chemistry C* Vol. 114 (**2010**) 3256-3259.

[31] P. Sinsermsuksakul, K. Hartman, S. B. Kim, J. Heo, L. Sun, Enhancing the efficiency of SnS solar cells via band-offset with a zinc oxysulfide buffer layer, *Applied Physics Letters* Vol. 102 (**2013**) 053901-1-053901-5.

[32] M. Devika, N. Koteeswara Reddy, F. Patolsky, K. R. Gunasekhr. Ohmic contacts to SnS films: selection and estimation of thermal stability, *Journal of Applied Physics* Vol. 104 (**2008**) 124503-1-124503-6.

[33] T. H. Sajeesh, K. B. Jinesh, M. Rao, C S. Jartha, K. P. Vijayakumar, Defect levels in SnS thin films prepared using chemical spray pyrolysis, *Physica Status Solidi A* Vol. 209 (**2012**) 1274-1278.

[34] J. J. Loferski, Theoretical considerations governing the choice of the optimum semiconductor for photovoltaic solar energy conversion, *Journal of Applied Physics* Vol. 27 (**1956**) 777-784.

[35] M. Ichimura, H. Takagi, Electrodeposited ZnO/SnS heterostructures for solar cell application, *Japanese Journal of Applied Physics*, Vol. 47 No. 10 (**2008**) 7845-7847.

[36] B. Gosh, M. Das, P. Banerjee, S. Das, Characteristics of metal/p-SnS schottky barrier with and without post-deposition annealing, *Solid State Sciences* Vol. 11 (**2009**) 461-466.

[37] C. Chen, I. An, G. M. Ferreira, N. J. Podraza, J. A. Zapien, R. W. Collins, Multichannel Muller matrix ellipsometer based on the dual rotating compensator principle, *Thin Solid Films* Vol. 455 May (**2004**) 14-23.

[38] R. E. Banai, H. Lee, M. A. Motyka, R. Chandrasekharan, N. J. Podraza, J. R. S. Brownson, M. W. Horn, Optical properties of sputtered SnS thin films for photovoltaic absorbers, *IEEE Journal of Photovoltaics* Vol. 3 No. 3 July (**2013**) 1084-1089.

[39] H. Nozaki, M. Onoda, M. Sekita, K. Kosuda, T. Wada, Variation of lattice dimensions in epitaxial SnS films on MgO(001), *Journal of Solid State Chemistry* Vol. 178 (**2005**) 245-252.

[40] R. E. Banai, H. Lee, S. Zlotnikov, J. R. S. Brownson, M. W. Horn, Phase identification of RF-sputtered SnS thin films using rietveld analysis of x-ray diffraction patterns, *39th IEEE Photovoltaic Specialists Conference* (**2013**).

[41] D. L. Smith, Thin-film deposition: principles & practice *McGraw-Hill* (**1995**).

[42] L. A. Burton, A. Walsh, Phase stability of the earth abundant tin sulfides SnS. SnS_2 and Sn_2S_3, *The Journal of Physical Chemistry*. Vol. 116 (**2012**) 24262-24267.

[43] J. Nelson, The physics of solar cells, *Imperial College Press* London (**2003**).

[44] M. Grätzel, Solar energy conversion by dye-sensitized photovoltaic cells, *Inorganic Chemistry* Vol. 44 No. 20 (**2005**) 6841-6851.

[45] M. Devika, K. T. Ramakrishna Reddy, N. Koteeswara Reddy, K. Raesh, R. Ganesan, Microstructure dependent physical properties of evaporated tin sulfide films, *Journal of Applied Physics* Vol. 100 (**2006**) 023518-1-023518-7.

[46] R. Chandrasekharan, Numerical modeling of tin-based absorber devices for cost-effective solar photovoltaics, *Ph. D Dissertation*, the Pennsylvania State University, University Park, PA, USA(**2012**).

[47] R. E. Banai, H. Lee, M. Lewinsohn, M. A. Motyka, ,R. Channdraskharan, N. J. Podaraza, J. R. S. Brownson, M. W. Horn, Investigation of the absorption properties of sputtered tin sulfide thin films for photovoltaic applications, *38^{h} IEEE Photovoltaic Specialists Conference* (**2012**) 000164-000169.

[48] J. R. Welty, C. E. Wicks, R. E. Wilson, G. L. Rorrer, Fundamentals of momentum, heat, and mass transfer 5th edition, John Wiley & Sons, Inc. (**2008**).

[49] S. Lopez, A. Ortiz, Spray pyrolysis deposition of Sn_xS_y thin films, *Semiconductor Science and Technology* Vol. 9 (**1994**) 2130-2133.

[50] S. J. Fonash et al. http://www.ampsmodeling.org/.

[51] M. Grätzel, Solar energy conversion by dye-sensitized photovoltaic cells, *Inorganic Chemistry* Vol. 44 No. 20 (**2005**) 6841-6851.

Chapter 6

Conclusion and Future work

6.1 Conclusion

In this dissertation, three different applications for light energy utilization were researched and fabricated: dye-sensitized solar cells incorporating sculptured platinum thin films as a counter electrode, TiO_2 photocatalytic films with sculptured copper film as a cocatalyst and SnS for use in thin film solar cells. For each section, a bulleted list of the conclusions reached in this dissertation is provided below. For a discussion of these conclusions, see each section discussion as listed.

6.1.1 Sculptured Platinum Nanowire Counter Electrodes for Dye-sensitized Solar Cells (Chapter 3)

- Sculptured platinum nanowire thin films were fabricated by 5° incident vapor flux angle via electron beam evaporation.
- Sculptured Pt thin films exhibited higher roughness of 44.4 nm than other Pt films prepared as counter electrodes.
- H_2PtCl_6 solution treatment onto platinum thin films caused a decrease in surface roughness.

- Electrochemical analysis that was implemented in symmetrical cells showed that a lower charge transfer resistance of 0.121 Ω·㎠ was measured in the sculptured platinum nanowire counter electrode than that in planar platinum counter electrodes (0.578 Ω·㎠).
- Further improvement in the charge transfer resistance was measured for planar Pt electrode (0.578 Ω·㎠ → 0.509 Ω·㎠) and sculptured Pt counter electrode (0.121 Ω·㎠ →0.04025 Ω·㎠).
- Dye-sensitized solar cells incorporating sculptured platinum nanowire counter electrode exhibited 5.1 % and 5.64 % of conversion efficiency without H_2PtCl_6 solution treatment and without it, respectively, showing the increase in photocurrent density under AM 1.5 illumination compared to standard Pt counter electrodes.

6.1.2 Plasmonic Enhancement of CO_2 Conversion to Methane using Sculptured Copper Thin Films Grown Directly on TiO_2 (Chapter 4))

- Sculptured copper thin films were grown by 5° incident vapor flux angle directly on TiO_2 photocatalytic film for CO_2 conversion.
- Fabricated copper films showed porous and columnar surface morphology
- The length of Cu columnar structures was varied by controlling the deposition time. The measured lengths were ranged from 61 nm to 331 nm.

- Methane production rate had maximum number of 124.3 $ppm \cdot cm^{-2} \cdot h^{-1}$ in the TiO_2/Cu STFs phtocatalytic film at the 160 nm long Cu columnar structure. After that, the methane production rate decreased as the length increased.
- The plasmonic effect of sculptured Cu thin films was found at ~600nm in the absorbance spectra and other evidence was observed in 160 nm planar Cu film experiment.
- Totally oxidized Cu thin films exhibited nearly no contribution for CO_2 conversion to methane.
- The plasmonic effect seen for sculptured Cu thin films was the essential factor to explain the 160-fold increase in methane production rate in the comparison with TiO_2 photocatalytic sample without Cu STFs.

6.1.3 Tin Sulfide Thin Film Deposited by Radio Frequency Magnetron Sputter for Solar Cell Application (Chapter 5)

- SnS thin films were deposited by radio frequency magnetron sputtering as an absorber material for photovoltaics by changing deposition parameters such as deposition power, deposition pressure, throw distance and substrate temperature.
- Higher deposition power was favorable for more crystallized films due to higher energy imparted to the vapor flux.
- Deposition pressure played an essential role in the variation in surface morphology of SnS thin films. In lower pressure depositions (e.g., 10 mTorr), surface morphology of SnS films exhibited columnar structures and in higher pressures (e. g., 50 mTorr), SnS thin film became more compact.

- Inclusion of SnS polymorphs and resulting additional phases was seen in lower pressure depositions, showing more crystallization of the films.
- Larger size and different shape of grains were observed in shorter throw distance films (e.g., 6.5 cm) because of other growth orientations by the inclusion of another SnS polymorph as in lower deposition pressure films.
- Substrate heating affected surface morphology of SnS thin films and crystal structure with possible inclusion of SnS polymorphs and more crystallization.
- Variation in morphology and crystal growth pattern based on changed deposition parameters were explained by the mean free path and energy of diffusing vapor flux.
- All the SnS films exhibited $>10^5$ cm^{-1} of high absorption coefficient in visible range and even in near infrared range.
- Direct and indirect energy band gaps were calculated and ranged from 1.33 to 1.55 eV and from 1.07 to 1.39 eV, respectively. The SnS thin films prepared under lower energy deposition exhibited more possibility of the existence of Urbach tails and trap states within their bandgap.
- Transfer length measurements with Indium contacts deposited at room temperature made ohmic contact to most of the sputter deposited SnS thin films.
- Resistivity measured by transfer length measurement showed a correlation to surface roughness. Lower root mean square roughness showed lower resistivity and vice versa.
- Photoresponse was found in the SnS thin film deposited under lower pressure while the SnS thin films prepared under higher deposition pressure showed no measurable photoresponse under AM 1.5 illumination in the TLM configuration.

- SnS thin film solar cells were fabricated in two ways: SnS thin film solar cell with ZnO thin film and SnS electrochemical cells with TiO_2 films.
- No open circuit voltage was found in SnS/ZnO thin film solar cells because of unfavorable band alignment
- SnS/TiO_2 electrochemical cells exhibited photovoltaic performance and with incorporation of sculptured SnS thin film, showed improvement in open circuit voltage and fill factor.

6.2 Future work

This chapter suggests ideas for future work that were based on the findings of this dissertation. Some specific experiment procedures are suggested while other suggestions while are for larger project level ideas.

6.2.1 Energy Band Diagram for Sputtered SnS Thin Films

In order to fabricate more efficient solar cells, unique properties of the sputtered SnS thin films should be investigated further. In particular, investigating energy band diagram including electron affinity, work function, carrier concentration and trap states is very important since this will help to design solar cells with other semiconductor materials and metals. Moreover, this can provide a strategy for efficient solar cells based on more understanding about band alignment and resulting possible mechanism.

The practical ways that I suggest for obtaining proper band diagram model are to use Kelvin probe force microscopy (KPFM) and Hall measurement. Since the material

characterization lab at Penn State already have the capability for KPFM, the work function of sputtered SnS thin films can be obtained by the relationship between the measured local surface potential difference, ΔSP and the work function of the sample, φ_s below [1],

$$\Delta SP = (\varphi_{tip} - \varphi_s) / e \tag{6.1}$$

Where φ_{tip} is the work function of the conductive tip and e is the magnitude of the electronic charge. In addition, Hall measurements can contribute to modeling the band diagram of the sputtered SnS thin films. This measurement is available on campus at the Applied Research Laboratory. Simply, Van der Pauw Hall measurement patterns can be tried as shown in Figure 6-1. Since the deposited SnS thin films have large sheet resistance (>10^7 Ω), micro size hall measurement pattern is necessary which and must be designed by photolithography. Photolithography can be carried out with a base etchant such as a NaOH solution. However, the study on etching rate with a specific etchant should be done first to obtain good definition of the Hall measurement pattern. From the measurement, many valuable parameters can be extracted such as type of the semiconductor and majority carrier concentration. The electron affinity can be

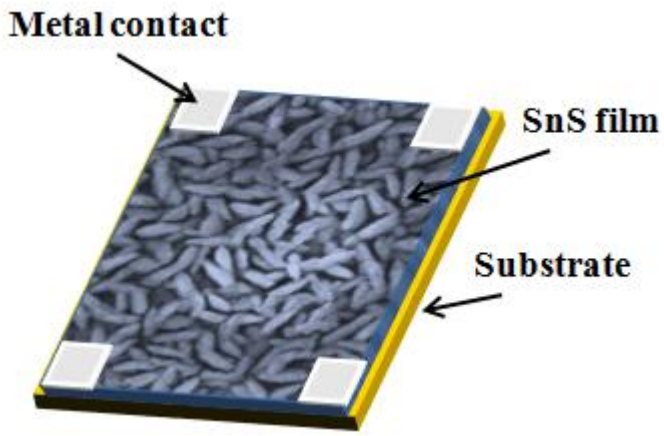

Figure 6-1. An example of hall measurement pattern. The figure shows van der Pauw pattern.

calculated from the combination of the results from KPFM and hall measurement. The band gap can be investigated with spectroscopic ellipsometry as shown in Chapter 5.4.2. Moreover, temperature dependent photoluminescence can be used to determine the trap levels within the band gap.

6.2.2 Further Research on Sputtered SnS Thin Films and Fabrication of Thin Film Solar Cells

Up to now, we found out many notable features of sputtered SnS thin films. For example, it is found that the surface morphology and crystallinity of the SnS thin films are related to energy of deposition mode. Optical and electrical properties were investigated in Chapter 5. However, the SnS thin films could not be optimized for thin film solar cells because room temperature deposition that was presented in this thesis did not show exceptional electrical properties. That is to say, higher energy deposition led higher deposition rate and higher crystallinity but it had secondary phases and higher resistivity. In lower energy deposition, the films showed lower possibility of secondary phase existence and lower resistivity but lower crystallinity and lower deposition rate. Therefore, simple adjustment based on deposition parameters at room temperature appears to have some limitations for further improvement.

The suggestion that can be easily made is to add additional source of energy for SnS thin films. For example, like in the experiment with substrate heater from Chapter 5.4.1, the additional energy can be provided during deposition or the films can be annealed in vacuum after deposition. Both cases can lead some changes in crystallinity and surface morphology of the SnS thin films. These changes will affect their optical and electrical properties in addition to the varied properties of SnS thin films depending on varied deposition parameters. In reality, several SnS thin film researches have been done for annealing [2-4] and substrate heating [5] under different deposition

systems. These additional sources of energy during or after deposition occur change in material, optical and electrical properties. So, annealing or substrate heating for SnS thin films by RF magnetron sputter could be the way to find desirable thin films that have advantages in material, optical and electrical properties for more efficient solar cells. For this idea, fundamental research like in Chapter 5.4 is necessary.

Another future work that can be suggested is the fabrication of Schottky barrier SnS thin film solar cells. As shown in Chapter 5.4.4, the efficiency was too low or not measurable although we could demonstrate the two different types of solar cells. In particular, SnS/ZnO solar cells did not show any open circuit voltage and photocurrent, which is the evidence that the band alignment is not favorable between our sputtered SnS and ZnO layers that were used for this experiment. So, before making a p-n junction with other n-type semiconductor, fabrication of thin film solar cells with relatively simple structure would be beneficial to understand features of SnS thin film solar cells and to achieve more efficiency under p-n junction structure. Schottky barrier SnS thin films have a simple structure and they have an advantage in fabrication. Since it is found that indium makes ohmic contact to SnS, work function of sputtered SnS thin film is expected to be near the work function of indium metal. For other side, lower work function metal can be considered to make Schottky junction since SnS is usually reported as a p-type semiconductor material. Figure 6-2 shows the example using simulation for SnS Schottky junction solar cells done by AMPS-1D. Simulated band structure of Schottky junction solar cells with 600 nm thick SnS thin film is shown in Figure 6-2 (a). The similar work function of SnS thin films to indium (4.09 eV) is assumed for back contact. For front contact one of lower work function materials, Mg (3.66 eV) is considered to build Schottky barrier to SnS thin films. Considering transparency of front contact layer, thin metal film or unique design such as finger-shaped contact can be considered. Ignoring the effect from the trap levels which may be located within the band gap, 6.254 % of conversion efficiency can be obtained from Figure 6-2 (b). By fabricating the SnS

Schottky barrier solar cells and investigating its features, more understanding on SnS thin films solar cells is possible and this would be a basis for the realization of the SnS thin film solar cells.

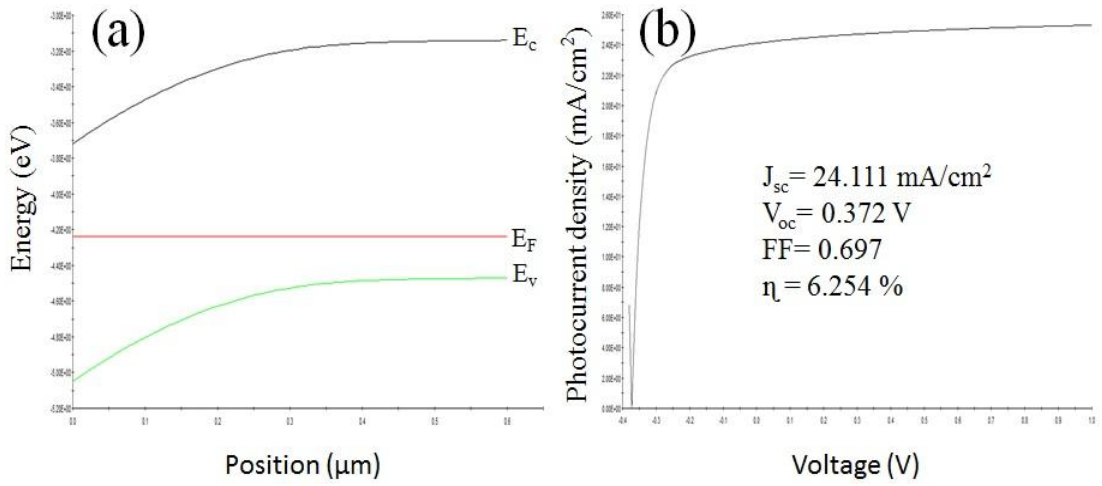

Figure 6-2. SnS Schottky junction solar cells with Mg and In metal contacts by AMPS-1D (a) simulated band diagram (b) J-V characteristics under AM 1.5 illumination. E_c, E_F and E_v denote conduction band edge, Fermi level and valence band edge, respectively.

6.3 Chapter 6 Reference

[1] T. H. Sajeesh, K. B. Jinesh, M. Rao, C S. Jartha, K. P. Vijayakumar, Defect levels in SnS thin films prepared using chemical spray pyrolysis, *Physica Status Solidi A* Vol. 209 No. 7 (**2012**) 1274-1278.

[2] J. B. Johnson, H. Jones, B. S. Latham, J. D. Parker, R. D. Engelken, C. Barber, Optimization of photoconductivity in vacuum-evaporated tin sulfide thin films, *Semiconductor Science and Technology* Vol. 14 (1**999**) 501-507.

[3] M. Devika, N. Koteeswara Reddy, K. Ramesh, K. R. Gunasekhar, E. S. R. Gopal, K. T. Ramakrishna Reddy, Influence of annealing on physical properties of evaporated SnS films, *Semiconductor Science and Technology* Vol. 21 (**2006**) 1125-1131.

[4] O. E. Ogah, K. Ramakrishna Reddy, G. Zoppi, I. Forbes, R. W. Miles, Annealing studies and electrical properties of SnS-based solar cells, *Thin Soild Films* Vol. 519 (**2011)** 7425-7428.

[5] Y. Guo, W. Shi, Y. Zhang, L. Wang, G. Wei, Influence of Substrate Temperature on Properties of Tin Sulfide Thin Films in Proceedings of *SPIE* Vol. 6984 (**2008**) 69841P-1-69841P-5.

VITA

Hyeonseok Lee

EDUCATION

- Ph. D, Department of Electrical engineering, Pennsylvania State University, University Park, USA, 2014 Spring (Advisor: *Mark W. Horn*)
- M. S. Electrical engineering Myongji University, Yongin, Republic of Korea, Feb 2008 (The title of thesis: *Effects of Chemical sintering and TiO_2 nanoparticles on Carbon electrodes for Dye-sensitized Solar cells*)
- B. S. Electrical engineering Myongji University, Yongin, Republic of Korea, Feb 2006

RESEARCH EXPERIENCE

- SnS thin film solar cell by RF sputter(*Jan 2012-2014*)
- CO_2 conversion to methane by using Cu sculptured thin film cocatalyst (*Jan 2012 ~Jan 2013*)
- VO_x thin film deposited by biased target sputter for Infrared camera (*Sep 2011~Jan 2012*)
- Sculptured Pt nanowire thin film for Dye-senstitzed solar cell (*Jan 2011~Aug 2012*):
- Nanostructured TiO_2 photoanode for dye-senstized solar cells (*May 2010~Dec 2010*):

TEACHING EXPERIENCE

- Teaching Assistant (Aug 2010~May 2014)
  Subject: EE340 & EE 397E *Introduction to nano electronics*, EE311 *Electronic circuit design* and EE 442 *Solid state devices*,

PUBLICATION

A. *PEER REVIEWED JOURNALS*

- **Hyeonseok Lee**, Mark W. Horn, *Thin Solid Films* Vol. 540 (**2013**) 208-211.
- Rona E. Banai, **Hyeonseok Lee**, Michael A. Motyka, Ramprasad Chandrasekharan, Nikolas J. Podraza, Jeffrey R. S. Brownson, Mark W. Horn, *IEEE Journal of Photovoltaics* Vol. 3 No. 3 July (**2013**) 1084-1089.
- Su-Il In, Klaus P. Almtoft, **Hyeonseok Lee**, Inge H. Andersen, Dongdong Qin, Ningzhong Bao, C. A. Grimes, *Bulletin of the Korean Chemical Society* Vol. 33 No. 6 (**2012**) 1989-1992.

B. *Proceeding*

- R.E Banai, **H. Lee**, S. Zlotnikov, J. R. S. Brownson, M. W. Horn, *39th IEEE Photovoltaic specialist conference* (**2013**).

- R.E. Banai, **H. Lee**, M. Lewinsohn, M. A. Motyka, R. Chandrasekharan, N. J. Podraza, J. R. S. Brownson, M. W. Horn, *38th IEEE Photovoltaic specialist conference* (**2012**) 000164-000169.